UNIVERSITÀ
DEGLI STUDI
FIRENZE

DOTTORATO DI RICERCA IN NEUROSCIENZE

CICLO XXXV

COORDINATORE Prof.ssa Amato Maria Pia

SIENA-SC: accurate, robust, and automated longitudinal spinal cord change analysis

Settore Scientifico Disciplinare MED/26

Dottorando
Dott. Luchetti Ludovico

Tutore
Prof. De Stefano Nicola

Coordinatore
Prof.ssa Amato Maria Pia

Anni 2019/2022

Acknowledgements

I am immensely grateful to all my supervisors. To Prof De Stefano, for giving me the opportunity to work and contribute to his lab. To Marco Battaglini, source of joy and torment throughout my PhD journey. His passion for research, unwavering commitment, and insightful guidance have been invaluable. To Ferran Prados, for demonstrating a remarkable patience in guiding me and ensuring I stayed focused on my goals. And, last but not least, to Rosa Cortese, for her unwavering support and the time she dedicated to reviewing and improving my work. Their expertise, constructive feedback, and encouragement were instrumental in shaping the direction of this research.

I would like to express my gratitude to all current and former colleagues in the Siena Imaging group. While their contributions on this specific work may have been limited, the exposure to the lab's atmosphere has significantly contributed to my personal growth.

Thanks to all my friends who were a constant source of motivation and joy, for their understanding, encouragement, and occasional distractions that provided much-needed breaks.

Finally, I cannot thank my family and especially my parents enough for too many things to mention here.

Abstract

In this thesis we present a new method to assess longitudinally spinal cord (SC) atrophy, called SIENA-SC.

The spinal cord (SC) is an important area of the central nervous system (CNS) as it plays a critical role in both motor and sensory functions. Magnetic resonance imaging (MRI) allows for *in-vivo* visualization of the SC, providing valuable insights into its structure and function and helping the diagnostic workup of several neurological conditions such as multiple sclerosis (MS), amyotrophic lateral sclerosis (ALS), and spinal cord injury. In addition, the quantification of SC atrophy can be used to monitor disease progression and as an outcome measure in clinical trials. However, these measures have not reached yet a degree of robustness and reliability comparable to those of brain atrophy, which are currently used to monitor disease progression and treatment efficacy in neurodegenerative diseases.

To date, there are two possible strategies to assess longitudinal volumetric changes of SC over time. The first is to compare the cross-sectional area (CSA) from segmentation maps obtained independently at each timepoint. This approach provides an indirect estimation of the atrophy rates and is limited by the inaccuracy of segmentation maps due to partial volume effects. The second approach relies on these SC segmented masks, but they are registered on a common reference space, providing a direct estimation of atrophy measurements. The first attempt to provide a reliable tool to measure SC atrophy longitudinally was made through the generalized boundary shift integral (GBSI)., an optimization of an algorithm that has been already validated to assess brain atrophy.

Structural Image Evaluation using Normalization of Atrophy (SIENA) is a widely recognized method that employs registration techniques to measure changes in brain volume over time. Over the past two decades, SIENA has been extensively used to evaluate brain atrophy due to its user-friendly nature and its reliability. SIENA calculates the zeros of the second derivative of the intensity profiles of the lines perpendicular to the surface in the two images to be compared. This approach helps to reduce the influence of MRI intensity inhomogeneity, as it relies on the shape of the intensity profiles rather than their specific intensity values. By using this method, the variability introduced by intensity variations is minimized, allowing for more robust and reliable measurements of atrophy.

The study presented in this thesis introduces SIENA-SC, which is an adapted version of the SIENA method, designed to calculate the percentage of spinal cord change (PCVC) over time directly on the cord edges. Our main objective was to provide a fully automated approach that reduces variability in measuring SC atrophy and offers a solution similar to longitudinal brain atrophy measurements.

In the first experiment, using a multicenter dataset including 13 scan-rescan and 190 Healthy Control (HC) subjects, SIENA-SC showed to have a lower measurement error than GBSI and CSA, reflected by lower standard deviation, coefficient of variation and median absolute variation.

In the second experiment, the lower measurement variability of SIENA-SC than GBSI and CSA, was confirmed in a dataset of 65 MS subjects and the same 190 HC of the previous experiment, thus resulting into a better differentiation between patients with MS and HC, an improvement of statistical power, and reduction of sample size estimates.

In conclusion, SIENA-SC showed to be robust and feasible when assessing SC atrophy using brain MRI scans routinely acquired in clinical practice. Longitudinal spinal cord atrophy measured through SIENA-SC has the potential to become a recognized outcome measure for clinical trials. However, it should currently be considered as a secondary outcome measure until additional advancements enhance the ease of acquisition and processing. Further developments of the methods are needed to make the process more streamlined and user-friendly.

Impact Statement

In this thesis, I have developed and validated the Structural Image Evaluation using Normalization of Atrophy in Spinal Cord (SIENA-SC), one of the first registration-based method for quantification of spinal cord atrophy. The SIENA-SC pipeline is a modified version of the original SIENA method that has been designed to address the limitations of commonly used segmentation-based methods, such as measuring the spinal CSA. Furthermore, SIENA-SC has been designed for using routinely acquired MRI of brain.

The improvements in spinal cord atrophy measurements presented in this thesis can expand research possibilities for future neurodegenerative diseases projects, such as Multiple Sclerosis, Amyotrophic Lateral Sclerosis and SC injury, where SC volume changes are representative of the most aggressive aspects of the diseases.

The high robustness and reliability reached by SIENA-SC suggests that this tool has the potential to become a gold standard for clinical trials including spinal cord atrophy as an outcome measure. Moreover, obtaining spinal cord atrophy measurements from brain scans could represent a viable and clinically meaningful alternative to more technically challenging spinal cord images, in particular in multi-centre settings where homogenous spinal cord acquisitions are not feasible.

Finally, results of this thesis are also important for the patients. Deriving spinal cord atrophy measurements from brain scans would significantly reduce the scan time for MRI and, thus, participants' burden. In the future, it is important to identify changes in spinal cord volume

which may improve the monitoring of the clinical course of neurological disease and its treatment response.

Table of contents

List of abbreviations

ALS: Amyotrophic lateral sclerosis

AS: Active Surface

BET: Brain Extraction Tool

BSI: Boundary Shift Integral

CNS: Central Nervous System

CSA: Cross-sectional area

CSF: Cerebrospinal fluid

DIS: Dissemination in space

DIT: Dissemination in time

ET: Echo Time

FOV: Field of View

GBSI: Generalized Boundary Shift Integral

GM: Grey Matter

MOG: Myelin oligodendrocyte glycoprotein

MS: Multiple Sclerosis

MRI: Magnetic Resonance Imaging

NBV: Normalized Brain Volume

NMO: Neuromyelitis optica

NMOSD: Neuromyelitis optica spectrum disorder

PBVC: percentage brain volume change

PCVC: Percentage Cord Volume Change

RRMS: Relapsing Remitting Multiple Sclerosis

RT: Repetition Time

SC: Spinal Cord

SCT: Spinal Cord Toolbox

SD: Standard Deviation

SE: Standard Error

SIENA: Structural Image Evaluation using Normalization of Atrophy

SIENA-SC: Structural Imaging Evaluation, Using Normalization, of Atrophy for Spinal Cord

SPMS: Secondary Progressive Multiple Sclerosis

PPMS: Primary Progressive Multiple Sclerosis

WM: White Matter

List of Tables

List of Figures

1 Introduction

In this thesis, we present a new method for longitudinally assessing spinal cord (SC) atrophy, called SIENA-SC (Structural Imaging Evaluation, Using Normalization, of Atrophy for Spinal Cord), on routinely acquired MRI.

To make the thesis self-consistent, the necessary concepts will be provided in the introduction so that the objectives can then be correctly described. The notions necessary to understand the new solutions implemented in the software will also be provided.

Therefore, the introduction will be organized as follows:

1. An overview of the anatomy of the spine;

2. a review of the current state of the art methods for the analysis of the brain and the spinal cord, with a particular regard to the SIENA methodology. This section will explore also the challenges of spinal cord imaging and the attempts to overcome them to develop reliable SC analysis tools;

3. a description of the role of the spinal cord in neurodegenerative disease, with a particular focus on MS, a disease where SC atrophy has been already characterized.

1.1 The Spinal Cord

The SC constitutes, along with the brain, the central nervous system (CNS). The SC is a long tubular-shaped structure located in the vertebral column, surrounded by Cerebrospinal fluid (CSF) and extending from the medulla oblongata in the brainstem to the first or second lumbar

vertebrae depending on individuals (Figure 1). As an extension of the brain, its role is to relay nervous signals between the brain and the peripheral nervous system, ensuring the transfer of efferent and afferent messages between the cerebral cortex and the motor and sensory system. It is also the center for reflexes coordination and control. In particular, SC hosts central pattern generators which control rhythmic movements such as breathing or walking.

1.1.1 Structure

The SC consists of 31 segments through which spinal nerves symmetrically enter and exit by right and left sides : C1 to C8 for cervical levels, T1 to T12 for thoracic levels, L1 to L5 for lumbar levels and S1 to S6 for sacral levels. During embryonic development, vertebrae match spinal levels but as vertebral column grows faster than SC, it is not the case anymore at adulthood. In general, the spinal levels are found at the same height as their respective rostral vertebral levels (e.g., spinal level C4 is at the same height as vertebral level C3) [1]. However inter-individual variations are observed [2].

The SC is made up of grey (GM) and white matter (WM) (Figure 1). GM is found in the center with a butterfly or H shape, while white matter surrounds it. SC cross-section changes in shape and area along inferior-superior axis (Figure 2), as GM and WM do. The GM/WM CSA ratio is also reduced with aging [3,4]. The SC cross-section shape is round at thoracic and lower lumbar levels and elliptical at cervical levels.

SC surface is cover by a thin membrane, the *pia mater*, which is the innermost layer of the meninges, with the arachnoid mater and the dura mater as the outermost layer, at the surface of the spinal canal. The spinal canal or the *subarachnoid* cavity is filled with CSF. The CSF is a colorless fluid derived from blood plasma with equivalent sodium content but almost no

proteins. It is composed at 99% of water. The remaining is glucose, potassium, calcium, magnesium and chloride. The CSF plays a protective role for the brain and SC, acting as a cushion or buffer. It also plays a role of autoregulation of the cerebral blood flow and prevention of brain ischemia. Finally, it is an important component of the lymphatic system as it enables metabolic waste products from brain and SC to be cleared.

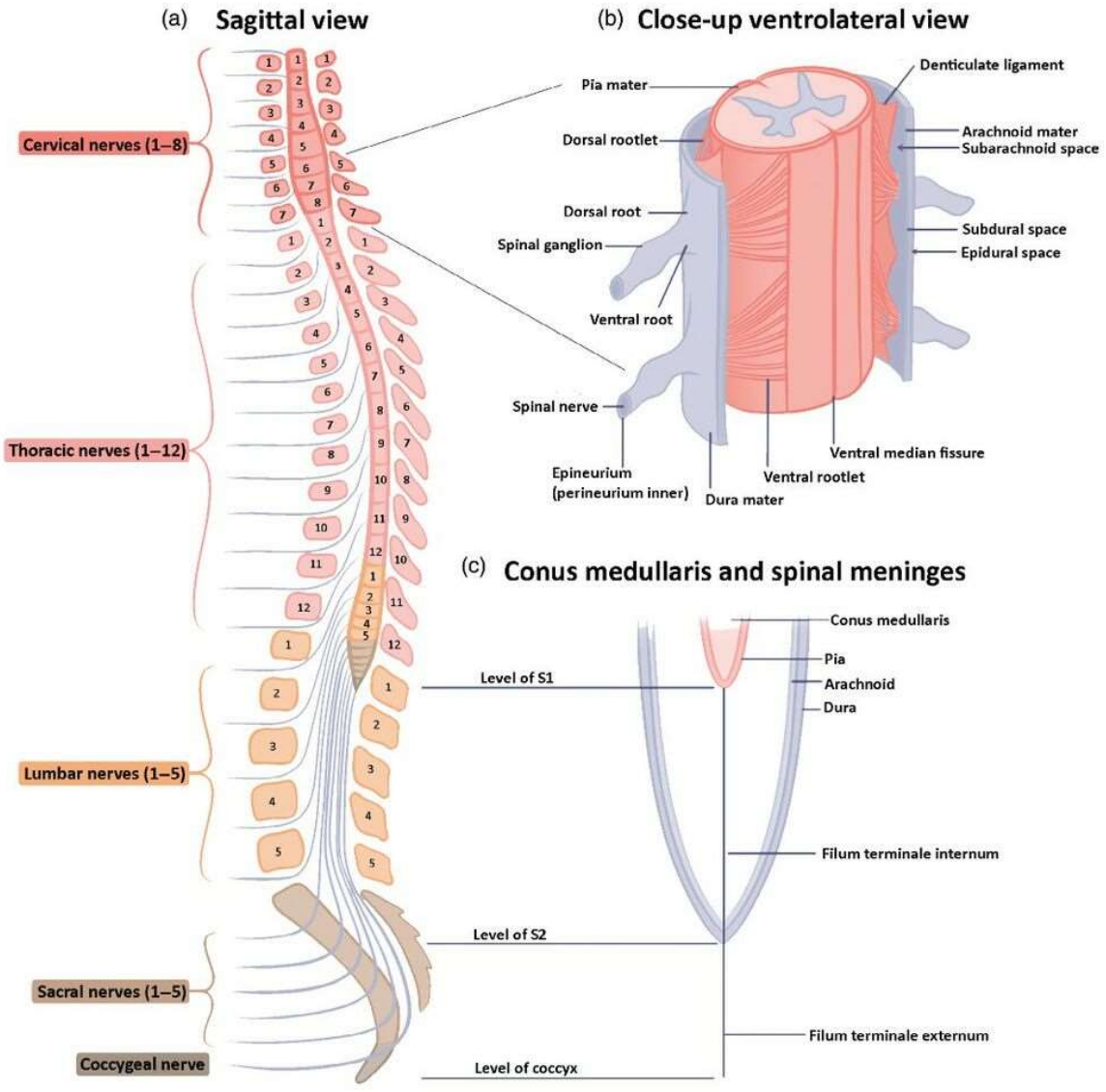

Figure 1: a) Sagittal view of Cord Segments, b) close up of ligaments, c) conus medullaris. Source: https://wikimsk.org/wiki/Spinal_Cord_Anatomy.

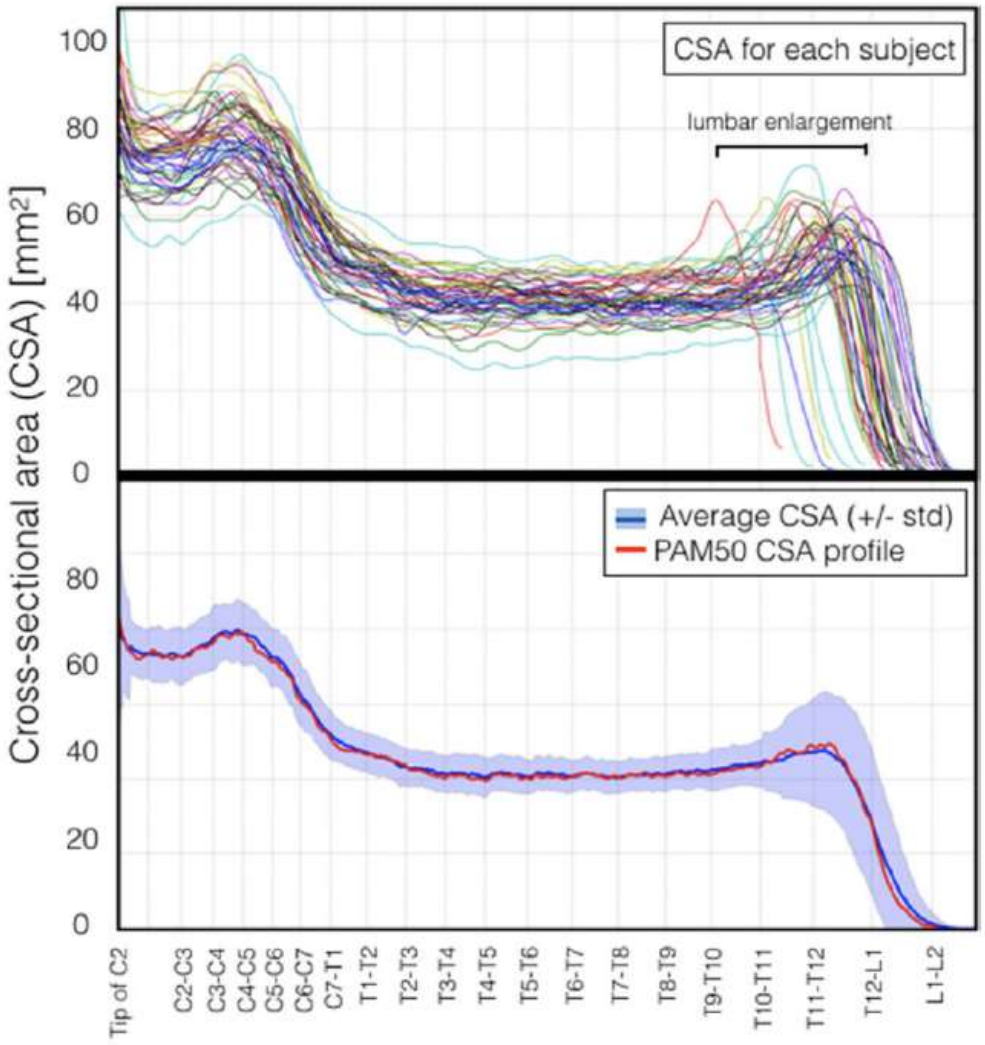

Figure 2: Spinal cord cross-section area evolution along inferior-superior axis within 50 healthy subjects (mean age: 27 ± 6.5 y.o., 29 men, 21 women, source: De Leener et al., 2018).

1.1.2 Grey matter

The GM of the SC has the shape of a butterfly or the letter H (Figure 3) and it is mainly made up of a mixed of neurons, interneuronal connection fibers, glial cells (cells supporting neurons environment) and blood vessels. GM is generally divided into three main columns on each side which host specific cellular groups receiving the nerve endings (Figure 3): the dorsal or posterior horn, the ventral or anterior horn and the intermediate or lateral GM. In the center is the central canal filled of CSF. The dorsal horns host the free nerve ending of afferent nerve fibers entering SC by dorsal roots and transmitting signal to sensory neurons. The ventral horns host the free nerve ending of efferent nerve fibers exiting SC through ventral roots and transmitting signal from motor neurons (**Errore. L'origine riferimento non è stata trovata.**). Afferent neurons and efferent neurons are connected through interneurons in the central grey commissure around the central canal. These connections are responsible for *spinal reflexes* (e.g., limb withdrawal reflex after a painful stimuli).

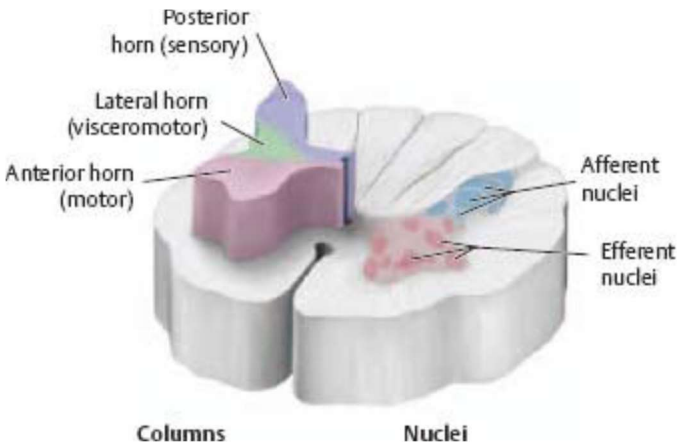

Figure 3: Spinal grey matter organization. Diagram at thoracic level (Source: https://doctorlib.info/medical/anatomy/43.html on June 18, 2020).

1.1.3 White Matter

The white matter is made of long fibers called *axons*, running along the inferior-superior axis and relaying nervous signal from neurons or receptors to other neurons or effectors. Those fibers are wrapped in a myelin sheath providing a pale color to tissue (hence the name *white matter*), which is produced by glial cell named *oligodendrocytes*. Axons diameters ranges from 1 to 10 µm in humans [5]. White matter also includes some blood vessels and CSF in extracellular space. Axons with globally same origin and destination are grouped by region and function in symmetric right-left *pathways* or *tracts* (Figure 4). Two main categories can be identified: the sensory ascending pathways and the motor descending pathways. Ascending pathways consists of afferent fibers entering SC through dorsal roots or coming from SC GM and conducting information to higher levels. Descending pathways are mainly composed of fibers coming from motor cortex or brainstem and conducting information to lower levels and to the peripheral nervous system. Finally, the propriospinal (or intersegmental) tracts are a third category of pathways which are made of both ascending and descending, crossed and uncrossed short fibers, and which interconnect adjacent or distal spinal levels. Main tracts of this category (not represented in Figure 4) are the ventral propriospinal tract, the lateral propriospinal tract and the dorsal propriospinal tract.

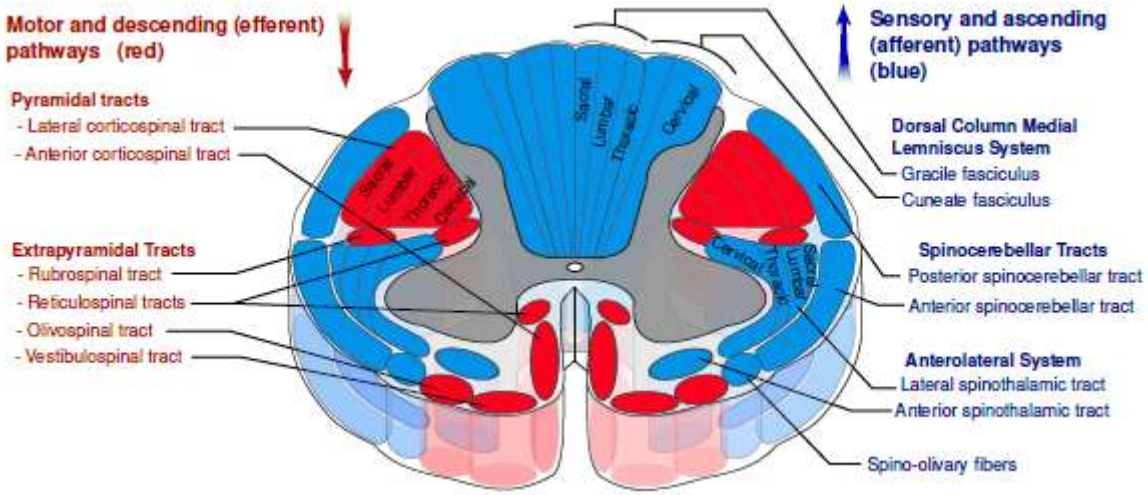

Figure 4: Atlas of major white matter spinal tracts. In red are the motor descending pathways, in blue are the sensory ascending pathways. Source: https://upload.wikimedia.org/wikipedia/commons/thumb/b/b2/Spinal_cord_tracts_-_English.svg/1920px-Spinal_cord_tracts_-_English.svg.png

1.2 Towards brain segmentation to spinal cord segmentation

In order to be able to explain in detail SIENA-SC, the solution proposed in the following chapters of this thesis for the evaluation of longitudinal atrophy of the SC, it is appropriate to preliminarily introduce some general concepts related to the characteristics of MRI images, list the possible causes of variability in the images themselves and some of the solutions proposed in the field of volumetric analysis of the brain. Afterwards, we will describe the different approaches used in the evaluation of SC atrophy.

MRI is a medical application of nuclear magnetic resonance. MRI is a medical imaging technique used in radiology to obtain images of the anatomy and physiological processes of the body. MRI scanners use strong magnetic fields, magnetic field gradients, and radio waves to generate images of the body's organs. MRI is not invasive, because it does not involve the use of X-rays or ionizing radiation, which distinguishes it from CT and PET scans. The result of an MRI sequence is the creation of a high-definition 3D image of the organ being studied. An MRI image thus consists of an ordered, three-dimensional grid of voxels, the minimal elements of a 3D image equivalent to the pixels of two-dimensional images. The intensity encoded in each voxel does not directly reflect any physical content but is indirectly related to the times with which the spins of hydrogen atoms, previously aligned along a direction through the use of a constant magnetic field B0, return to the same once excited through a pulse of known radio frequency, called B1. These time intervals are called relaxation times, vary from tissue to tissue, and depend on parameters, such as repetition time (RT: the time between excitation pulses) and echo time (ET: the time in which radiofrequency data returning from the tissue after the initial radiofrequency pulses are collected) whose different combination allows

different sequences to be constructed, which create images with varying intensity contrast between tissues.

Given the complexity of the physical processes and digital signal processing involved in creating an MRI image, the artifacts that can be generated are numerous. These can depend on either hardware-related problems, such as B0 inhomogeneity in the region encompassing the analyzed organ or intensity distortions due to B1 field inhomogeneity, or problems related to patient cooperation, such as motion artifacts. Another, ineradicable source of variability in MRI images is called the partial-volume effect and is generated when the voxel size is larger than the intrinsic size of the structures to be studied. The artifact occurs as a blurring of intensities in voxels that contain multiple tissues, such as the irregular interfaces between white and GM in the brain.

This brief and far from exhaustive review of the principles that preside over the creation of MRI images and the possible sources of error allows us to focus on the various analysis pipelines that have been developed to analyze atrophy variations computed on MRI images.

Generally speaking, image segmentation is the process of dividing an image into different parts, aiming to define specific regions, whose boundaries separate image parts that display distinct features. Quantitative MRI measures are strongly dependent not only on acquisition parameters, but also on processing methods, presenting with different sensitivity to change, repeatability and measurement error.

Several libraries of free online software for neuroimaging analysis have implemented pipelines for fully automated quantification of brain atrophy and SC. Referring to the existing literature,

we can provide a schematic classification of software. We speak of a "segmentation method" when the software does not directly compare brain MRI images of the same subject acquired over time. This type of software is mostly used in cross-sectional analysis. Conversely, it is called "registration method" when the software directly compares brain MRI images of the same subject acquired over time and is based on an initial registration. This type of software is often used in longitudinal analysis [6].

Most 'segmentation-based' software packages divide the analysis into separate sub-phases. The first one reduces the amount of voxels to be analysed. Thus, for the analysis of brain images, this phase automatically separates the parenchyma (GM+WM+CSF) from the non-parenchyma, while for the analysis of SC images, this phase automatically segments the SC cord. The second one consists of automatically correcting the MR images of the previously identified organ for B0 inhomogeneity (e.g. brain or SC). Finally, these approaches provide the total volume and GM and WM volumes by summing the partial volumes (PVE) of each tissue estimated in each voxel, i.e. the proportions of WM, GM and CSF present in each voxel of an MRI image. The quantification of the PVE in each voxel starts by assigning the PVE to a given voxel, using its intensity and that of the surrounding voxels, thus reducing classification errors due to the presence of random noise. To improve segmentation, a-priori spatial information concerning the position of voxels can be added to the MRI intensities, thus reducing the estimated proportion of a certain tissue in voxels that most likely belong to a different tissue, based on their position.

"Registration-based" software packages provide the total/GM/WM volume changes by comparing co-localized volumes of serially acquired MRI images from the same subject. A

preliminary step common to most of these procedures is the registration of all MRI images of the same subject on the same virtual space. Early software packages used in longitudinal analysis introduced the concept of halfway-space in which to align two MRI examinations of the same subject and on which to measure the percentage of change in overall volume by calculating the shift in the parenchyma/CSF boundary over time.

Before describing the solutions developed for SC, it is instructive to look in detail at the pipelines implemented in some of the software used for the analysis of brain atrophy, as many of the solutions implemented in the analysis of SC atrophy exploit software (or concepts) previously developed for the analysis of brain images.

1.2.1 Brain Segmentation method

1.2.1.1 Sienax

SIENAX works for cross-sectional (single time point) analysis, and it is useful for differentiating two groups of subjects on the basis of single time point brain size measurement [7].

SIENAX attempts to estimate normalized brain volume (NBV) from a single image, using the skull to normalise spatially, with respect to a standard image. It starts by performing segmentation of brain from non-brain tissue in the head and estimates the outer skull surface. The brain and skull images are then registered to a standard space brain and skull image pair derived from the MNI152 standard image [8]. Next a standard space mask is used to make sure that no parts of the eyes are left from the brain extraction (because of the connection of the optic nerve, this can occasionally happen) and also to provide a consistent (i.e., non-arbitrary)

cutoff point for the brain stem. Finally tissue-type segmentation is carried out (including partial volume estimation) and a (normalised) brain volume estimate is produced.

The normalization for head/skull size is very important because it reduces within-group variations, making cross-group comparisons more sensitive.

The complete SIENAX method is summarized in the Figure 5.

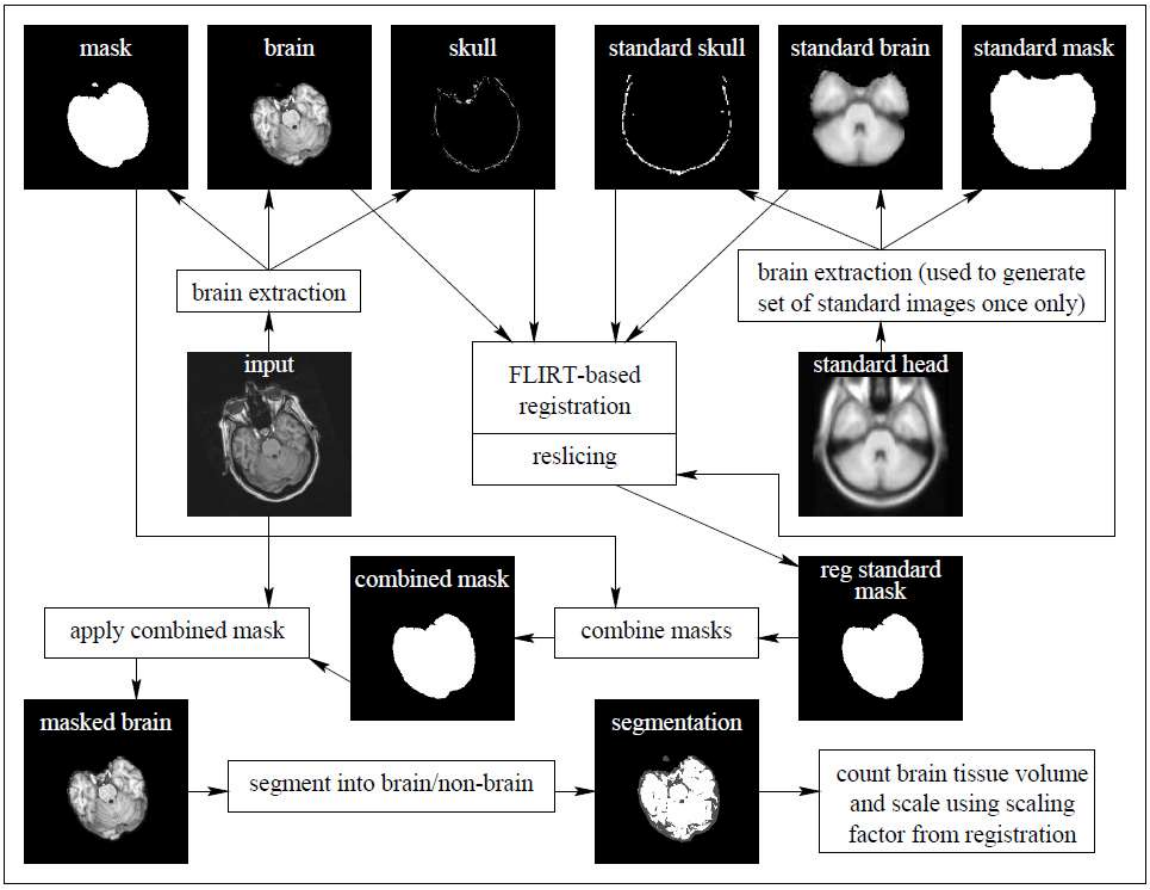

Figure 5: Example of SIENAX workflow.

1.2.2 Brain Registration methods

Brain atrophy measures have been a cornerstone in the study of interventions with putative neuroprotective effects [9–11], because of the application of registration-based methods that provide direct estimates of brain atrophy, such as the SIENA [7], and the BSI method [12–14]. Both SIENA and BSI demonstrated a reduced sample size requirements to detect significant differences between groups or over time and are nowadays well-established methods to measure longitudinal brain atrophy in clinical trials and in observational studies for neurodegenerative diseases [15].

The two methods mentioned above will be described in detail, as they form the conceptual basis on which SIENA-SC is based and describe some of the functionalities that have been employed, with the necessary adaptations, in the implementation of SIENA-SC.

1.2.2.1 Siena

SIENA performs segmentation of brain from non-brain tissue in the head and estimates the outer skull surface (for both time-points), and uses the resulting masks to register the two images on a halfway space, while correcting and normalising for imaging geometry changes. Then the registered segmented brain images are used to find local atrophy, measured on the basis of the movement of image edges [7,16].

Brain extraction

The first processing stage is the separation of parenchyma from non-parenchyma tissue. The method used is known as BET - Brain Extraction Tool [17]. BET provides a binary brain mask, the segmented brain image, and an external skull surface image as output.

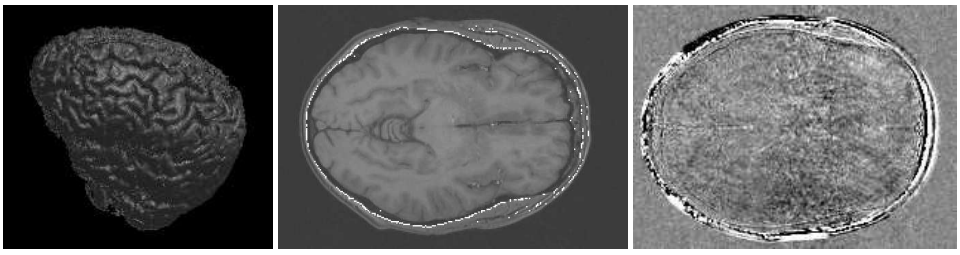

Figure 6: Left: Example brain surface found by BET. Middle: Example skull surface found by BET. Right: example subtraction image after registration of two images from a subject without atrophy.

Skull extraction

Measurement of changes in brain size benefits from the estimation of the skull (which is of fairly unvarying size over time in an adult) as a normalising factor in both cross-sectional and longitudinal measurements.

Before brain change can be measured, the two images of the brain have to be registered (aligned). Clearly this registration cannot allow rescaling, otherwise the overall atrophy will be underestimated. However, because of possible changes in imaging geometry over time (due to gradient calibration drift or variable local field distortions), it is necessary to hold the scale constant (see also [18] for previous work on this problem; note that some longitudinal methods have failed to take account of this problem, although methods based primarily on cross-sectional measurements tend to normalise against it). With the method described here, this can be achieved by using the exterior skull surface (assumed to be constant in size and shape for an individual) as a scaling constraint in the registration.

In most MR images, the skull appears very dark. In T1-weighted images, the internal surface of the skull is largely indistinguishable from the CSF, which is also dark. Thus, the exterior

surface is searched for. This also can be difficult to identify, even for human experts, but is the most realistic surface to aim to find. The exterior skull surface is found automatically as the final stage of brain extraction, using BET. Starting with the estimated brain surface, each surface point is taken as the start of a search outwards for the optimal skull position. The most distant (from the brain) point of low intensity (before the bright scalp) is found, and the first peak in gradient outside of this is then defined as the exact position of the exterior of the skull surface. This method is quite successful, even in regions of overlying (dark) muscle or where there is significant (bright) marrow within the bone. Thus, a skull image is generated for each input image, to be used in registration.

Registration

As already stated, before the differences between two images can be found, the brains in the two images must be aligned, using a registration procedure. The registration carried out uses a robust and accurate automated linear registration tool, FLIRT (FMRIB's Linear Image Registration Tool) [19]. A three-step procedure is used, where the brain images are used to optimise the initial registration and the final translation and rotation, whilst the skull images are used to optimise the scaling and skew.

One could stop here and apply change analysis to the registered second brain and the original first brain. However, this is not optimal, as the second brain image has been through a processing step that the first brain image has not, namely a spatial transformation (involving interpolation of its values). The images will therefore look slightly different; the transformed second brain image will be slightly more blurred than the first brain image. To ensure that the images being compared undergo equivalent processing steps, both input images are

transformed to a position which is halfway between the two. In this way both images are subjected to a similar degree of interpolation-related blurring.

The typical quality of this brain registration is illustrated in Figure 6 (right), an example subtraction of a registered pair of head images, which shows only appreciable motion outside of the skull.

All of the brain and skull images are now discarded; only the original unsegmented images and the brain mask images are kept. The transformations are applied to these images so that two registered ("common-space") head images and two registered brain mask images result. These four images are passed on to the next stage.

Masking

The registered binary brain masks are now combined into a single mask which will be applied to the registered head images to produce two new registered brain images. The reason for this (rather than keeping the original registered brain images) is that even slight differences in the original brain segmentations (i.e., the production of the brain masks) would cause the artefactual appearance of brain change. Thus, the two masks are "binary ORed" - i.e., if either is 1 at a particular voxel, the output is 1. (They cannot be "ANDed" as the brain from the second time point would cause incorrectly reduced masking of the first time point image in the case of atrophy.)

The resulting combined mask is then applied to the registered head images to produce two registered brain images. These two images are passed to the final stage for the analysis of change.

Change analysis

The next stage in the analysis is the change estimation itself. There is great variety in how this is achieved amongst published longitudinal atrophy methods. Some researchers (e.g., [20–22]) use normalized subtraction of the images, assuming that resulting areas of significant deviation from zero correspond to areas of interesting brain change. This relies on the assumption that the images will appear exactly the same (apart from the change of interest); various procedures such as histogram matching and relative bias field correction have been suggested [22], in order to attempt to make the images look as similar as possible. Others look more directly for changes around tissue boundaries. For example, [12,18] use the "boundary shift integral" (the area under the intensity profile across a boundary in image 1 is subtracted from that for image 2, and normalised by the boundary height, resulting in an accurate measure of lateral motion), which gives the motion of each edge, even if blurred, but only if image contrasts in general are well matched between scans (See chapter 1.2.2.2 for further details). Methods that are principally cross-sectional in nature avoid the need to address the issue of change analysis.

The system presented here first attempts to find all brain surface edge points and then estimates the motion of these edge points from one time point to the next. This edge motion is found for the whole brain surface, enabling the total volume change to be estimated. The previously published version of SIENA found edges on the basis of edge strength, and then found edge motion by searching for matching edge points from one image to the next. This suffered slightly from relatively imprecise definition of edge points, i.e., discrimination was imperfect. The current version uses full tissue-type segmentation to find edge points, and thus

is more correctly selective, and also enforces continuity of the estimated brain surface. Thus the system presented here finds all brain surface edge points (including internal brain- CSF edge points, such as those around the ventricles) and then finds the motion of these points, in a Bayesian framework, perpendicular to the local edge, to sub-voxel accuracy.

In order to find all brain surface edge points, tissue segmentation is performed on the image from time point 1 after application of the joint brain mask (see previous section). The tool used [23] carries out tissue (GM, WM and CSF) segmentation and bias field correction. The method is based on a hidden Markov random field (segmentation labelling) model and an associated Expectation-Maximization algorithm for estimating tissue intensity parameters and bias field (spatial intensity inhomogeneity). The whole process is fully automatic (after being instructed as to whether the image is T1 or T2, and whether to attempt to segment GM and WM as a single class or as separate classes), producing a tissue-labelled segmentation. It is robust and reliable, compared to the more common finite-mixture-model-based methods, which are sensitive to noise, particularly as they use no spatial neighbourhood information.

The tissue segmentation labels are used to find all brain edge points. First, grey and white voxels are combined into a single class, as are also CSF and background voxels. All boundary voxels between these two resulting classes are used for the next processing stage. Note that this method of finding brain edge voxels enforces a continuous surface (without breaks), although not necessarily a topologically simple one. Figure 7 shows example slices through an image after edge point detection (and also example perpendicular image profiles as described below).

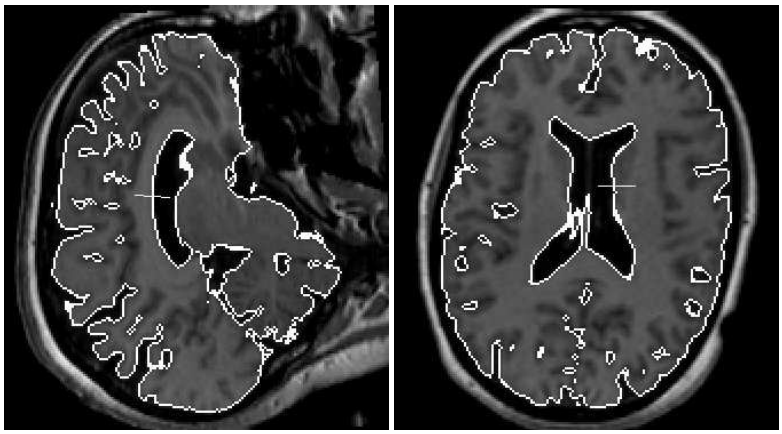

Figure 7: Example slices through an image after edge point detection, and also example perpendicular image profiles.

Next, the common-space registered image from time point one is processed at each brain edge point. First the image gradient direction (in 3D) is found, using a simple 3x3x3 Gaussian-weighted derivative operator. This is used to find the surface normal unit vector (and will always point from the darker side of the boundary to the lighter side - this information will later be used to tell the difference between atrophy and "growth").

Next, a 1D array (an intensity profile perpendicular to the edge) is filled with values from the image. These values are sampled at sub-voxel positions (using tri-linear interpolation) as the array's elements will not in general fall exactly at voxel grid positions. The length of the array is preset to a fixed number of millimeters (typically ± 3); the extent will also be limited by the presence of a second edge, for example, the far side of a sulcus, in order to prevent other nearby edges from confusing the motion estimation. A second 1D array is filled with values from exactly the same image positions from the (common-space registered) image from time point two.

Edge motion is now estimated by finding the relative shift, between the arrays, which produces the maximum correlation (to sub-voxel accuracy using interpolation of the correlation scores). However, before the correlation, each array is pre-processed in two ways.

First each profile is convolved with a differentiating kernel, as it makes sense to correlate the derivatives (edge-enhancements) of the two 1D image profiles rather than the raw image values; if there are intensity or contrast differences between the two images, the position of maximum correlation could be skewed, but this effect is much reduced if correlating edge-enhanced versions of the profiles. Thus this method requires no (intensity) normalisation of the images, and is not sensitive to problems arising from intensity inhomogeneities across the images. The second process is the multiplication of each profile by a high-power exponential profile (smoothed sharp cutoff); this acts as a prior on the expected motion by weighting the correlation score, so that higher motions are less likely than small ones - this helps reduce the effect of large motion mismatches (which otherwise make a large contribution to error in the overall method). This can be viewed as a Bayesian prior:

$$P(displacement|data) \infty P(data|displacement)P(displament)$$

(1-1)

where the first term on the right can be thought of as the raw correlation score, and second term is the prior on the displacement between the profiles

$$P(displacement) \propto e^{\frac{-displacement^4}{2\sigma^4}}$$

(1-2)

which has σ set to a suitable length such as 7mm. Because the posterior on the displacement is simply used to find the maximum probability the constants of proportionality are unimportant.

Thus, the optimal displacement is found for each edge point, and, as stated earlier, the direction of the edge normal determines whether atrophy or “growth”1 is taking place at this point. The position of optimal displacement is estimated to sub-voxel accuracy by fitting a quadratic through the correlation values at the peak and its two neighbours. Figure 8 shows example profiles from one edge point with a slight shift between time points, and the derivatives of these profiles.

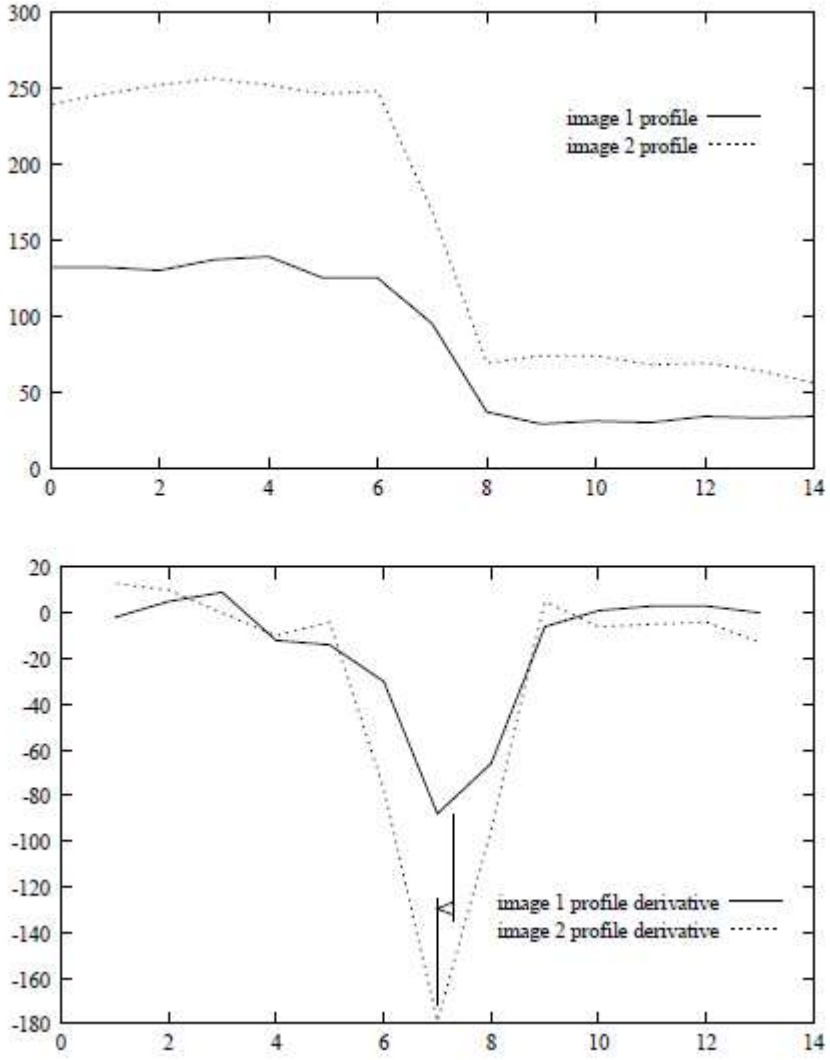

Figure 8: Example profiles from one edge point with a slight shift between timepoints, and the derivatives of these profiles.

For example, slices showing atrophy as blue edge points and “growth” as red, see Figure 9.

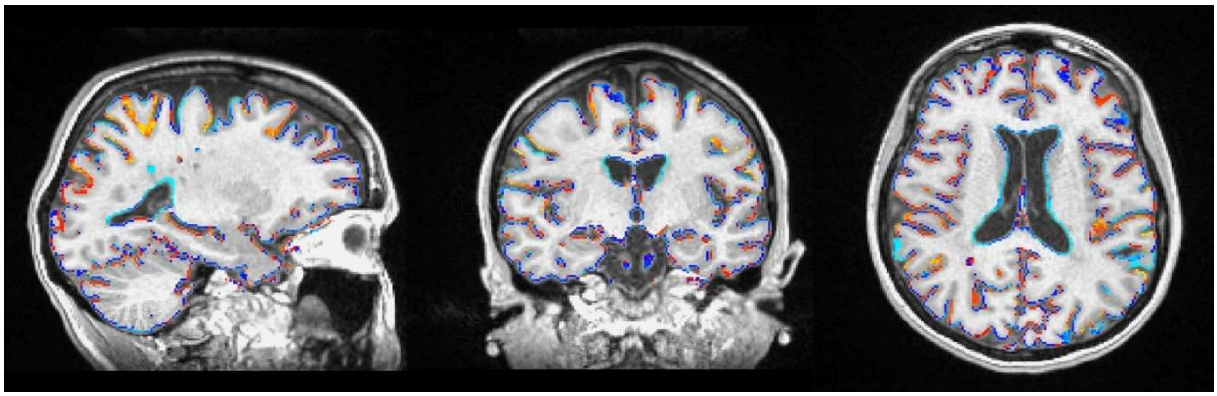

Figure 9:Example slices showing atrophy as blue edge points and "growth" as red.

Percentage Brain Volume Change Quantification

Brain atrophy is conveniently quantified by a single number such as the percentage brain volume change (PBVC). The initial value obtained from the change image is the sum of all edge point motions (linear voxel units), which, when multiplied by voxel volume, gives the total BVC. This is one possible measure, as would be a PBVC derived directly from this. However, a more invariant measure is obtained by dividing this volume by the number of edge points found times the voxel "area". (Note, the final stages of SIENA are always carried out with cubic voxels, so there is no confusion about the definition of area here.) This measure is then the mean perpendicular brain surface motion. The reason why this is preferable to the total volume change is that it is not (to first order) dependent on the number of edge points found. As the number of edge points depends on slice thickness (see below - typically by a factor of two between 1mm slices and 6mm) and (to a lesser extent) other scanning details, it is a good idea

to normalize for the number of points found. Finally, if it is required to convert the mean surface motion to a PBVC, the ratio of the brain volume to the brain surface area needs to be estimated.

In this formulation:

$$l = \frac{v\sum m}{aN}$$

(1-3)

where l is the mean surface motion, $\sum m$ is the edge motion (voxels) summed over all edge points, *v* is voxel volume, *N* is the number of detected edge points and *a* is voxel CSA. Thus,

$$\%\ brain\ volume\ change = \frac{100lA}{V} = \frac{100lfV}{V} = 100lf$$

(1-4)

where *A* is the brain surface area (actual, i.e., not *aN*), *V* is the actual brain volume, *f* is the ratio of actual area to volume.

It is possible to find *f* directly for any given image without knowing *A* or *V*; if a single image is scaled by a known amount and then compared with the unscaled version using the above change analysis, the correct PBVC is known from the scaling that was applied, and the measurement of l then allows *f* to be found. It varies across scanners, slice thicknesses and pulse sequence, but normally lies between 0.1 and 0.2mm^{-1}. Applying this method (referred to as self-calibration) helps reduce bias (systematic error) in the reported estimates of PBVC.

The complete SIENA method is summarized in Figure 10.

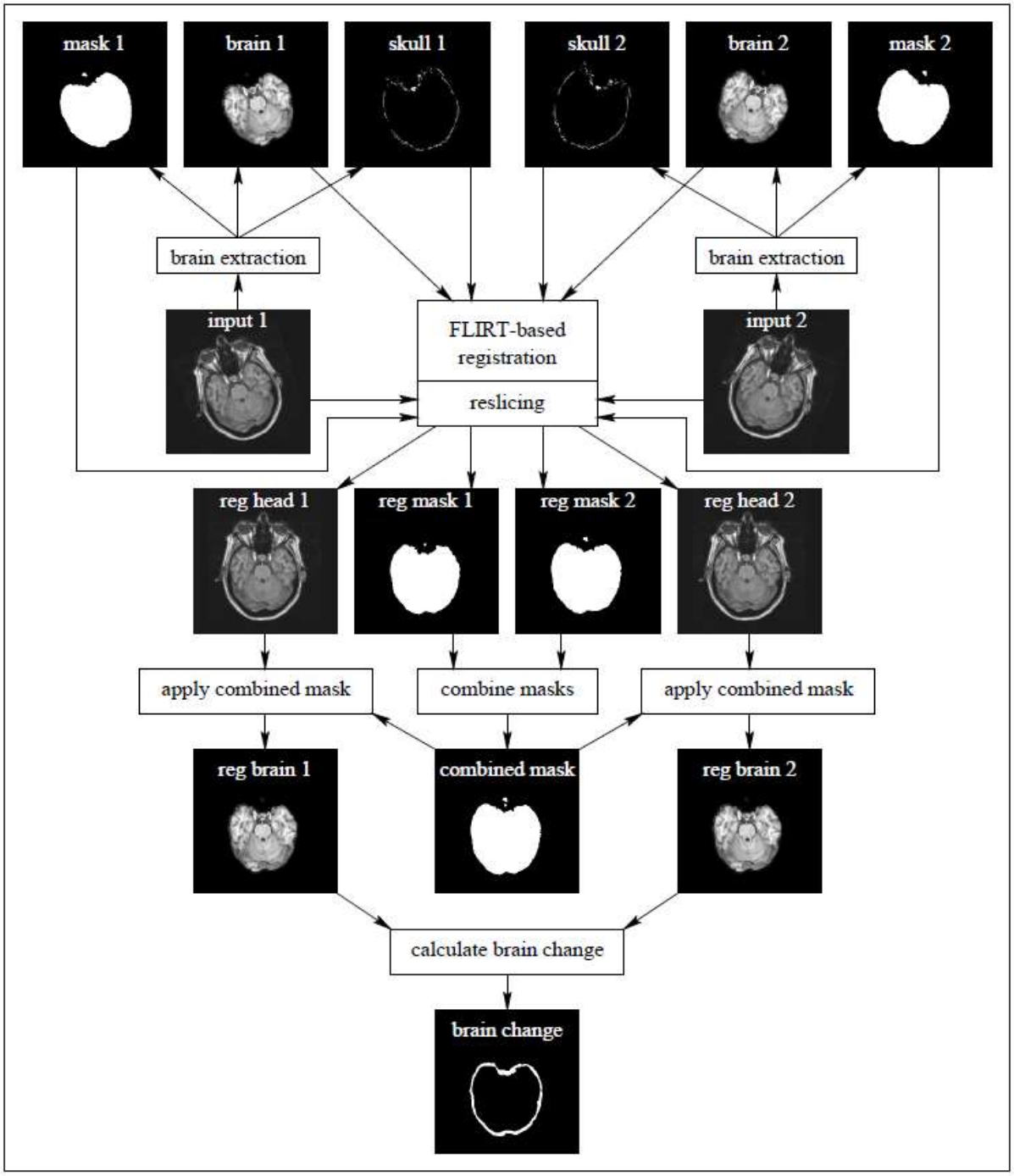

Figure 10: Overview of SIENA method

1.2.2.2 BSI

"BSI" refers to Boundary Shift Integral, is a widely recognized technique [12] to measure atrophy directly from the difference image of the registered serial MR images [12,13].

The BSI algorithm assumes that a change in volume of a soft tissue object must be associated with an exact shift in the boundary of that object. The shift of the tissue boundary results in an exactly equivalent shift of the signal which is constructed from the MR samples [12].

Hence, if the baseline scan and follow-up scan are registered, in the area around the boundary of the registered scans I_{base} and I_{reg}, the intensities of $I_{base}(x; y; z)$ and $I_{reg}(x; y; z)$ should shift by an amount corresponding to the position shift; this permits the precise measurements of boundary shifts by determining intensity shifts in the boundary region. The change in volume can thus be estimated by computing the integral of all of the boundary shifts.

If $i_{base}(x)$ is the MR signal along the cord boundary at the location x of the baseline scan and $i_{reg}(x)$ is the MR signal at location x of a registered follow-up scan on which there has been a boundary shift of $\Delta\omega$ from the baseline, then these two MR signals can be related by $i_{reg}(x) = i_{base}(x+\Delta\omega)$ in the region of the cord boundary [12]. Moreover, if the intensity changes monotonically across the cord boundary, then $i_{base}(x)$ and $i_{reg}(x)$ will take the form shown in Figure 11. We can therefore define inverse functions $x_{base}(i)$ and $x_{reg}(i)$, related by $x_{reg}(i) = x_{base}(i) - \Delta\omega$.

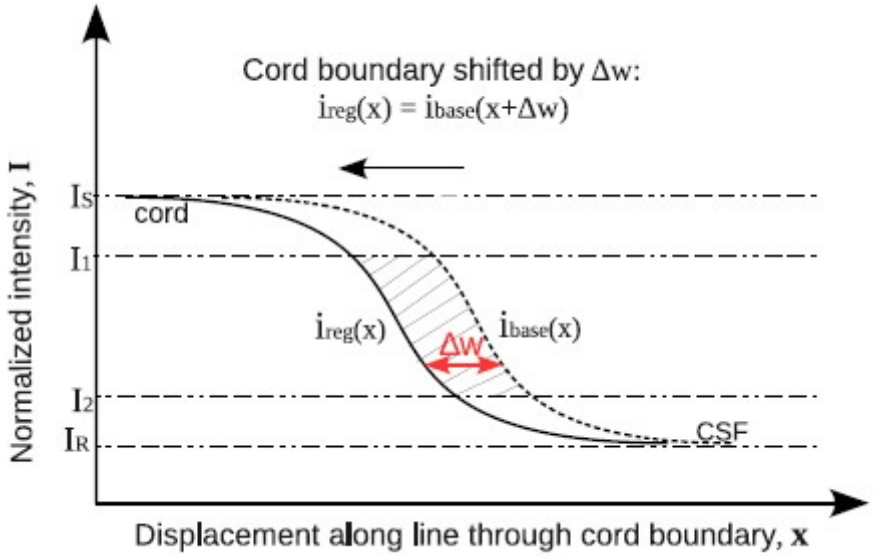

Figure 11: Example of an idealized one dimensional cord boundary shift between the intensity $i_{base}(x)$ along x axis on baseline scan, and the intensity $i_{reg}(x)$ along x axis on registered follow-up scan. An estimate of the shift along x axis, Δω, may be obtained as the shaded area divided by the intensity range (I_1 - I_2). This strategy can be extended to three dimensions to estimate the cord volume loss Δv.

A simple estimate of $\Delta\omega$ can be obtained using $\Delta\omega = x_{base}(i) - x_{reg}(i)$, where i may be any value within the intensity range of the cord boundary region $[I_R, I_S]$. In 3D T1 weighted spine MR images, the cord is brighter while the CSF is darker, thus I_R is the intensity on the CSF side of the boundary and I_S is the intensity on the cord side of the boundary. A more robust estimated can be obtained by averaging the estimates of $\Delta\omega$ over an intensity range $[I_2, I_1]$, as shown in Equation (1-5).

$$\Delta\omega = \frac{1}{I_1 - I_2}\int_{I_2}^{I_1} (x_{base}(i) - x_{reg}(i))di$$

(1-5)

where $I_R \leq I_2 < I_1 \leq I_S$.

Equation (1-5) can alternatively be expressed as an integral with respect to *x* over the boundary, as written in Equation (1-6). Equation (1-5) and Equation (1-6) are equivalent by considering that both integrals evaluate the area of the shaded region in Figure 11.

$$\Delta\omega = \frac{1}{I_1 - I_2} \int_{boundary} (Clip(\, i_{base}(x), I_1, I_2) - Clip(i_{reg}(x), I_1, I_2))dx$$

(1-6)

where $I_R \leq I_2 < I_1 \leq I_S$, and $Clip(a; I_1; I_2) = \begin{cases} I_2 & a < I_2 \\ a & I_2 \leq a \leq I_1 \\ I_1 & I_1 > I_1 \end{cases}$

If we extend this strategy to three-dimensions and determine the integral numerically by evaluating the integrand at small sampling intervals, the volume change can be calculated as shown in Equation (1-7).

$$\Delta v = \frac{K}{I_1 - I_2} X \sum_{x,y,z \in \mathrm{E}} (Clip(I_{base}(x,y,z), I_1, I_2) - Clip\big(I_{reg}(x,y,z), I_1, I_2\big))$$

(1-7)

where *K* is the unit voxel volume, *E* is the set of voxels in the border region of the cord, $I_{base}(x; y; z)$ and $I_{reg}(x; y; z)$ are the voxel intensities on the registered baseline and follow-up scans at *(x; y; z)*, and the intensity range of the integral $[I_2; I_1]$ is referred to as the intensity window.

Finally, the evaluation of BSI requires the appropriate selection of an intensity window. The intensity window $[I_2; I_1]$ should be selected such that it falls entirely within the intensity transitions associated with the boundaries of the structure of interest.

When applied to MRI image, the two T1-weighted images are co-registered using an affine registration that correct for rotation, translation, scaling and minimize the standard deviation

of the ratio image [24]. The registered scans are then differentially bias-corrected [25] before calculating the BSI. The method defines a region that lies near the borders of the baseline and registered repeat brain masks. The BSI technique is based on integrating the differences in intensities over this region. Scan intensities are normalised by dividing each scan by its respective mean, calculated over the interior region. The intensities are bounded by a clipping function based on a pre-defined upper and lower intensity for each scan. Dividing the integrated differences by the span of the clipping function provides a measure of the global brain volume loss (Figure 11). The absolute scaling of the BSI (that allows a final % brain volume change to be estimated) is calibrated using manual measurements of brain volume on each scan. The Figure 12 shows an example of the entire workflow on a brain analysis.

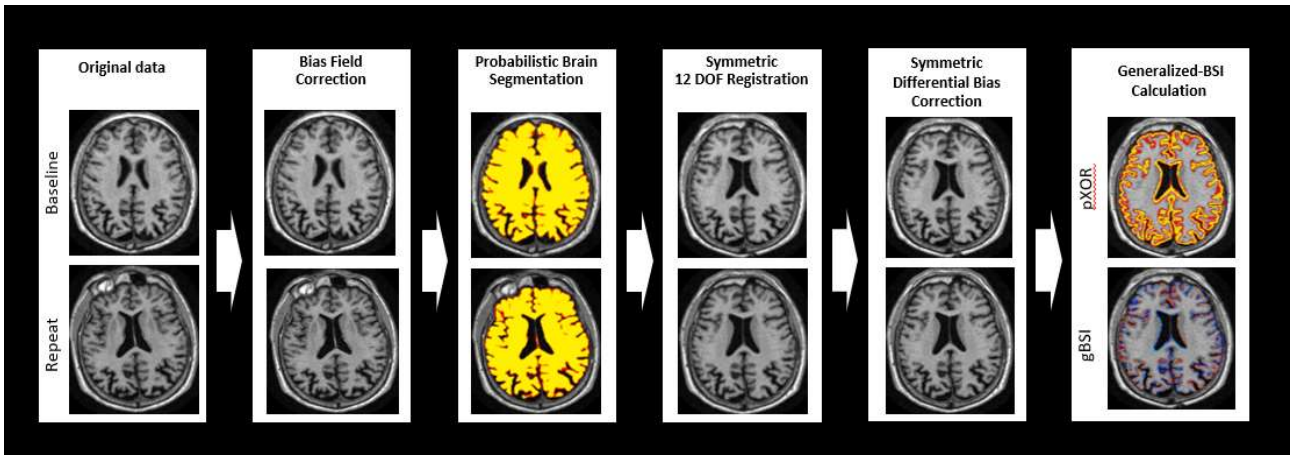

Figure 12: BSI pipeline. Source: Prados et al. 2015

1.2.3 Challenges in spinal cord imaging

MRI is also the method of choice in investigating disorders of the SC in a fairly quick and non-invasive fashion. Based on the magnetic properties of the hydrogen atoms, abundant in the human body in fat and water, various MRI contrasts may be generated and deliver anatomical detail, information on structural composition and tissue function [26–28]. For that purpose, a number of different MR-sequences and contrasts are used including relaxation time-weighted (T1, T2, T2*), proton-density weighted, magnetization prepared rapid gradient echo, fast-spin echo, phase-sensitive and short tau inversion recovery techniques [29].

However, in contrast to brain MRI, the environment of the SC presents additional challenges for MRI methods [26–28]. Greatest challenge is the inhomogeneous magnetic field across the SC due to the different magnetic properties of the surrounding tissues, e.g. CSF, fat, vertebral bones, and air-tissue interfaces. This may lead to image distortions and a loss of spatial resolution. Further, the SC is a fairly thin and curved structure with a maximal antero-posterior diameter of 8.3 ± 1.6mm at the C1 level and maximal latero-lateral diameter of 13.3 ± 2.2mm at the C5 level [2,30–33], which results in partial volume effects (a mix of tissues with different relaxation properties in one voxel) at the SC/CSF borders [26–29]. Another challenge is the cord's physiological movement in the spinal canal as a result of cardiac-induced pulsatile CSF motion, respiratory motion, and swallowing resulting in MRI motion artifacts [34–36]. Contact of the SC with some point of the osseous canal, which partially eliminates contrast between the SC and its surroundings further hampers assessment. Furthermore, osteophytes of the spinal column can cause focal changes in CSF flow dynamics within the spinal canal causing so

called CSF flow artifacts. Finally, so-called “Gibbs truncation artifacts” are very common in SC MRI resulting in high signal in the center and dark edges of the SC.

Another limitation is the currently insufficient contrast between SC GM, WM and CSF on conventional SC MRI. Only recently, advanced MRI sequences were able to overcome those obstacles providing images with sufficient signal- and contrast-to-noise ratios between SC compartments in 3 Tesla MRI machines.

Despite anatomical and methodological challenges, SC MRI is essential in clinical routine and can be generally assessed in two ways: qualitatively or quantitatively. Qualitative SC MRI assessment involves neuroradiologists searching for MRI signal intensity changes within the SC in order to distinguish normal SC tissue from focal intramedullar pathology such as demyelination, edema, or inflammation e.g. in MS lesions (Figure 13). This is currently the sole use of SC MRI in clinical settings. However, some of the disorders affecting the SC do not present with focal abnormalities in the sense of hypo- or hyperintense lesions on MRI but are rather characterized by neurodegeneration of various aetiologies leading to neuronal loss and shrinkage, Wallerian degeneration and axonal loss (e.g. spinal muscular atrophy, amyotrophic lateral sclerosis). Others do manifest with MRI intensity changes indicating inflammatory and demyelinating lesions, which -however- do not represent the entire underlying SC pathology and often do not serve as reliable biomarkers (e.g. MS, human-T-cell lymphotropic virus type-1 (HTLV-1) associated myelopathy). Nevertheless, the aftermath of those neurodegenerative and demyelinating processes is tissue shrinkage and can be assessed in vivo on MRI as SC volume loss. Hence, cross-sectional or longitudinal quantitative measurements of SC volume and/or CSA indirectly deliver additional valuable information regarding mechanisms of

neuropathology, that cannot be appreciated with the naked eye in qualitative assessments of SC MRI. Nonetheless, this is not part of clinical routine for the time being yet.

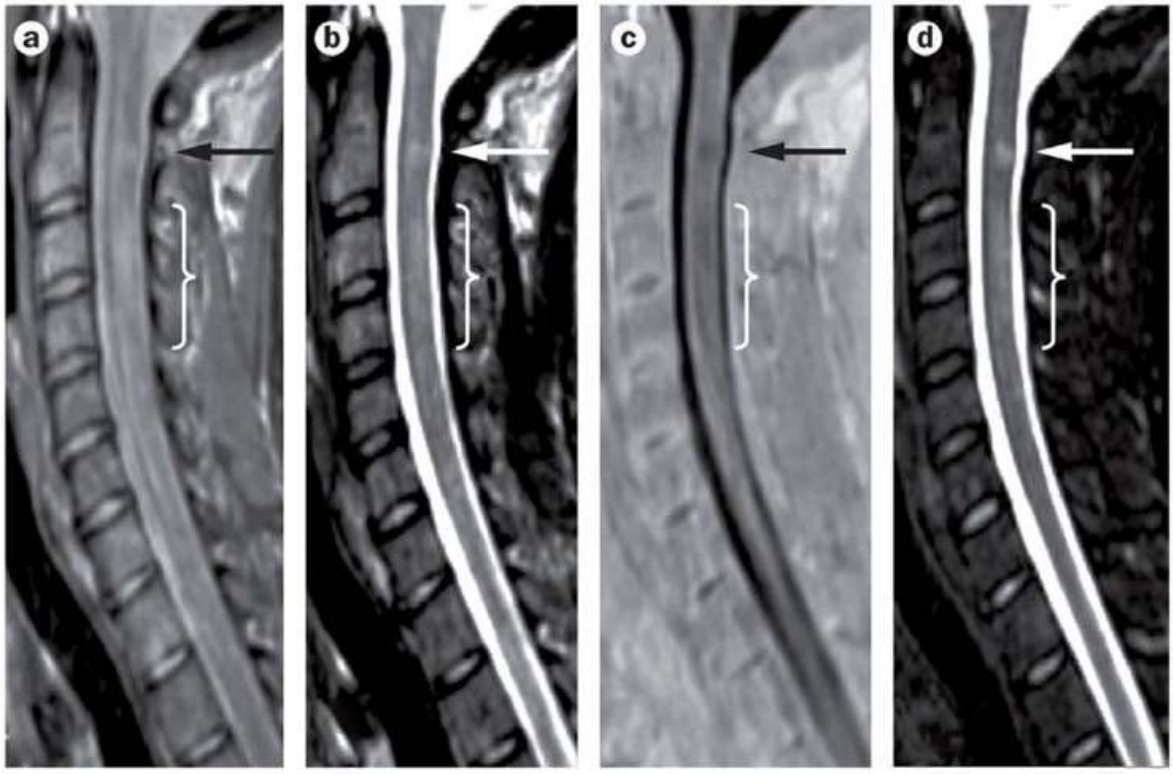

Figure 13: Multiple sclerosis SC lesions in sagittal images acquired with: a) Proton-density-weighted, b) T2-weighted, c) phase-sensitive inversion recovery and d) short tau inversion recovery imaging. Source: Tsagkas et al. 2019.

1.2.4 Brief overview of Spinal Cord methods

The purpose of this chapter is to present background information on SC image segmentation, laying the groundwork of our tool, SIENA-SC.

Implementing image segmentation techniques to quantify the SC volume and CSA have been introduced since 1996 [37]. Despite that, computer-based SC segmentation remains demanding in part due to limitations hampering SC MR-imaging (as mentioned in chapter

1.2.3). A big number of semi- and fully automatic techniques have been proposed [38]. The most important include active contours of surfaces [39–41], level sets [42], partial volume modeling [43], gradient vector flow [44], atlas-based approaches [45,46], and tubular deformable models with variable required user interaction from manual identification of the SC centerline [41] to the identification of multiple [40] or single [39,46] anatomical landmarks, with completely automated approaches presented only recently (Figure 14) [47]. In the past, SC atrophy was usually determined by assessing the CSA of the cervical cord, usually at the C2/C3 level, which has been shown to correlate with clinical measures, although reproducibility was limited and depending on data quality as well as repositioning [37,48,49]. However, until now only a few of those methods have been validated and/or evaluated on patient follow-up data to demonstrate the applicability in longitudinal trial settings with up to two years follow up time [37,41,47,50–52].

For the purpose of this thesis, chapter 1.2.4.1 presents the current most used and relevant segmentation-based methods, chapter 1.2.4.2 presents the attempts provided for the longitudinal SC atrophy estimation.

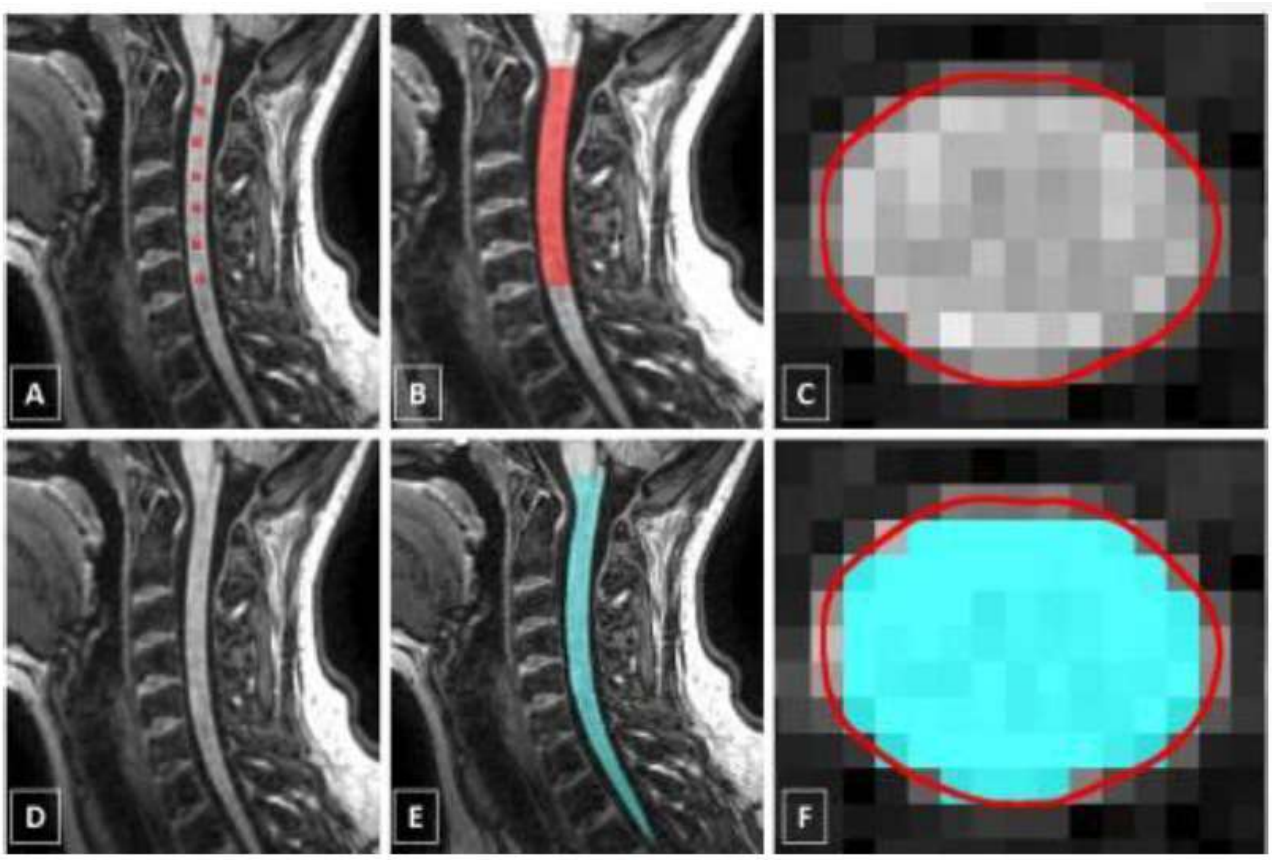

Figure 14: A-C shows a SC segmentation performed with an active surface method, while D-F demonstrates a fully automatic SC segmentation. Source: Yiannakas et al. 2016

1.2.4.1 Spinal Cord Segmentation method

The tools described in this section provide the CSA as metric of measurement. When using segmentation methods for longitudinal SC atrophy calculation, thus providing an indirect estimation, the rate of atrophy is estimated by numerical subtraction of SC CSA measurements calculated at different time-points. For instance, percent change of cord area is calculated using the following formula (1-8):

$$atrophy = 100 * \frac{(follow\ up\ area - baseline\ area)}{baseline\ area}$$

(1-8)

Years between baseline and follow-up scans can also be included in the denominator of the formula, if there is variability of the interval between scans [53,54].

1.2.4.1.1 Jim

Jim provide a toolbox for medical image analysis. Within the JIM tool, the ASM is a surface-based method that semi-automatically outlines the cord, after marking the centre of the SC [41,55]. The ASM has provided more prompt and repeatable measures of the SC volume, compared with manual methods [56]. The ASM offers a considerable reduction in user interaction time, and can be performed over long spinal segments. The user needs to identify landmarks at the extremes of the region to study, and, then, mark the centerline of the cord. Sagittally-acquired images are then reformatted to the axial plane to obtain five contiguous 3 mm slices; the program automatically calculates the radius and the centre of each axial slice and, finally, the CSA is obtained by averaging these contiguous slices [41]. Jim is not provided free of charge and it hasn't been used in this thesis.

1.2.4.1.2 Spinal cord toolbox

The Spinal Cord Toolbox (SCT) is a free open-source software dedicated to the processing of SC MR images. SCT contains a lot of functions for working on the SC in several different fields [57]. Most of the functions in the SCT are the state-of-the-art in their field. A lot of recent works in the SC domain have used the SCT in their research [58]. SCT works on Unix

environment. The tool is freely available at https://spinalcordtoolbox.com/user_section/installation.html.

In this thesis, we used SCT as the basis for the development of our tool for three main reasons.

First, the SCT proposes two algorithms for the SC segmentation and both of them are quite recent. The large amount of studies using the SCT to achieve their results is a good hint about the quality of the proposed algorithms [47,57,59]. Moreover one of those algorithms is based on deep learning techniques that allows a total automated segmentation also from brain MRI images.

Second, the segmentation algorithm inside SCT showed to have same sensitivity as the Active Surface Model (ASM) within JIM (https://www.xinapse.com/) but has higher inter-rater repeatability and is more time-efficient [47].

Third, the SCT and its algorithms are open-source and very easy to use. Moreover, it has an active community of developers which make sure that the SCT stays at the top of the current techniques.

1.2.4.1.2.1 Sct_propseg

This algorithm has been developed in 2014 by researchers from Polytechnique Montréal and the University of Montréal [59]. It is totally automatic and is designed to segment the entire SC (Figure 15).

The algorithm consists in the iterated propagation of a deformable 3D mesh which ends up corresponding to the SC. It is divided into two modules: the detection and the propagation module.

The detection module consists in finding SC position and orientation. The module is divided in three phases followed by a validation step. It starts by the automatic selection of an axial slice (e.g. the middle one). Using the symmetry of the body, the medial antero-posterior line that passes through the SC is detected. The medial antero-posterior line position is computed by maximizing the mutual information between the two parts of the image separated by the line (the line defines the middle of the symmetry). A restrained image is then created by cropping a region of 5 cm length in the left-right direction of the symmetrical line. Due to the circular shape of the SC, the second phase consist in performing a circular Hough transformation [60] on the cropped image. Since other circular shape structure can be present on the image only circles embedded in other circles are kept (the SC lies in the spinal canal). Note also that a stretching factor is applied on the Hough transformation in order to detect elliptical shapes which correspond more to the SC shape in certain parts. Finally those two steps are repeated on 10 axial slices, 5 rostral and 5 caudal to the starting plane (each separated by several millimeters) in order to improve detection rate. The neighbouring points (between different slices) of the detected structures are then connected. It is assumed the longest connected chain is the SC. In order to ensure the SC was detected, a validation step is executed. This validation uses a classification method based on easily computable metrics.

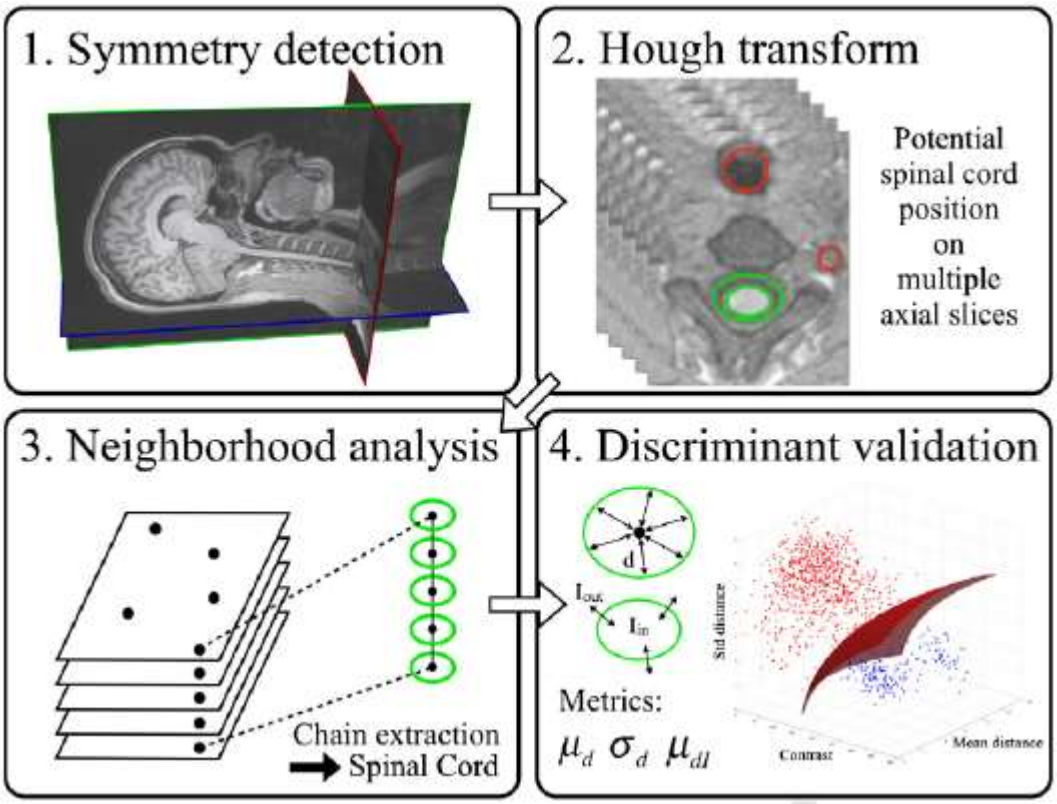

Figure 15: Workflow of the detection module. Source:Kaus et al 2003

Using the information collected in the detection module, a triangular tubular mesh is created. During the propagation module this mesh will be transformed to correspond in the best way possible to the SC. This iterative process is divided in two phases.

The first phase consists in selecting the most promising points where the mesh has to be deformed. The second phase consists in the use of active contour techniques where each selected point is displaced to minimize an energy function. Once the mesh is deformed one section M_i of it is duplicated and translated in order to propagate the mesh. A different energy term is maximized in order to determine the orientation of the mesh at the new points. The process is mainly inspired from the work of Kaus et al. [61]. For computational conveniences

the iterative process is first computed on a low-resolution mesh and second on a refined mesh interpolated from the first mesh once it has been deformed and propagated. This provides a complete automated algorithm for the segmentation of the SC (Figure 16).

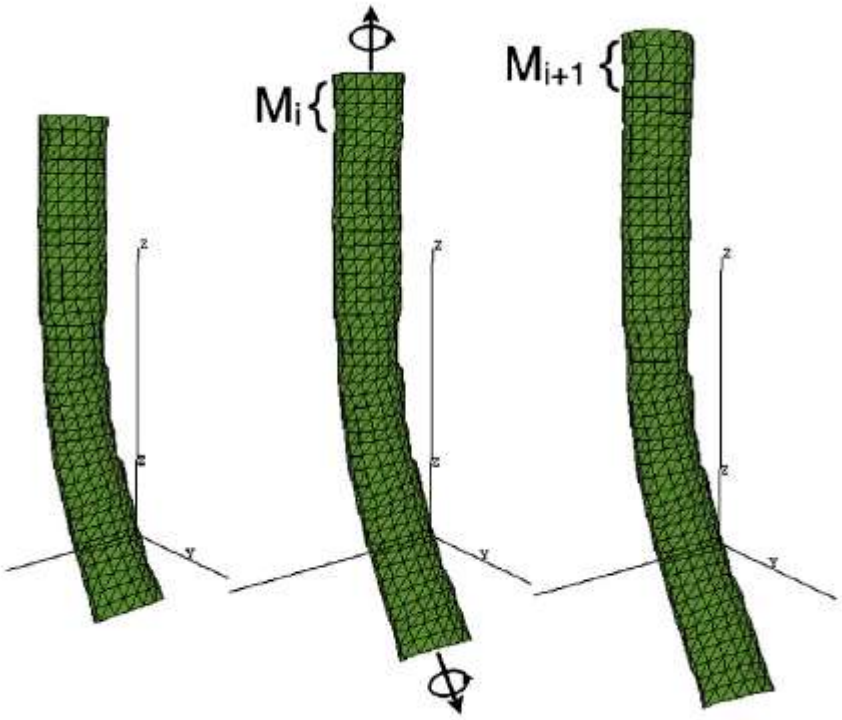

Figure 16: Propagation of the deformable mesh. Source: De Leener, Kadoury, and Cohen-Adad 2014.

1.2.4.1.2.2 Sct_deepseg

Researchers of the University of Montreal have developed in 2019 a new segmentation algorithm for the SC using deep learning and U-net architecture [62]. It contains also a model designed for the detection of SC sclerosis.

The new segmentation algorithm is divided in two different convolutional structures which are applied one after the other to the image.

On classical MR images, SC voxels represent less than 1% of the total amount of voxels. The role of the first CNN is to find the center of the SC such that the image is then cropped around it in order to remove the useless information. This CNN uses 2D convolution and is a slightly derivation of the classical U-net architecture (Figure 17). The number of downsampling steps is reduced from 4 to 2. This is possible because the conventional convolution are replaced by dilated convolution in the contraction section. A dilated convolution is a convolution which uses a sparse filter which provides an exponential expansion of the receptive view (the "window" of pixels that is scanned through the filter for each convolution). Due to the larger receptive view, this process captures more contextual information compared to a classical convolution with the same amount of parameters in the filter. As the dimensions of the feature maps will decrease quicker after each convolutional layer, it allows to use less downsampling steps . The CNN creates a prediction mask which indicates the degree of confidence each voxel is part of the SC. The centerline of the SC is then computed using OptiC. This is a fast globalcurve optimisation algorithm, which regularises the centerline continuity along the Superior-to-Inferior axis [63].

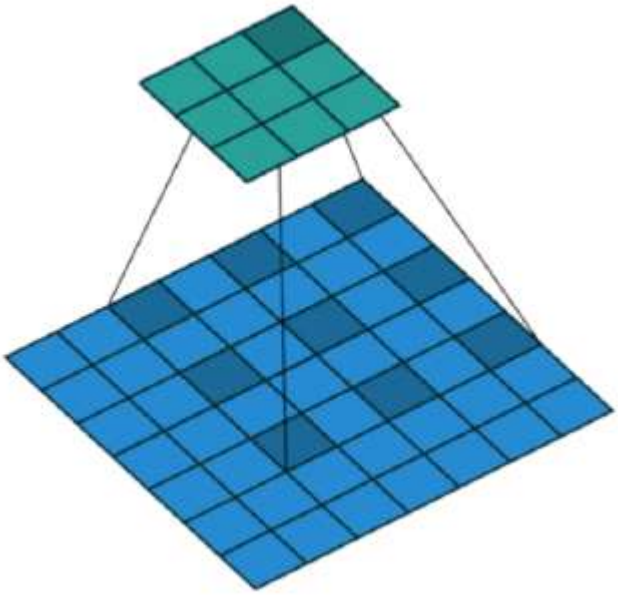

Figure 17: A 2D dilated convolution with a receptive view of size 5x5 and a filter of 9 parameters (output image in green). Source: https://towardsdatascience.com/types-of-convolutions-in-deep-learning-717013397f4d

The second CNN uses 3D convolutions and is computed in a volume around the SC centerline. From the volume, 3D patches of size 64x64x48 are extracted.

Intensity normalization is applied on the patches to homogenise the intensity distribution on standardised intensity range [64].

This CNN is a 3D derivation of the 2D U-net architecture, with 3D convolution[65]. The role of this CNN is to segment the SC. Its output is a binary mask with same dimensions as the input image. The full deepseg framework can be applied through a SCT function on NIFTI image and allows different options choices such as the contrast of the image.

The training has been divided by MRI contrast (T1,T2 and T2*) in order to make trained models available for each contrast. A dataset containing 1943 images (151 for T1, 904 for T2 and 888 for T2*) and coming from 30 different centers has been used for the training of the models. The training set contains very heterogeneous images in resolution and orientation which allows the algorithms to work on almost every MR image. An example of the cord detection module is showed in Figure 18.

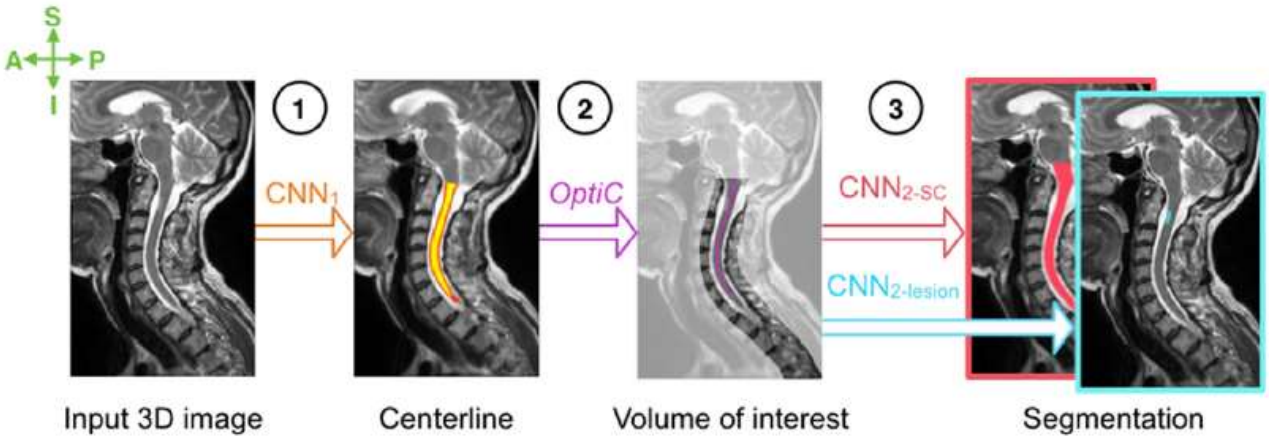

Figure 18: The journey of an image through deepseg. Source:Gros et al 2019.

1.2.4.2 Spinal Cord Registration method

Registration based methods have the great advantage of providing a direct estimation of the rate of atrophy. To date, GBSI is the only one freely available solution for longitudinally assessing SC using a pure registration-based approach [66].

1.2.4.2.1 GBSI

The GBSI is an extension of the BSI algorithm already used for the longitudinal brain atrophy estimation. The pipeline used to test the performance of GBSI is applicable to datasets with T1-weighted images (brain or dedicated spine acquisition), with identical acquisition parameters, ideally using 1 mm isometric voxels, at two time-points for each subject. A graphic overview of the pipeline is illustrated in Figure 19 and further detailed below.

The first step is the manual or automatic segmentation of the SC from T1-w images. Afterwards, the extracted masks are used to compute a ring surrounding the SC to scale the signal intensity of the images accounting for the presence of the noise floor [67]; for this step the signal intensities in the whole 3D volume are corrected using a fast version of the adaptive non-local means filter algorithm [68]. Then, an intensity inhomogeneity correction is applied to the 3D data using the N4 algorithm [69]. Once images are corrected for noise and intensity non-uniformities, both SC time-points are straightened using a specific software available within the SCT [70]. Both SCs are then registered to the half-way space using a symmetric, affine and inverse-consistent method [71]. To reduce the residual bias field and homogenise the grey scale between both registered time-points, a symmetric differential bias correction is applied [25]. Finally, the GBSI is computed on a voxel-by-voxel basis as the difference in intensity between the baseline and the follow-up image within a clipped window and can be obtained from the two k-means class values. The clipped window goal is to catch the difference between tissue intensities at the two time-points, reducing the background influence. Then the intensity differences are weighted by the probabilistic XOR mask voxel-wise. PCVC was

calculated by dividing the GBSI value by the binarized, straightened and registered baseline cord mask volume.

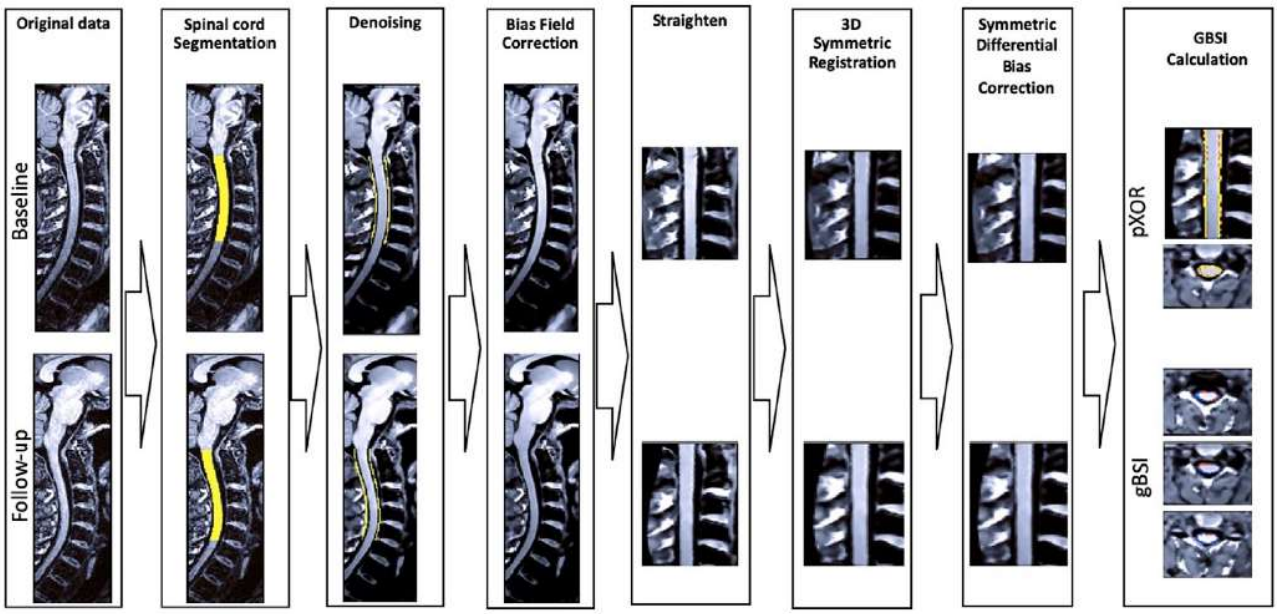

Figure 19: Pipeline for the longitudinal spinal cord assessment using GBSI. Source: Prados 2020.

1.2.4.2.2 Reg

The Reg method is composed of the following main steps: 1) initial segmentation, 2) image co-registration, and 3) final cord segmentation. The general workflow is illustrated in Figure 20.

The first part of the process is manual, then it will proceed in a total automatic way. The analysis starts when the operator puts the landmark to identify the approximate center line of the SC at both time points. The marking of the cord center is refined using an approach similar to that described by Gros et al [63]. The cord is then segmented using the AS method [41]. The cord masks obtained were then dilated by a distance of 2 mm, and an annulus surrounding the

cord was formed by an exclusive OR operation (XOR) between the original cord outlines and the dilated outlines in order to assess the signal intensities within the CSF surrounding the cord. The standard deviation (SD) of the CSF signal was used as a measure of the noise level in a nonlocal means noise reduction filter [72], which was applied to the original axial cord images before they were segmented once again using the low number of cord shape coefficients, but this time the segmentation was used to produce a straightened cord image of the region between the superior and inferior cord landmarks for both time points [41].

In the second step, the two straightened cord images are registered to a half-way space and a symmetric differential bias correction is applied [25]. At this point there is a further improvement where any slight residual misregistration along the cord are removed using an in-plane-only registration procedure with translations along x and y, and rotation on the z-axis.

Now the two straightened cord images are precisely aligned, with cord centroids at the origin in the straightened cord space, and the two registered straightened cord images were pixel-by-pixel intensity averaged, and the AS method was used to give initial approximate cord outlines. Then, these outlines were used to initialize the final cord segmentations of the two straightened cord images separately.

The overall mean PCVC between the most superior and most-inferior overlapping registered slices was calculated as the average of the values for the two images processed in forward and reverse order (1-9):

$$PCAC = (100 * \frac{(CSA_{FU} - CSA_{BL})}{CSA_{BL}}$$

(1-9)

where CSA_{BL} is the mean cord CSA in the baseline image and CSA_{FU} is the mean cord CSA in the follow-up image.

Although it falls into the category of registration-based tools, the final computation of atrophy is done in the same way as segmentation methods.

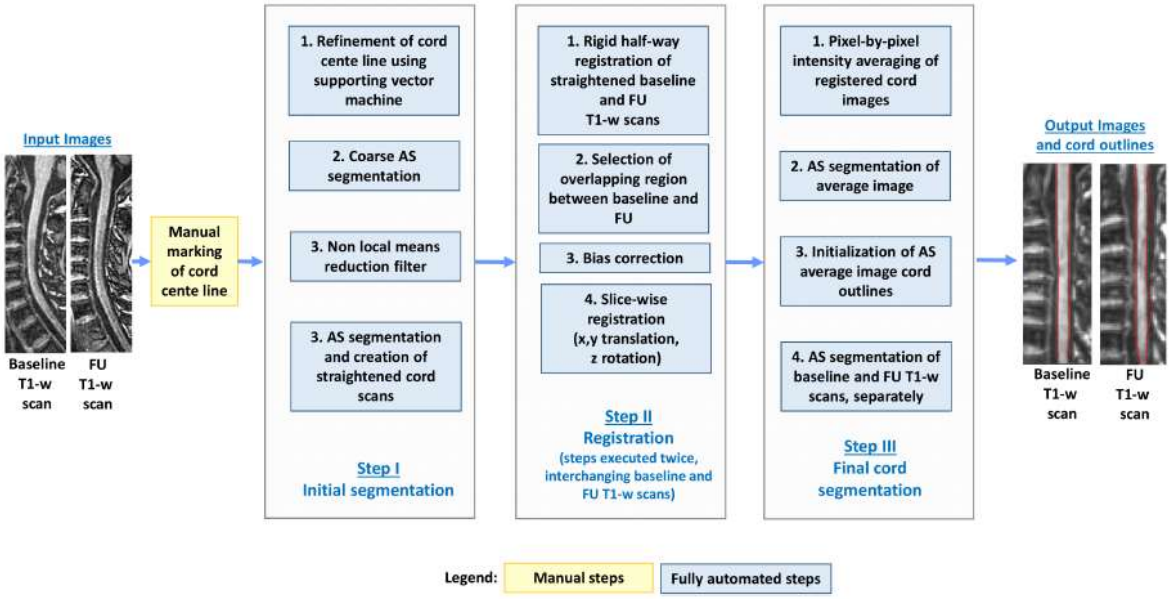

Figure 20: Schematic representation of the main steps of preprocessing performed by the registration (Reg) method on pairs of 3D T1-weighted baseline and follow-up scans. Manual and fully automated steps are represented in yellow and light blue boxes, respectively. FU = follow-up; AS = active surface. Source: Valsasina et al 2015.

1.3 Role of spinal cord in neurological diseases

The SC is affected by inflammatory and neurodegenerative processes leading to irreversible tissue loss in several neurological conditions, such as MS [54], NMO [73–75], and human T-lymphotropic virus 1 (HTLV-1)-associated myelopathy/tropical spastic paraparesis [76]. Moreover, SC atrophy is associated with more severe clinical features in amyotrophic lateral sclerosis [77–79], SC injury [80], and Friedreich's ataxia [81], and with worse recovery from SC surgery [82]. There is also preliminary evidence of SC atrophy in Alzheimer's disease [83], and in Huntington disease [84], suggesting that SC atrophy can be part of more widespread neurodegenerative diseases.

In one study involving 19 patients with SC injury, SC atrophy was shown to correlate with motor and sensory deficits [85].Notably, Lundell et al. showed that anterio-posterior width (APW) and left right width (LRW) of the cord can be used to assess sensory and motor function independently. In another study, atrophy was shown to correlate with American Spinal Injury Association (ASIA) score in a chronic SC injury population, independently from DTI and magnetization transfer measurements[86]. SC atrophy has also been demonstrated in patients with amyotrophic lateral sclerosis [87]. Notably, Cohen-Adad et al. showed an association between muscle deficits and local SC atrophy, suggesting that atrophy is a sensitive biomarker for lower motor neuron degeneration. The authors tested the specificity of atrophy at a given vertebral level (between C4 and C7) in relation to muscle deficits and motor-evoked potentials using a stepwise linear regression model. They demonstrated that deficit of the deltoid muscle (at the C5 spinal level, equivalent to the C4 vertebral level) was associated with atrophy at the C4 vertebral level, and that deficit of the abductor pollicis brevis or adductor digiti minimi (at

the C8 spinal level, equivalent to the C7 vertebral level) was associated with atrophy at the C7 vertebral level.

In MS, SC atrophy is one of the long-term sequelae, particularly in the most disabling forms of the disease, with the cervical cord being most affected. The main cause is thought to be Wallerian degeneration as a result of changes that occur in the brain, rather than tissue loss due to primary cord pathology. However, only moderate correlations have been found between cervical cord atrophy and conventional and advanced MRI measures of brain damage [88,89], suggesting that degenerative and inflammatory processes typical of MS affect the cord and the brain with dynamics that are partially independent. As explained previously, the SC is the main pathway for information connecting the brain with the peripheral nervous system, thus SC atrophy has a major impact on patients' clinical status.

Since we validate our software using MS subjects, the following paragraph 1.4 will be dedicated on the MS pathology.

1.4 Multiple Sclerosis

1.4.1 Introduction

MS is a chronic inflammatory demyelinating and neurodegenerative disease of the CNS, potentially causing any neurological deficit [90,91]. Previous studies have implicated a combination of genetic and environmental factors in the-pathogenesis of MS, with chronic inflammation and neurodegeneration mediated by the patient's immune system [92,93].

1.4.2 Epidemiology

According to the most recent Global Burden of Disease Study estimates (2016), MS is the most common immune-mediated disease of the CNS, with over 2.2 million cases world-wide, corresponding to 10% increased prevalence from 1990 [94]. North America, Western Europe and Australasia hold higher prevalence rate (91-164 cases per 100,000), compared with Africa (2-3 cases per 100,000) [94]. On the contrary, incidence of MS has been relatively stable or slightly increased over the past four to five decades [94]. As such, the rising prevalence mostly reflects improved survival, with a global mortality rate for MS being decreased by 11% between 1990 and 2016 [94].

Clinical onset is generally in early adult life, though there is increased awareness of presentation in childhood [90]. Prevalence of MS is similar in preteen boys and girls, but progressively increases through lifetime among women, with a 2:1 sex ratio in favor of women in the sixth decade of life [94]. As discussed above, the life expectancy for a person with MS is relatively unimpeded by the disease, with a 5 to 10-year reduction versus non-affected individuals [95]. However, MS is one of the leading causes of disability from CNS disease among

young adults, and has a severe impact on quality of life, made further strenuous by a relatively young average age of onset [90,94].

1.4.3 Pathology

The most typical pathology signs of MS is the presence of demyelinating lesions in the WM and GM, in the brain and in the SC [96–100]. Demyelinating lesions generally originate around venules, where accumulation of inflammatory lymphocytes can be observed [101,102], along with astrocytic response and macrophages/microglia infiltrates to the active injury site, eventually resulting into gliotic scars [103]. Acute inflammatory demyelination is clinically associated with the acute onset of new neurological symptoms (i.e., clinical relapse) [104–106].

Neuro-axonal loss is another prominent hallmark of MS and is a key factor of irreversible disability accrual [107]. In the early stages of the disease, axonal loss is generally seen in areas of pathological demyelination, in association with inflammatory infiltrates consisting of macrophages/microglia and lymphocytes [108]. During the course of the disease, axonal loss can occur in areas of prolonged demyelination without active inflammation, suggesting that axonal survival is related to the presence of myelin support [109–112]. Notwithstanding this, the presence of chronically demyelinated axons suggests that demyelination does not necessarily leads to neuro-axonal loss [110,113,114]. In advanced MS, axonal loss results into shrinking of the brain parenchyma (i.e., atrophy), and is associated with impaired function of macrophages/microglia and astrocytes, and with increased oxidative stress and mitochondrial damage. In particular, demyelination and subsequently impaired axonal dysfunction increase

the energy demand, further contributing to altered metabolism, neuronal dysfunction and, ultimately, axonal loss [115–117].

The mechanisms by which demyelination and axonal loss occur are profoundly heterogeneous and involve a variety of cellular subsets [90,118,119]. The sequence of pathological events might include perivenular infiltration of macrophages, CD8+ T lymphocytes and CD4+ T lymphocytes and B lymphocytes, with profound blood brain barrier (BBB) leakage, giving rise to classical active demyelinated plaques [119–124]]. As the disease progresses, infiltrates of T and B lymphocytes, activation of microglia/macrophages and astrocytes, and mitochondrial dysfunction become obvious throughout the brain parenchyma, also in the absence of major BBB damage [120,125], with formation of aggregates of inflammatory cells in the form of meningeal follicle-like structures, and expansion of previously-existing WM and GM lesions [116,117,119–121,126–129] . These changes ultimately lead to progressive demyelination, axonal loss and neurodegeneration in the brain and the SC [116,117,119,126,129] .

Inflammation, demyelination, and axonal loss can be measured *in vivo* by using MRI [130].

1.4.4 Imaging biomarker in MS

During the last 20 years, over a dozen DMTs received the approval for the treatment of RRMS, being facilitated by screening the anti-inflammatory activity of putative treatments using active MRI lesions as outcomes in phase 2 trials [131,132]. On the contrary, the paucity of active medications for both PPMS and SPMS is striking [90,133]. In view of this, the Progressive MS Alliance recently suggested to develop and validate biomarkers of progression that could make clinical trials for progressive MS less time and resource-consuming, when compared with

conventional clinical measures [134]. This could be achieved with the identification of reliable, repeatable and sensitive-to change imaging outcomes [54,135].

Several brain MRI measures are able to reflect the inflammatory and neurodegenerative pathology of MS [136,137]. Brain lesion count and volume are robust markers of inflammation and demyelination, and are important outcomes in both RRMS and progressive MS trials [9]. Following recent improvements in analysis methods, brain atrophy has gained relevance, in light of its strong association with disability accrual [9,135]. Advanced brain MRI techniques, such as magnetization transfer ratio (MTR), diffusion tensor imaging (DTI) and magnetic resonance spectroscopy (MRS), have been included in few trials so far, and hold promise for the future, as they can reflect specific pathological changes targeted by neuroprotective treatments, such as improved myelination measures within lesional tissue, following treatment [135,138]. Positron emission tomography (PET) and optical coherence tomography (OCT) are also emerging as candidate imaging outcomes of MS progression [135].

More recently, improvements in MRI acquisition protocols and post-processing have overcome some of the limitations associated with imaging the SC, a small and mobile structure at risk of motion artefacts from breathing, cardiac movement, CSF pulsation and blood flow [53,54]. Conventional SC MRI provides information on focal lesions, which are necessary for the diagnosis and prognosis of MS and is commonly used in the clinical setting [9,139]. SC volume loss is the result of demyelination, neuro-axonal loss, oligodendrocyte damage, and gliosis, ultimately resulting in chronic motor, sensory and autonomic dysfunction [37,140], and will be at the very centre of this thesis. Advanced SC MRI techniques assess the type and extent of SC

abnormalities, but, as discussed below, their use is currently limited to specialized centres for research purposes [54].

Overall, looking at the paradigm of treatment development for PPMS and SPMS, the number of imaging outcomes included in clinical trials has almost doubled from 2.3±1.5 in the decade 1996- 2006, to 4.1±2.6 in most recent years (2007 to current) [135].

1.4.5 Role of spinal cord imaging in MS diagnosis

The 2017 revised McDonald criteria confirmed that MRI is the most useful paraclinical test to aid the diagnosis of MS and can be used to establish dissemination of lesions in space (DIS) and time (DIT) [141]. The SC is one of the four areas of the CNS where lesions with characteristics typical of MS are scored to confirm DIS. Prior to the 2017 McDonald criteria, only asymptomatic SC lesions were scored for DIS, which led to the high specificity of the DIS criteria; in order to facilitate the scoring of the criteria, and avoid discussing which lesion is the symptomatic one in cases of multiple lesions occurring in the same CNS location, the 2017 revised criteria do not distinguish anymore between symptomatic and asymptomatic lesions when testing the DIS criteria. In particular, the inclusion of SC symptomatic lesions for DIS or DIT increases diagnostic sensitivity, with little or no reduction in specificity [142–144].

Whilst brain MRI is recommended in all patients who are undergoing investigations for the diagnosis of MS, SC MRI is advisable when: (1) The clinical presentation suggests a SC lesion; (2) The clinical presentation is suggestive of PPMS; (3) Brain MRI is normal, but there is a strong clinical suspicion of MS; (4) Brain MRI findings are inconclusive (e.g., age-related vascular changes) [141,145,146]. Therefore, SC MRI is generally recommended in patients with SC CIS and in those with non-spinal MS not fulfilling the DIS criteria. It is debated whether all the

remaining CIS patients, who have non-spinal MS and fulfil DIS criteria on brain MRI brain, should undergo SC MRI [147].

More recently, patients with clinical features typical of MS, but showing evidence of pathology exclusively in the SC, even with a single lesion, and whose MRI does not fulfil the DIS criteria, have been described as two novel clinical entities: (1) Progressive solitary sclerosis, when insidiously progressive upper motor neuron impairment can be attributed to an isolated demyelinating lesion within the CNS (within the SC in 90% cases) [148]; and (2) Pure spinal MS, when relapsing episodes of short-segment myelitis occur over time, in the absence of typical brain or optic nerve lesions [149]. Progressive solitary sclerosis and pure spinal MS are proposed novel MS phenotypes, characterised by a predominant SC pathology. Myelocortical MS is another suggested pathology subtype of MS where axonal loss in the WM occurs in absence of obvious demyelination, but is still lacking further pathology and clinical validation [113].

1.4.6 Spinal Cord Atrophy in MS

SC atrophy is a common and clinically relevant aspect of MS. An increasing number of studies have focused on the importance of SC atrophy as a biomarker of disability progression and as an outcome measure in clinical trials.

SC atrophy is the consequence of different pathological processes, including axonal transection and associated neuro-axonal loss, demyelination, loss of oligodendrocytes, gliosis, and, ultimately diffuse tissue injury [98,99,150–154]. Although these pathological abnormalities occur within focal lesions, extensive tissue abnormalities are also present in the normal-appearing SC of MS patients, and this finding may explain why SC atrophy occurs

independently of SC lesions [98–100,110,155–158]. Additionally, SC atrophy also occurs, at least in part, independently of brain pathology [156,159,160].

SC atrophy is generally measured as CSA at the cervical level, which is least affected by movement artefacts, yields the most reproducible results, and provides the best clinical correlates [161–165]. The most common levels are C1-C2 and C2-C3, but measurements can be also made between C1 and C7 [166]. Atrophy assessment can be done on a variety of sequences, mainly 3D T1-weighted and T2*- weighted gradient echo sequences on different MRI scanners (e.g. Philips, Siemens, GE) [37,41,167].

1.4.7 Spinal cord atrophy in disease phenotypes

SC atrophy occurs even in early stages of MS and has been detected in patients with CIS [167–170]. In CIS patients who were followed-up for 5 years after onset, the lowest rate of SC atrophy (-0.1% a year) was observed in those who remained CIS, whilst the highest rate (-1.4% a year) was detected in patients who developed MS and had an EDSS at the last time point equal or greater than 3 [171]. In general, a high rate of SC atrophy is observed in the progressive forms of MS, especially SPMS (-2.2% per year) [150,166,169,170,172]. Overall, in clinically-definite MS, the rate of cord atrophy has been reported to vary between 1 and 5% per year [37,150,173–175]. A multicentre study has detected a rate of -1.22% per year in patients with stable MS and -2.01% in patients who deteriorated over time [166]. Interestingly, there is a significant development of SC atrophy in early PPMS patients when compared with healthy controls over only 1-year follow-up, but not in patients with established SPMS, who had a higher disability and more atrophic cord than early PPMS patients [176]. Although the rate of atrophy may vary slightly between studies, because of different cohorts and different

methods, it is consistently higher than the rate of brain atrophy, which is known to be around -0.5% per year in MS patients [177]. A recent meta-analysis of twenty-two longitudinal studies assessing SC atrophy in all MS subtypes revealed a pooled rate of SC atrophy of -1.78% per year, that increased to - 2.08% per year when considering progressive patients alone [161].

Only few studies have examined cervical cord atrophy in NMOSD and reported conflicting results. Some studies found more pronounced SC atrophy in AQP4 positive patients than MOG patients [73], and in MS than NMOSD [74], whereas another study found similar reductions of CSA in NMOSD and MS [75].

1.4.8 Spinal cord atrophy and MS disability

Several studies have shown associations between: (1) the extent of SC atrophy at a single time point and concurrent disability [178], and (2) the rate of SC atrophy over time and disability progression [51,89,167,170,179,180]. A recent study has reported that every 1% increase in the annual rate of SC volume loss is associated with a 28% risk of developing disability progression in the subsequent year [181]. In a longitudinal cohort of non-spinal CIS, upper cord cross-sectional area (UCCA) decrease was associated with 5-year increased disability, measured by EDSS [180]. Overall, SC atrophy can account for 77% of disability progression after 5 years [171,178,182]. Within EDSS, the sub-scores that reflect the neurological functions mediated by SC pathways, such as the pyramidal, sensory, bowel and bladder functional scores, correlated with SC atrophy [52]. Higher SC atrophy rate is associated with worsening of more specific measures of motor disability, such as the 9HPT and the T25FWT [178,181]. Associations between the development of SC atrophy and disability progression are particularly strong in PPMS [172].

1.4.9 Spinal cord atrophy in clinical trials

Since SC atrophy rates are two-to-three times higher than brain atrophy (-1.78% vs -0.5% per year), in particular in progressive MS [161,183], and the SC is a very eloquent site of pathology in MS, SC atrophy has been considered as an exploratory outcome measure in phase 2 and phase 3 clinical trials, especially in patients with progressive MS, although much less frequently than brain atrophy [9]. However, clinical therapeutic trials that incorporated SC atrophy as an outcome measure did not demonstrate beneficial drug effects on this metric [184–186]. In addition to the possibility that the medications tested were not effective, there may be other reasons for these negative results, related to methodological difficulties of calculating SC atrophy; these include: movement artefacts and subsequent image noise; the limited spatial resolution of MRI scanners, which is an important issue, given the small cord size; multicentre design, with inter-site variability related to the use of different scanners with different acquisition settings; and inter-study variability related to the use of different methods to calculate SC area [187,188]. Also, SC normalisation using the intracranial volume, which aims to reduce the effect of biological conditions unrelated to the disease, has been suggested [50,162,163], but it is not always performed.

There have been encouraging results from a recent, single-centre, study employing SC atrophy [176,188]. If patients at the early stage of PPMS, with mild disability and a non-atrophic cord are selected, the sample size necessary to run a trial over only 1 year is achievable [176].

2 Aims of thesis

Identifying reliable imaging outcome measures is a cornerstone for improving the understanding of the disease mechanisms and for monitoring the clinical course of neurological diseases and its response to treatment [9,54].

Against this background, this thesis will focus on:

1) Develop a novel method, SIENA-SC, for the longitudinal assessment of SC atrophy by adapting a well-established registration-based method already use for the quantification of brain atrophy. The entire pipeline is fully described in Chapter 3.
2) Test the robustness and the reliability of SIENA-SC on a cohort of HCs. Hereby, we compared precision and repeatability of SC atrophy measurements obtained with one segmentation method (CSA change obtained with sct_propseg), a registration-based methods (GBSI) and our novel registration-based method. The experiment is fully described in Chapter 4.
3) Validate SIENA-SC using a cohort of pathological subjects and evaluate SC atrophy as a potential valuable biomarker. This experiment is presented in Chapter 5 and consists of the application of SIENA-SC to a cohort of MS subjects to further evaluate the ability of the software to discern physiological and pathological rate of atrophy and its treatment effect with the study of the sample size. Results will be compared among the three methods, SIENA-SC, GBSI and CSA change.

Finally, Chapter 6 summarizes the development of SIENA-SC, the limitations of the study and possible future directions.

3 Proposed Methods: SIENA-SC

SIENA-SC [189] is applicable to T1-weighted brain images, with identical or similar acquisition parameters, ideally using 1 mm isometric voxels, at two time-points for each subject. A graphic overview of the pipeline is presented in **Errore. L'origine riferimento non è stata trovata.** and further detailed below.

3.1 Step 1: Cropping the field of view of brain images

The first step is intended to constrain the field-of-view (FOV) of the input images to the SC area. In order to do this, we choose the brainstem from the MNI atlas as the neurological reference of the bounding box to crop the FOV of the images. The brainstem was resampled from the atlas in MNI space to the native T1-weighted images and then eroded 5 times. The last slice of the masks was taken as a reference point to remove all the regions above the bottom of the brainstem. This step was performed to isolate the cord section and to improve the performance of the segmentation and the following registration step of the SC.

3.2 Step 2: Spinal cord segmentation

The crucial step to obtain a total automated pipeline is the automated localization of the SC. For the purpose of this study and to avoid any manual intervention we used the fully automatic deep learning algorithm provided by SCT library (sct_deepseg) [62] described in chapter 1.2.4.1.2.2. This segmentation is computed separately and independently for each time-point, over all the visible SC. The obtained cord masks were used as input to perform intensities correction in step 2.

3.3 Step 3: Image Denoising

The extracted masks serve the purpose of computing a ring surrounding the SC, allowing for the scaling of signal intensity in the images while considering the presence of the noise floor [67]. To achieve this, the original T1-weighted images undergo denoising using a fast variant of the adaptive nonlocal means filter algorithm. This denoising process employs the mask derived from the segmented SC [68]. Specifically, the standard deviation of the signal within a ring located in the CSF is calculated to determine the root power of the noise, which is then used to account for the existence of a noise floor. To ensure accuracy, any voxel values within the extracted ring that exceeded 2 standard deviations above the mean were disregarded. This step prevents the inclusion of values originating from nerve roots or other erroneous signal intensities. Finally, the ring within the CSF was derived by dilating twice the SC mask, followed by the subsequent subtraction of the mask itself.

3.4 Step 4: Image inhomogeneity correction

The 3D MRI data undergoes an intensity inhomogeneity correction using the N4 algorithm [69], specifically within the region defined by the two-time dilatation of SC masks. The correction process incorporates the following parameters: full width at half maximum (FWHM) of 0.05, a convergence threshold set at 0.0001, and a maximum number of iterations capped at 1000 [14]. This application of the N4 algorithm ensures that intensity variations within the SC region are appropriately addressed and mitigated.

3.5 Step 5: Repetition of Spinal Cord segmentation

In order to enhance the segmentation accuracy and minimize bias caused by significant change in intensities caused by MRI artifacts between scans, we repeated the segmentation on the denoised and inhomogeneity corrected input images using a propagation segmentation algorithm [59]. To facilitate this process, we used the SC centerline derived from the previously computed masks as the input for the method.

3.6 Step 6: SC straightening

To eliminate any variations in cord curvature between time-points caused by positioning in the scanner, we employ a reliable and precise approach to straighten the MRI images. This involves utilizing the SC segmentation previously computed and employing a robust and accurate tool part of the SCT software package [57,70]. This approach preserves the SC's topology, crucial for measuring even the most delicate alterations in SC edges when employing SIENA-SC.

3.7 Step 7: Half-way space registration

To prevent the introduction of biases that may arise from registering one time-point to another, the images are registered to the halfway space through an affine transformation [16,190,191]. This step employs an inverse-consistent and symmetric algorithm [71]. The SC mask dilated until covering the vertebrae is used to provide a non-moving reference in the registration algorithm. After acquiring the transformations, both the images and their corresponding masks from each time-point are linearly resampled to the shared halfway space using a nearest neighbor interpolation. This ensures accurate alignment and facilitates subsequent analyses by establishing a consistent reference frame.

3.8 Step 8: Refinement of the resampled cord masks

Two additional refinements of the SC masks were performed at this stage. First, as resampling a mask into a different image space could result in loss of accuracy, we performed a smoothing of the border of the masks using a diamond-connectivity of the voxels. Second, the resampled segmentation masks on the halfway space were merged and the longer mask not covering the cord region in both images has been cut. In this way we are sure that the masks cover the same length between the two timepoints. This was performed because the SC section can vary by the number of slices between timepoints (e.g. different orientation, different positioning of the subject in the scanner), thus the final computation is performed on the same region of interest.

Finally, the obtained masks were then transferred to the algorithm for the computation of the atrophy.

3.9 Step 9: Atrophy computation

As a final step, the PCVC was estimated between the two aligned cord images following SIENA algorithm principles. To achieve this, the mean perpendicular surface motion from the generated edge points masks were estimated ignoring the flow in z direction (in order to have a 2D evaluation of atrophy along the cord) and finally converted to a PCVC.

To make the PCVC estimation robust, SIENA method internally corrects for possible small differences on image resolution and/or misalignment by calculating a calibration factor. Briefly, two PCVCs are calculated between the original image and a couple of artificial images obtained by varying the dimension of voxels (one increasing and one decreasing from the same scale

factor). These two PCVC are then averaged. Given that the “nominal” PCVC is known, once fixed the scale factor, a calibration factor can be obtained by dividing the “nominal” changes by the averaged PCVC. Now, given that the calculated PCVC depends also on the number of edge points and that this number is roughly 100 smaller for SC than for brain image, we accordingly changed the scale factor by dividing for 100. The rationale of this approach in described in the next chapter 3.10.

To increase robustness, the “forward” and “backward” PCVC was calculated for each pair of images swapping baseline and follow-up images. The average value of the “forward” and “backward” atrophy results was the final PCVC.

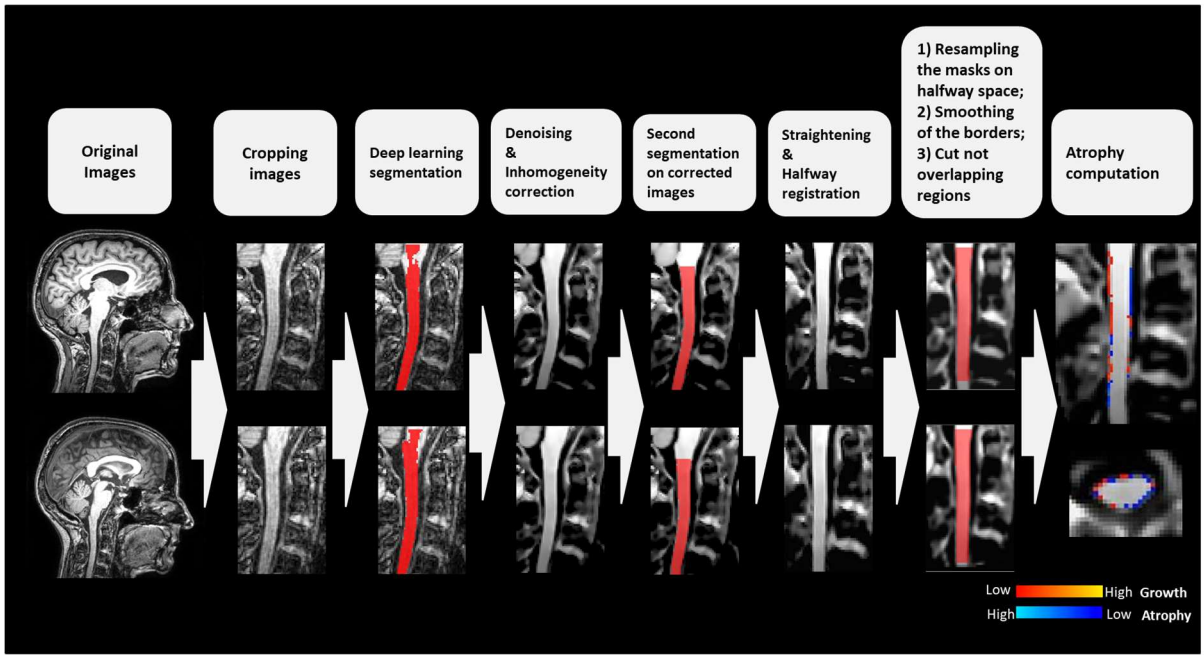

Figure 21: SIENA-SC image processing pathway.

3.10 Calibration Factor

To find the correction factor relating the self-calibration used in the brain atrophy estimation with that used for SC atrophy, we employed the math already exposed in Smith et al. [7] and explained in chapter 1.2.2.1.

In detail, the f_b self-calibration of the brain is comprised between 0.1 and 0.2 mm^{-1} and it is related only to the actual area of studied surface following the formula:

$$pbvc = \frac{100lA}{V} = \frac{100lfV}{V} = 100lf$$

(3-1)

where l is the mean surface displacement of the border, *A* and *V* are the brain surface and volume and *f* is the self-calibration for the brain.

Given that *f* is independent from volume, to assess the f_{sc} for SC we have simply made the ratio between the area of SC and area of brain from 100 randomly selected healthy volunteers of our population.

From the brain mask volume as obtained with BET, we derived the "nominal" radius of the brain (r_b), by approximating the brain itself to a sphere.

From this value, we obtained the brain surface (s_b) following this formula:

$$s_b = \frac{(r_b - 1)^3}{{r_b}^3}$$

(3-2)

From the actual volume of SC, derived by mask obtained from SCT and using $L_{sc,}$ the length in mm of the SC mask we obtained the "nominal" SC radius r_{sc} and from this the nominal SC surface s_{sc}.

$$S_{sc} = L_{sc} * \pi(r_{sc}^2 - (r_{sc} - 1)^2)$$

(3-3)

Finally, the correction factor between the self-calibration of the brain and the self-calibration of SC has been obtained averaging S_{sc}/S_b.

This value ranged from 0.01 and 0.02 and we opted for using a correction factor of 0.01, thus $f_{sc} = 0.01 * f_b$.

4 Experiment 1: Robustness

The first experiment concerns the study of the robustness of SIENA-SC compared with other two methods, GBSI and CSA change, to evaluate the longitudinal SC atrophy.

4.1 Population

We used two different MRI datasets (Table 1):

1. A single centre test dataset with HCs acquired twice on the same day to assess the reproducibility of the atrophy measurements. In this dataset it is expected to see an absence of cord atrophy.
2. A longitudinal multi centre dataset with HCs.

4.1.1 Scan rescan dataset

Thirteen healthy subjects (mean age: 39 ± 9,4 years) underwent a brain MRI acquisition using a 3 T Philips at Meyer Hospital in Florence. For each subject the MRI scans were acquired twice on the same day with repositioning of the subject in-between acquisitions. 3D T1-weighted brain images were acquired in sagittal orientation with 1mm isotropic voxel. The goal of the use of this dataset was to assess the *scan-rescan* repeatability of the automated software. We compared the PCVC measurement evaluated with SIENA-SC, GBSI and CSA change.

4.1.2 Healthy Control dataset

190 multicenter subjects (mean age: 74 ± 5,7 years) with an average follow-up of 1,2 ± 0,2 years freely available from ADNI website (https://adni.loni.usc.edu/).

All subjects had two brain 3D T1-w images acquired using a 3T MRI scanner, sagittally oriented and with 1 mm isotropic voxel.

	Number (Female)	Mean (SD) Age, years	Mean (SD) Follow-up
Scan-rescan dataset	13 (6)	39 ± 9.4	0*
Healthy Control dataset	190 (99)	74 ± 5.7	1.2 ± 0.2

Table 1: Population demographic

4.1.3 Statistical analysis

The statistical analysis was performed using MATLAB Release R2020a. Significance level was set to $P < 0.05$. The results are shown in mean, standard deviation, and standard error. All the atrophy measurements were yearly normalized before performing statistics, except for the scan-rescan dataset.

Paired t-student was employed to compare PCVC in scan-rescan dataset.

Pearson's correlation has been used to evaluate the degree of concordance between the different measurements obtained by the different methods. The Bland Altman plot was used to test for the presence of systematic bias.

PCVC obtained from CSA measurements was calculated as the CSA difference between two consecutive time-points CSA, divided by the first time-point and multiplied by 100.

4.2 Results

4.2.1 Scan - rescan dataset

SIENA-SC showed lower measurement error (mean: -0.06%; SD: ±0.18; SE: 0.03) compared to GBSI (mean: -0.12%; SD: ± 0.73; SE: 0.13 ; p<0.005) and CSA change (mean: 0.58%; SD: ± 2.2; SE: 0.32 ; p<10E-10). GBSI showed lower measurement error compared with CSA (p<0.01). SE: Standard Error. (Figure 22).

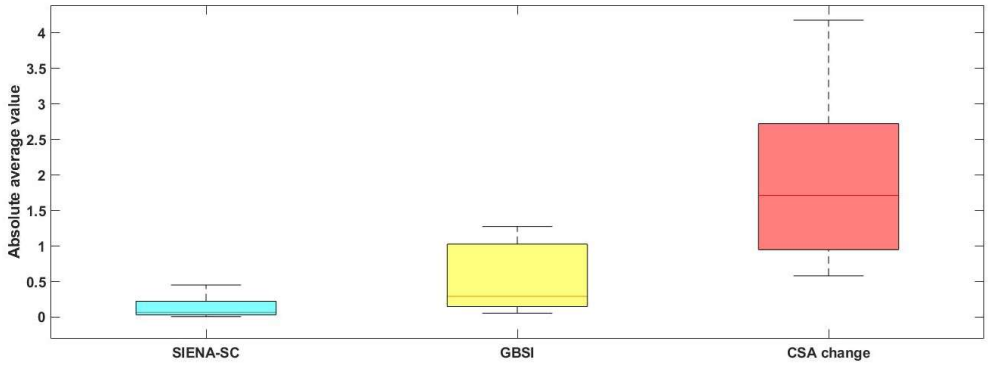

Figure 22: Boxplot showing the comparison of the measurements using SIENA-SC, GBSI and CSA change. The line inside the boxes indicates the median value. Results are shown in absolute values

4.2.2 Comparison between methods using Healthy Controls

On the HCs dataset, the annualized PCVC showed no degree of atrophy using all the three methods (SIENA-SC: -0.05% ± 0.45 ; GBSI: -0.08% ± 1.6; CSA: 0.005% ± 3.1).

T-test analysis did not show any difference in the measurements obtained with the three methods (SIENA-SC vs GBSI: p=0.85 ; SIENA-SC vs CSA change: p=0.78 ; GBSI vs CSA change: p=0.73).

4.2.2.1 SIENA-SC vs GBSI

SIENA-SC correlation with GBSI: r=0.48, p<0.05, mean absolute difference= -0.02%. The least-squares fit between SIENA-SC and GBSI is estimated at y=1.42x (R^2=0.16). See Figure 23 for a direct SIENA-SC vs. GBSI plot and a Bland Altman of the same data. The strong asymmetry in both the plot is driven by the differences in standard deviation between the two methods.

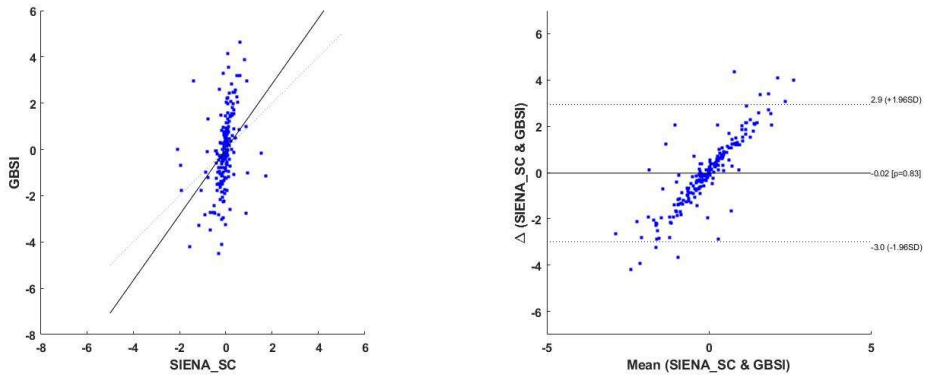

Figure 23: Scatter plot (on the left) showing PCVC evaluation from SIENA-SC (x) and GBSI (y). The dotted line shows ideal agreement of x=y. The continuous line shows the least-squares fit between SIENA-SC and GBSI. Bland Altman plot (on the right) showing the difference between SIENA-SC and GBSI

4.2.2.2 SIENA-SC vs CSA change

Correlation between SIENA-SC and CSA change measurements: r=0.29, p<0.05, mean absolute difference=0.06%. The least-squares fit between SIENA-SC and CSA change is estimated at y=2.02x + 0.12 (R^2=0.09). See Figure 24 for a direct SIENA-SC vs. CSA plot and a Bland Altman of the same data. The strong asymmetry in both the plot is driven by the differences in standard deviation between the two methods.

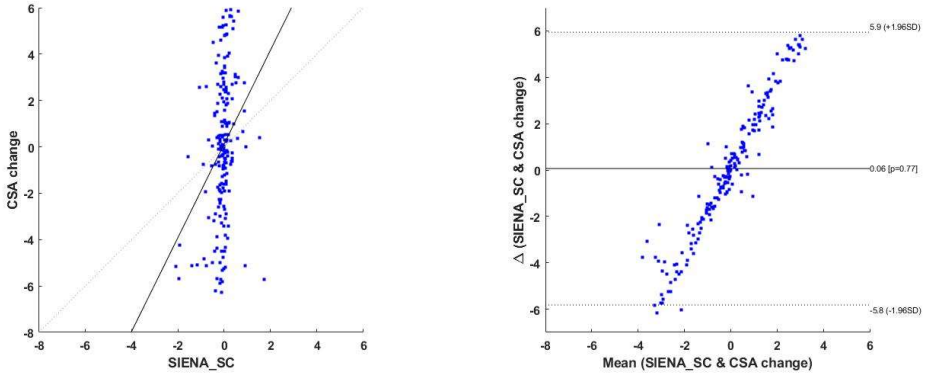

Figure 24: Scatter plot (on the left) showing PCVC evaluation from SIENA-SC (x) and CSA change (y). The dotted line shows ideal agreement of x=y. The continuous line shows the least-squares fit between SIENA-SC and CSA change. Bland Altman plot (on the right) showing the difference between SIENA-SC and CSA change.

4.2.2.3 GBSI vs CSA change

Correlation between GBSI and CSA change measurements: r=0.33, p<0.05, mean absolute difference= 0.09%. The least-squares fit between GBSI and CSA change is estimated at y=0.63x-0.06 (R^2=0.11). See Figure 25 for a direct GBSI vs. CSA change plot and a Bland Altman of the same data.

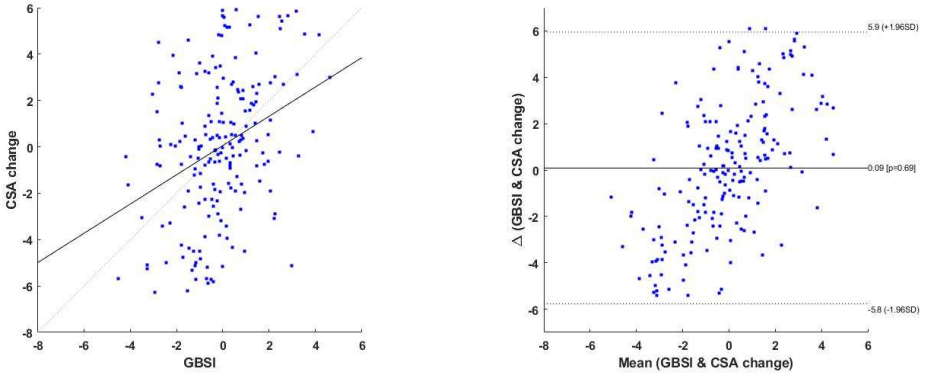

Figure 25: Scatter plot (on the left) showing PCVC evaluation from GBSI (x) and CSA change (y). The dotted line shows ideal agreement of x=y. The continuous line shows the least-squares fit between GBSI and CSA change. Bland Altman plot (on the right) showing the difference between SIENA-SC and CSA change.

4.3 Main findings

SIENA-SC showed a consistent higher robustness than GBSI and the CSA change when PCVC from scan rescan were assessed, while no differences were found between the three methods in the longitudinal dataset of HC. This is expected, due to the small biological variation of SC volume in HC. However, compared to GBSI and CSA change, SIENA-SC demonstrated a smaller dispersion of the data, as estimated by the standard error.

The higher robustness of SIENA-SC and GBSI, when compared with CSA on a scan-rescan dataset, can be explained by a better ability of registration-based methods to account for partial volume effects [192]. Such effects can cause segmentation errors and variability when calculating CSA. Indeed, conventional segmentation-based methods rely on numerical differences between areas obtained from hard segmentation at each time-point, which can lead to indirect estimates of atrophy and greater variability, especially when using scans with different intensity scales, different voxel sizes or other confounding effects like subject's repositioning, cord curvature or noise. The similar approach between SIENA-SC and GBSI can also explain the moderate correlation between the two methods, correlation that becomes weaker when they are compared with CSA (SIENA-SC: R=0.29, GBSI: R=0.33). Thus, our analysis confirmed the already known bigger reliability of registration-based methods compared with the segmentation-based ones [53].

Although sharing some of the pre-processing steps, the higher robustness and sensitivity shown by SIENA-SC compared with GBSI could rely on the different approaches used to derive changes in atrophy from local intensities variations. SIENA-SC reduces the impact of local random fluctuations in voxel intensities by comparing the profiles of the intensity derivatives,

and not directly assessing the differences in voxel intensities. On the other hand, GBSI reduces the global differences in two SC images through a prior intensity normalization and then directly compares the voxel intensities. This approach might be influenced by local fluctuations in voxel intensities, not fully recovered after the global intensity normalization and leads to assume that SIENA-SC could be less biased by sources of variability in MRI signal. In other words, GBSI approximate the brain volume change by measuring the intensity difference while SIENA measure the intensity profile distance between each corresponding pair of edge voxels of the rigidly registered baseline and repeat images. Indeed, both these two techniques significantly reduce the variance from segmentation errors by assessing the changes directly using intensity information.

5 Experiment 2: Sensitivity and sample size

5.1 Population

The second experiment aims to study the sensitivity of SIENA-SC in order to distinguish the physiological and pathological rate of atrophy.

5.1.1 Multiple Sclerosis subjects

We add a dataset of MS subject to the HC dataset used in the experiment 1. Population of the experiment 2 is summarized in Table 2.

MS data: 65 subjects acquired at two Italian sites: 10 subjects from Meyer Hospital in Florence (mean age: 40 ± 12,9 years; follow-up: 1,2 ± 0,4) and 55 subjects from University Hospital in Verona (mean age: 39 ± 11,3 years; follow-up: 1,4 ± 0,7).

All subjects had two brain 3D T1-w images acquired using a 3T MRI scanner, sagittally oriented and with 1 mm isotropic voxel. Details of the MRI acquisition are in Table 3.

	Number (Female)	Mean (SD) Age, years	Mean (SD) Follow-up
HC dataset	190 (99)	74 ± 5.7	1.2 ± 0.2
MS dataset	Center 1: 10 (7) Center 2: 55 (45)	40 ± 12.9	Center 1: 1.2 ± 0.4 Center 2: 1.4 ± 0.7

*Table 2: Population demographics. Center 1: Florence. Center 2: Verona. *Scan-rescan MRIs were performed on the same day*

Site	Field Strength	Manufacturer	Scanner Model	Echo Time	Repetition Time	Flip Angle	Pixel Bandwidth	Slice Thickness	Spacing Between slices
Florence	3T	Philips	Achieva	0,004s	0,01s	8	175	1	1
Verona	3T	Philips	Achieva	0,004s	0,008s	8	191	1	1
Verona	3T	Philips	Ingenia	0,004s	0,008s	8	191	1	1

Table 3: Scanner acquisition details for Florence and Verona Sites

5.2 Statistical analysis

The statistical analysis was performed using MATLAB Release R2020a. Significance level was set to $P < 0.05$.

A linear regression model has been used to measure the sensibility of the methods in discriminating HC subjects from MS patients. SIENA-SC, GBSI and CSA change were the dependent variable, group (HC or MS), age and sex were the covariates. Results are shown as the coefficient of PCVC change in MS patients, 95% confidence interval and p-values.

To evaluate the precision of each method, we computed the sample size for an hypothetical trial with 80% power at the 5% significance level and looking for 50%, 70% and 90% treatment effects.

As for the experiment one, PCVC obtained from CSA measurements was calculated as the CSA difference between two consecutive time-points CSA, divided by the first time-point and multiplied by 100.

5.3 Results

5.3.1 Comparison between HCs and MS

The linear regression model adjusted by group (HC and MS), age and sex, showed a different rate of atrophy in MS patients compared to the HC using the three methods: SIENA-SC (Coeff: -0.54, 95%CI=[-0.87, -0.21], p<0.001); GBSI (Coeff: -0.84 ; 95%CI=[-1.81, 0.12], p=0.08); CSA change (Coeff: -1.92 ; 95%CI=[-3.82, -0.016], p=0.048). Raw values of the results are illustrated in Table 4 and Figure 26.

	HC	**MS**	**p-value**
Annualized SIENA-SC [SE]	-0.05 ± 0.45 [0.03]	-0.6 ± 0.77 [0.09]	<0.001
Annualized GBSI [SE]	-0.08 ± 1.6 [0.12]	-1.14 ± 1.56 [0.19]	0.08
Annualized CSA change [SE]	0.005 ± 3.1 [0.22]	-1.52 ± 3.44 [0.42]	0.048

Table 4: Table showing the raw mean values, standard deviation, and standard error of PCVC obtained with the three methods. SE: Standard Error.

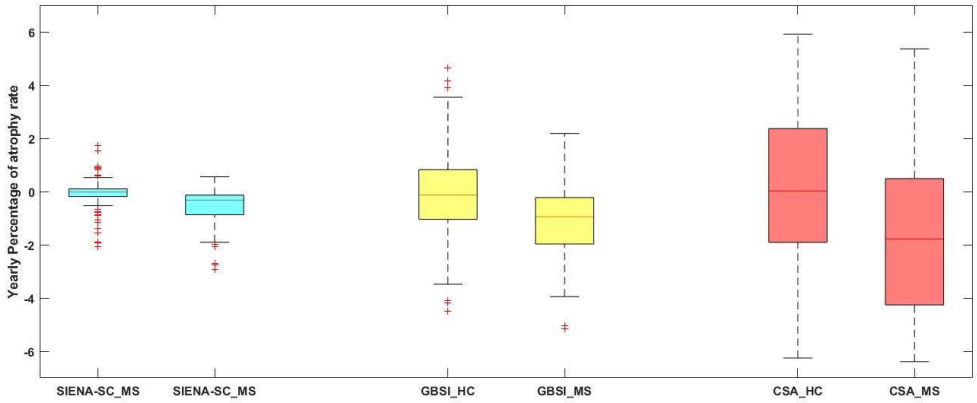

Figure 26: Boxplot illustrates the comparison of the annualized percentage cord area changes obtained using SIENA-SC, GBSI and CSA change between healthy control and multiple sclerosis subjects.

5.3.2 Sample size

Considering the sample size estimation per arm for a clinical trial where SC atrophy could be an outcome to measure the response to treatment, SIENA-SC showed the lowest number of MS patients needed to observe an effect over this hypothetical treatment (Table 5 and Figure 27).

Software	Effect size %	Sample Size [CI] (MS Subjects)
SIENA-SC	50	54 [39 to 95]
	70	146 [107 to 217]
	90	1290 [933 to 1986]
GBSI	50	62 [36 to 135]
	70	167 [86 to 478]
	90	1483 [714 to 4287]
CSA	50	171 [59 to 5628]
	70	472 [157 to 2700]
	90	4224 [1859 to 8991]

Table 5: Estimated sample size per arm with all the three methods (Power= 80%, 5% Significance level).

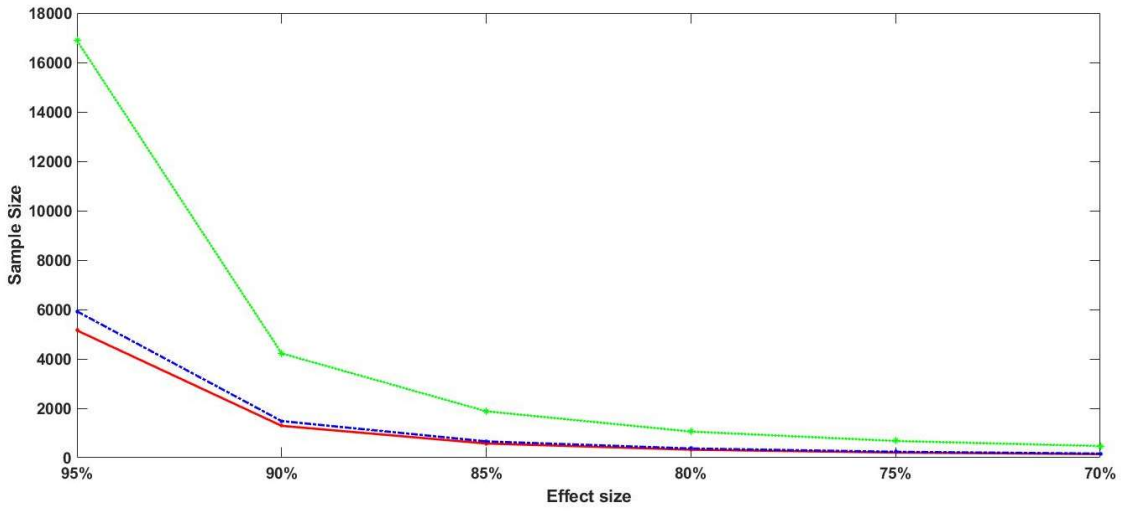

Figure 27: Plot showing the sample size power for different effect size for each method (SIENA-SC: continuous red line ; GBSI: blue dash-dot line ; CSA: green dotted line)

5.4 Main findings

There have been few clinical trials and observational studies in MS that used SC atrophy as an outcome measure, because of the large sample size required when using the available CSA method [9,135,193].

To provide evidence that SIENA-SC could be applied to neurological diseases, in this experiment we applied SIENA-SC, GBSI and the CSA change on a dataset of MS patients from two centers. As explained in chapter 1.4, SC atrophy is a well-known feature in MS since the early stages and monitoring cervical SC atrophy may be clinically relevant, due to its correlation with increased disability.

In our population, SIENA-SC was able to significantly distinguish between MS and HC ($p<0.001$), compared with GBSI ($p=0.08$). Although CSA changes narrowly obtained significance (0.048), both CSA and GBSI showed higher standard error than that from SIENA-SC. These results imply that SIENA-SC measurements are more precise, thereby holding promise for future MS research on SC imaging.

SIENA-SC yielded increased statistical power to detect 50-70-90% treatment effects than those provided by GBSI and CSA change, anyway, both the registration-based methods outperformed the results obtained by the atrophy changes measured with CSA. Specifically, SIENA-SC provided a three-fold smaller sample size than that obtained with CSA, while only slightly smaller than the one estimated by GBSI. Overall, the sample size estimates for SC atrophy measurements with SIENA-SC are of the same order of magnitude as those for brain atrophy obtained with registration-based methods [15,194,195].

This preliminary analysis is promising and seems to indicate SC atrophy as evaluated by SIENA-SC a suitable endpoint in clinical trials and in observational datasets.

6 General discussion

This study shows the feasibility of SIENA-SC, a fully automated, easy-to-use, tool to calculate the PCVC using brain MRI acquisitions, thus translating the behavior of the original SIENA method from brain to SC. Assessing SC atrophy from brain scans, the scan time for MRI and the associated cost could be significantly reduced, also relieving patients' burden. Moreover, SIENA-SC allows to obtain PCVC without extensive computer engineering experience and reduce inter-operator variability. To obtain this, a novel optimized pre-processing procedure, constituted by integrating and optimizing some previously developed routines, was ideated and tested.

SIENA-SC starts with a pre-processing based on an artificial-intelligence freely available tool [62]. This step eliminates the initial operator intervention necessary for the identification of the initial mask of the spine. This approach is valid by itself, making fully automated also the two methods, GBSI and CSA, compared with SIENA-SC. Indeed the same generated cord masks have been used for the atrophy assessment in all the three methods. In order to reproduce the SIENA methodology for the analysis of SC atrophy, we optimized a registration procedure between two longitudinally acquired images. This step was implemented using jointly, for each timepoint, images and masks of the dilated cord up to the vertebra, to provide the registration tool a non-moving reference. Finally, SIENA-SC derives the percentage change in atrophy through an indirect approximation of the local edge displacement, using the differences between the derivatives of the intensities between the 2 images and a calibration factor that depends on the size of the SC and serves to reduce the variability introduced by the intrinsic differences between the two images.

6.1 Limitation

This study is a proof-of-concept of the use of SIENA-SC. We mainly focused on the creation of the method and the initial validation of its robustness and sensitivity. These results should be confirmed on larger datasets of brain MRI images with a visible cervical cord and tested in different neurological diseases.

6.2 Future directions

The easy use of SIENA-SC could allow the evaluation of physiological changes in large data sets of HCs, defining normative values as already demonstrated for the brain atrophy using the SIENA method [196]. Furthermore, new studies using data sets of neurological patients supplied by clinical information should better explore the method's sensitivity in identifying pathological deviations from normality. Finally, SC atrophy could be combined with other clinical and brain MRI outcome measures to further improve the surveillance of the clinical course in neurological diseases [139,197,198]. Indeed, combined endpoints have become increasingly common, and the inclusion of SC atrophy could further improve statistical power and clinical correlates.

6.3 Conclusion

In this study, we presented SIENA-SC, a new method to assess SC atrophy longitudinally.

The software is fully automated, easy to use and has been specifically designed, but not limited, to work on routinely acquired brain MRI sequences, such as MPRAGE[6].

SIENA-SC offers reliable, sensitive and consistent quantitative measurements of longitudinal SC volume change.

This study provides evidence that SIENA-SC can be considered as a precise and reliable tool for calculating MS-related SC atrophy in clinical trials and in observational datasets or in other neurological disease where SC plays a determinant role.

Bibliography

[1] G. and J.K.M. Paxinos, The human nervous system, in: 2004: p. 11.

[2] D.W. Cadotte, A. Cadotte, J. Cohen-Adad, D. Fleet, M. Livne, J.R. Wilson, D. Mikulis, N. Nugaeva, M.G. Fehlings, *Characterizing the Location of Spinal and Vertebral Levels in the Human Cervical Spinal Cord*, American Journal of Neuroradiology. 36 (2015) 803–810. https://doi.org/10.3174/ajnr.A4192.

[3] M. Zhou, N. Goto, C. Zhang, W. Tang, *Aging process of the human lumbar spinal cord: A morphometric analysis*, Neuropathology. 16 (1996) 106–111. https://doi.org/10.1111/j.1440-1789.1996.tb00164.x.

[4] F. Kato, Y. Yukawa, K. Suda, M. Yamagata, T. Ueta, *Normal morphology, age-related changes and abnormal findings of the cervical spine. Part II: magnetic resonance imaging of over 1,200 asymptomatic subjects*, European Spine Journal. 21 (2012) 1499–1507. https://doi.org/10.1007/s00586-012-2176-4.

[5] A. Saliani, B. Perraud, T. Duval, N. Stikov, S. Rossignol, J. Cohen-Adad, *Axon and Myelin Morphology in Animal and Human Spinal Cord*, Front Neuroanat. 11 (2017). https://doi.org/10.3389/fnana.2017.00129.

[6] J. Sastre-Garriga, D. Pareto, M. Battaglini, M.A. Rocca, O. Ciccarelli, C. Enzinger, J. Wuerfel, M.P. Sormani, F. Barkhof, T.A. Yousry, N. De Stefano, M. Tintoré, M. Filippi, C. Gasperini, L. Kappos, J. Río, J. Frederiksen, J. Palace, H. Vrenken, X. Montalban, À. Rovira, *MAGNIMS consensus recommendations on the use of brain and spinal cord atrophy measures in clinical practice*, Nat Rev Neurol. 16 (2020) 171–182. https://doi.org/10.1038/s41582-020-0314-x.

[7] S.M. Smith, Y. Zhang, M. Jenkinson, J. Chen, P.M. Matthews, A. Federico, N. De Stefano, *Accurate, Robust, and Automated Longitudinal and Cross-Sectional Brain Change Analysis*, Neuroimage. 17 (2002) 479–489. https://doi.org/10.1006/nimg.2002.1040.

[8] V. Fonov, A. Evans, R. McKinstry, C. Almli, D. Collins, *Unbiased nonlinear average age-appropriate brain templates from birth to adulthood*, Neuroimage. 47 (2009) S102. https://doi.org/10.1016/S1053-8119(09)70884-5.

[9] C. Tur, M. Moccia, F. Barkhof, J. Chataway, J. Sastre-Garriga, A.J. Thompson, O. Ciccarelli, *Assessing treatment outcomes in multiple sclerosis trials and in the clinical setting*, Nat Rev Neurol. 14 (2018) 75–93. https://doi.org/10.1038/nrneurol.2017.171.

[10] X. Montalban, S.L. Hauser, L. Kappos, D.L. Arnold, A. Bar-Or, G. Comi, J. de Seze, G. Giovannoni, H.-P. Hartung, B. Hemmer, F. Lublin, K.W. Rammohan, K. Selmaj, A. Traboulsee, A. Sauter, D. Masterman, P. Fontoura, S. Belachew, H. Garren, N. Mairon, P. Chin, J.S. Wolinsky, *Ocrelizumab versus Placebo in Primary Progressive Multiple Sclerosis*, New England Journal of Medicine. 376 (2017) 209–220. https://doi.org/10.1056/NEJMoa1606468.

[11] L. Kappos, A. Bar-Or, B.A.C. Cree, R.J. Fox, G. Giovannoni, R. Gold, P. Vermersch, D.L. Arnold, S. Arnould, T. Scherz, C. Wolf, E. Wallström, F. Dahlke, A. Achiron, L. Achtnichts, K. Agan, G. Akman-Demir, A.B. Allen, J.P. Antel, A.R. Antiguedad, M. Apperson, A.M. Applebee, G.I. Ayuso, M. Baba, O. Bajenaru, R. Balasa, B.P. Balci, M. Barnett, A. Bass, V.U. Becker, M. Bejinariu, F.T. Bergh, A. Bergmann, E. Bernitsas, A. Berthele, V. Bhan, F. Bischof, R.J. Bjork, G. Blevins, M. Boehringer, T. Boerner, R. Bonek, J.D. Bowen, A. Bowling, A.N. Boyko, C. Boz, V. Bracknies, S. Braune, V. Brescia Morra, B. Brochet, W. Brola, P.K. Brownstone, M. Brozman, D. Brunet, I. Buraga, M. Burnett, M. Buttmann, H. Butzkueven, J. Cahill, J.C. Calkwood, W. Camu, M. Cascione, G. Castelnovo, D. Centonze, J. Cerqueira, A. Chan, A. Cimprichova, S. Cohan, G. Comi, J. Conway, J.A. Cooper, J. Corboy, J. Correale, B. Costell, D.A. Cottrell, P.K. Coyle, M. Craner, L. Cui, L. Cunha, A. Czlonkowska, A.M. da Silva, J. de Sa, J. de Seze, M. Debouverie, J. Debruyne, D. Decoo, G. Defer, T. Derfuss, N.H. Deri, B. Dihenia, P. Dioszeghy, V. Donath, B. Dubois, M. Duddy, P. Duquette, G. Edan, H. Efendi, S. Elias, P.J. Emrich, B.C. Estruch, E.P. Evdoshenko, J. Faiss, A.S. Fedyanin, W. Feneberg, J. Fermont, O.F. Fernandez, F.C. Ferrer, K. Fink, H. Ford, C. Ford, A. Francia, M. Freedman, B. Frishberg, S. Galgani, G.P. Garmany, K. Gehring, J. Gitt, C. Gobbi, L.P. Goldstick, R.A. Gonzalez, F. Grandmaison, N. Grigoriadis, O. Grigorova,

L.M.E. Grimaldi, J. Gross, K. Gross-Paju, M. Gudesblatt, D. Guillaume, J. Haas, V. Hancinova, A. Hancu, O. Hardiman, A. Harmjanz, F.R. Heidenreich, G.J.D. Hengstman, J. Herbert, M. Herring, S. Hodgkinson, O.M. Hoffmann, W.E. Hofmann, W.D. Honeycutt, L.H. Hua, D. Huang, Y. Huang, D. Huang, R. Hupperts, P. Imre, A.K. Jacobs, G. Jakab, E. Jasinska, K. Kaida, J. Kalnina, A. Kaprelyan, G. Karelis, D. Karussis, A. Katz, F.A. Khabirov, B. Khatri, T. Kimura, I. Kister, R. Kizlaitiene, E. Klimova, J. Koehler, A. Komatineni, A. Kornhuber, K. Kovacs, A. Koves, W. Kozubski, G. Krastev, L.B. Krupp, E. Kurca, C. Lassek, G. Laureys, L. Lee, E. Lensch, F. Leutmezer, H. Li, R.A. Linker, M. Linnebank, P. Liskova, C. Llanera, J. Lu, A. Lutterotti, J. Lycke, R. Macdonell, M. Maciejowski, M. Maeurer, R. V Magzhanov, E.-M. Maida, L. Malciene, Y. Mao-Draayer, G.A. Marfia, C. Markowitz, V. Mastorodimos, K. Matyas, J. Meca-Lallana, J.A.G. Merino, I.G. Mihetiu, I. Milanov, A.E. Miller, A. Millers, M. Mirabella, M. Mizuno, X. Montalban, L. Montoya, M. Mori, S. Mueller, J. Nakahara, Y. Nakatsuji, S. Newsome, R. Nicholas, A.S. Nielsen, E. Nikfekr, U. Nocentini, C. Nohara, K. Nomura, M.M. Odinak, T. Olsson, B.W. van Oosten, C. Oreja-Guevara, P. Oschmann, J. Overell, A. Pachner, G. Panczel, M. Pandolfo, C. Papeix, L. Patrucco, J. Pelletier, R. Piedrabuena, M. Pless, U. Polzer, K. Pozsegovits, D. Rastenyte, S. Rauer, G. Reifschneider, R. Rey, S.A. Rizvi, D. Robertson, J.M. Rodriguez, D. Rog, H. Roshanisefat, V. Rowe, C. Rozsa, S. Rubin, S. Rusek, F. Saccà, T. Saida, A.V. Salgado, V.E.F. Sanchez, K. Sanders, M. Satori, D. V Sazonov, E.A. Scarpini, E. Schlegel, M. Schluep, S. Schmidt, E. Scholz, H.M. Schrijver, M. Schwab, R. Schwartz, J. Scott, K. Selmaj, S. Shafer, B. Sharrack, I.A. Shchukin, Y. Shimizu, P. Shotekov, A. Siever, K.-O. Sigel, S. Silliman, M. Simo, M. Simu, V. Sinay, A.E. Siquier, A. Siva, O. Skoda, A. Solomon, M. Stangel, D. Stefoski, B. Steingo, I.D. Stolyarov, P. Stourac, K. Strassburger-Krogias, E. Strauss, O. Stuve, I. Tarnev, A. Tavernarakis, C.R. Tello, M. Terzi, V. Ticha, M. Ticmeanu, K. Tiel-Wilck, T. Toomsoo, N. Tubridy, M.J. Tullman, H. Tumani, P. Turcani, B. Turner, A. Uccelli, F.J.O. Urtaza, M. Vachova, A. Valikovics, S. Walter, B. Van Wijmeersch, L. Vanopdenbosch, J.R. Weber, S. Weiss, R. Weissert, P. Vermersch, T. West, H. Wiendl, S. Wiertlewski, B. Wildemann, B. Willekens, L.H. Visser, G. Vorobeychik, X. Xu, T. Yamamura, Y.N. Yang, S.M. Yelamos, M. Yeung, A. Zacharias, M. Zelkowitz, U. Zettl, M. Zhang, H. Zhou, U. Zieman, T. Ziemssen, *Siponimod versus placebo in secondary progressive multiple*

sclerosis (EXPAND): a double-blind, randomised, phase 3 study, The Lancet. 391 (2018) 1263–1273. https://doi.org/10.1016/S0140-6736(18)30475-6.

[12] P.A. Freeborough, N.C. Fox, *The boundary shift integral: an accurate and robust measure of cerebral volume changes from registered repeat MRI*, IEEE Trans Med Imaging. 16 (1997) 623–629. https://doi.org/10.1109/42.640753.

[13] K.K. Leung, M.J. Clarkson, J.W. Bartlett, S. Clegg, C.R. Jack, M.W. Weiner, N.C. Fox, S. Ourselin, *Robust atrophy rate measurement in Alzheimer's disease using multi-site serial MRI: Tissue-specific intensity normalization and parameter selection*, Neuroimage. 50 (2010) 516–523. https://doi.org/10.1016/j.neuroimage.2009.12.059.

[14] F. Prados, M.J. Cardoso, K.K. Leung, D.M. Cash, M. Modat, N.C. Fox, C.A.M. Wheeler-Kingshott, S. Ourselin, *Measuring brain atrophy with a generalized formulation of the boundary shift integral*, Neurobiol Aging. 36 (2015) S81–S90. https://doi.org/10.1016/j.neurobiolaging.2014.04.035.

[15] D.R. Altmann, B. Jasperse, F. Barkhof, K. Beckmann, M. Filippi, L.D. Kappos, P. Molyneux, C.H. Polman, C. Pozzilli, A.J. Thompson, K. Wagner, T.A. Yousry, D.H. Miller, *Sample sizes for brain atrophy outcomes in trials for secondary progressive multiple sclerosis*, Neurology. 72 (2009) 595–601. https://doi.org/10.1212/01.wnl.0000335765.55346.fc.

[16] S.M. Smith, N. De Stefano, M. Jenkinson, P.M. Matthews, *Normalized Accurate Measurement of Longitudinal Brain Change*, J Comput Assist Tomogr. 25 (2001) 466–475. https://doi.org/10.1097/00004728-200105000-00022.

[17] S.M. Smith, *Fast robust automated brain extraction*, Hum Brain Mapp. 17 (2002) 143–155. https://doi.org/10.1002/hbm.10062.

[18] P.A. Freeborough, R.P. Woods, N.C. Fox, *Accurate Registration of Serial 3D MR Brain Images and Its Application to Visualizing Change in Neurodegenerative Disorders*, J Comput Assist Tomogr. 20 (1996) 1012–1022. https://doi.org/10.1097/00004728-199611000-00030.

[19] M. Jenkinson, S. Smith, *A global optimisation method for robust affine registration of brain images*, Med Image Anal. 5 (2001) 143–156. https://doi.org/10.1016/S1361-8415(01)00036-6.

[20] J. V. Hajnal, N. Saeed, E.J. Soar, A. Oatridge, I.R. Young, G.M. Bydder, *A registration and interpolation procedure for subvoxel matching of serially acquired MR images*, J Comput Assist Tomogr. 19 (1995) 289–296. https://doi.org/10.1097/00004728-199503000-00022.

[21] J. V. Hajnal, N. Saeed, A. Oatridge, E.J. Williams, I.R. Young, G.M. Bydder, *Detection of subtle brain changes using subvoxel registration and subtraction of serial MR images*, J Comput Assist Tomogr. 19 (1995) 677–691. https://doi.org/10.1097/00004728-199509000-00001.

[22] L. Lemicux, U.C. Wicshmann, N.F. Moran, D.R. Fish, S.D. Shorvon, *The detection and significance of subtle changes in mixed-signal brain lesions by serial MRI scan matching and spatial normalization*, Med Image Anal. 2 (1998) 227–242. https://doi.org/10.1016/S1361-8415(98)80021-2.

[23] Y. Zhang, M. Brady, S. Smith, *Segmentation of brain MR images through a hidden Markov random field model and the expectation-maximization algorithm*, IEEE Trans Med Imaging. 20 (2001) 45–57. https://doi.org/10.1109/42.906424.

[24] R.P. Woods, S.T. Grafton, C.J. Holmes, S.R. Cherry, J.C. Mazziotta, *Automated Image Registration: I. General Methods and Intrasubject, Intramodality Validation*, J Comput Assist Tomogr. 22 (1998) 139–152. https://doi.org/10.1097/00004728-199801000-00027.

[25] E.B. Lewis, N.C. Fox, *Correction of differential intensity inhomogeneity in longitudinal MR images*, Neuroimage. 23 (2004) 75–83. https://doi.org/10.1016/j.neuroimage.2004.04.030.

[26] P.W. Stroman, R.L. Bosma, Spinal Cord Imaging, in: Neurological Aspects of Spinal Cord Injury, Springer International Publishing, Cham, 2017: pp. 237–257. https://doi.org/10.1007/978-3-319-46293-6_10.

[27] C.A. Wheeler-Kingshott, P.W. Stroman, J.M. Schwab, M. Bacon, R. Bosma, J. Brooks, D.W. Cadotte, T. Carlstedt, O. Ciccarelli, J. Cohen-Adad, A. Curt, N. Evangelou, M.G. Fehlings, M. Filippi, B.J. Kelley, S. Kollias, A. Mackay, C.A. Porro, S. Smith, S.M. Strittmatter, P. Summers, A.J. Thompson, I. Tracey, *The current state-of-the-art of spinal cord imaging: Applications*, Neuroimage. 84 (2014) 1082–1093. https://doi.org/10.1016/j.neuroimage.2013.07.014.

[28] P.W. Stroman, C. Wheeler-Kingshott, M. Bacon, J.M. Schwab, R. Bosma, J. Brooks, D. Cadotte, T. Carlstedt, O. Ciccarelli, J. Cohen-Adad, A. Curt, N. Evangelou, M.G. Fehlings, M. Filippi, B.J. Kelley, S. Kollias, A. Mackay, C.A. Porro, S. Smith, S.M. Strittmatter, P. Summers, I. Tracey, *The current state-of-the-art of spinal cord imaging: Methods*, Neuroimage. 84 (2014) 1070–1081. https://doi.org/10.1016/j.neuroimage.2013.04.124.

[29] G. Nair, M. Absinta, D.S. Reich, *Optimized T1-MPRAGE Sequence for Better Visualization of Spinal Cord Multiple Sclerosis Lesions at 3T*, American Journal of Neuroradiology. 34 (2013) 2215–2222. https://doi.org/10.3174/ajnr.A3637.

[30] H.H. Donaldson, D.J. Davis, *A description of charts showing the areas of the cross sections of the human spinal cord at the level of each spinal nerve*, Journal of Comparative Neurology. 13 (2004) 19–40. https://doi.org/10.1002/cne.910130104.

[31] H.C. Elliott, *Cross-sectional diameters and areas of the human spinal cord*, Anat Rec. 93 (2005) 287–293. https://doi.org/10.1002/ar.1090930306.

[32] H.-Y. Ko, J.H. Park, Y.B. Shin, S.Y. Baek, *Gross quantitative measurements of spinal cord segments in human*, Spinal Cord. 42 (2004) 35–40. https://doi.org/10.1038/sj.sc.3101538.

[33] A. Frostell, R. Hakim, E.P. Thelin, P. Mattsson, M. Svensson, *A Review of the Segmental Diameter of the Healthy Human Spinal Cord*, Front Neurol. 7 (2016). https://doi.org/10.3389/fneur.2016.00238.

[34] R.A. Bhadelia, A.R. Bogdan, R.F. Kaplan, S.M. Wolpert, *Cerebrospinal fluid pulsation amplitude and its quantitative relationship to cerebral blood flow pulsations: a phase-*

contrast MR flow imaging study, Neuroradiology. 39 (1997) 258–264. https://doi.org/10.1007/s002340050404.

[35] C.R. Figley, P.W. Stroman, *Investigation of human cervical and upper thoracic spinal cord motion: Implications for imaging spinal cord structure and function*, Magn Reson Med. 58 (2007) 185–189. https://doi.org/10.1002/mrm.21260.

[36] M. Piché, J. Cohen-Adad, M.K. Nejad, V. Perlbarg, G. Xie, G. Beaudoin, H. Benali, P. Rainville, *Characterization of cardiac-related noise in fMRI of the cervical spinal cord*, Magn Reson Imaging. 27 (2009) 300–310. https://doi.org/10.1016/j.mri.2008.07.019.

[37] N.A. Losseff, S.L. Webb, J.I. O'Riordan, R. Page, L. Wang, G.J. Barker, P.S. Tofts, W.I. McDonald, D.H. Miller, A.J. Thompson, *Spinal cord atrophy and disability in multiple sclerosis*, Brain. 119 (1996) 701–708. https://doi.org/10.1093/brain/119.3.701.

[38] B. De Leener, M. Taso, J. Cohen-Adad, V. Callot, *Segmentation of the human spinal cord*, Magnetic Resonance Materials in Physics, Biology and Medicine. 29 (2016) 125–153. https://doi.org/10.1007/s10334-015-0507-2.

[39] O. Coulon, S.J. Hickman, G.J. Parker, G.J. Barker, D.H. Miller, S.R. Arridge, *Quantification of spinal cord atrophy from magnetic resonance images via a B-spline active surface model*, Magn Reson Med. 47 (2002) 1176–1185. https://doi.org/10.1002/mrm.10162.

[40] S.J. Hickman, A. Hadjiprocopis, O. Coulon, D.H. Miller, G.J. Barker, *Cervical spinal cord MTR histogram analysis in multiple sclerosis using a 3D acquisition and a B-spline active surface segmentation technique*, Magn Reson Imaging. 22 (2004) 891–895. https://doi.org/10.1016/j.mri.2004.01.056.

[41] M.A. Horsfield, S. Sala, M. Neema, M. Absinta, A. Bakshi, M.P. Sormani, M.A. Rocca, R. Bakshi, M. Filippi, *Rapid semi-automatic segmentation of the spinal cord from magnetic resonance images: Application in multiple sclerosis*, Neuroimage. 50 (2010) 446–455. https://doi.org/10.1016/j.neuroimage.2009.12.121.

[42] R. Van Uitert, I. Bitter, J.A. Butman, Semi-automatic segmentation and quantification of 3D spinal cord data, in: A. Manduca, A.A. Amini (Eds.), 2006: p. 61430S. https://doi.org/10.1117/12.653266.

[43] J. Carbonell-Caballero, J. V. Manjón, L. Martí-Bonmatí, J.R. Olalla, B. Casanova, M. de la Iglesia-Vayá, F. Coret, M. Robles, *Accurate quantification methods to evaluate cervical cord atrophy in multiple sclerosis patients*, Magnetic Resonance Materials in Physics, Biology and Medicine. 19 (2006) 237–246. https://doi.org/10.1007/s10334-006-0052-0.

[44] Jaehan Koh, Taehyong Kim, V. Chaudhary, G. Dhillon, Automatic segmentation of the spinal cord and the dural sac in lumbar MR images using gradient vector flow field, in: 2010 Annual International Conference of the IEEE Engineering in Medicine and Biology, IEEE, 2010: pp. 3117–3120. https://doi.org/10.1109/IEMBS.2010.5626097.

[45] M. Chen, A. Carass, J. Oh, G. Nair, D.L. Pham, D.S. Reich, J.L. Prince, *Automatic magnetic resonance spinal cord segmentation with topology constraints for variable fields of view*, Neuroimage. 83 (2013) 1051–1062. https://doi.org/10.1016/j.neuroimage.2013.07.060.

[46] V.S. Fonov, A. Le Troter, M. Taso, B. De Leener, G. Lévêque, M. Benhamou, M. Sdika, H. Benali, P.-F. Pradat, D.L. Collins, V. Callot, J. Cohen-Adad, *Framework for integrated MRI average of the spinal cord white and gray matter: The MNI–Poly–AMU template*, Neuroimage. 102 (2014) 817–827. https://doi.org/10.1016/j.neuroimage.2014.08.057.

[47] M.C. Yiannakas, A.M. Mustafa, B. De Leener, H. Kearney, C. Tur, D.R. Altmann, F. De Angelis, D. Plantone, O. Ciccarelli, D.H. Miller, J. Cohen-Adad, C.A.M. Gandini Wheeler-Kingshott, *Fully automated segmentation of the cervical cord from T1-weighted MRI using PropSeg : Application to multiple sclerosis*, Neuroimage Clin. 10 (2016) 71–77. https://doi.org/10.1016/j.nicl.2015.11.001.

[48] D. Kidd, J.W. Thorpe, A.J. Thompson, B.E. Kendall, I.F. Moseley, D.G. MacManus, W.I. McDonald, D.H. Miller, *Spinal cord MRI using multi-array coils and fast spin echo: II.*

Findings in multiple sclerosis, Neurology. 43 (1993) 2632–2632. https://doi.org/10.1212/WNL.43.12.2632.

[49] X. Lin, C.R. Tench, N. Evangelou, T. Jaspan, C.S. Constantinescu, *Measurement of Spinal Cord Atrophy in Multiple Sclerosis*, Journal of Neuroimaging. 14 (2004) 20–26. https://doi.org/10.1177/1051228404266265.

[50] P. Valsasina, M.A. Rocca, M.A. Horsfield, M. Copetti, M. Filippi, *A longitudinal MRI study of cervical cord atrophy in multiple sclerosis*, J Neurol. 262 (2015) 1622–1628. https://doi.org/10.1007/s00415-015-7754-z.

[51] C. Lukas, D.L. Knol, M.H. Sombekke, B. Bellenberg, H.K. Hahn, V. Popescu, K. Weier, E.W. Radue, A. Gass, L. Kappos, Y. Naegelin, B.M.J. Uitdehaag, J.J.G. Geurts, F. Barkhof, H. Vrenken, *Cervical spinal cord volume loss is related to clinical disability progression in multiple sclerosis*, J Neurol Neurosurg Psychiatry. 86 (2015) 410–418. https://doi.org/10.1136/jnnp-2014-308021.

[52] C. Lukas, M.H. Sombekke, B. Bellenberg, H.K. Hahn, V. Popescu, K. Bendfeldt, E.W. Radue, A. Gass, S.J. Borgwardt, L. Kappos, Y. Naegelin, D.L. Knol, C.H. Polman, J.J.G. Geurts, F. Barkhof, H. Vrenken, *Relevance of Spinal Cord Abnormalities to Clinical Disability in Multiple Sclerosis: MR Imaging Findings in a Large Cohort of Patients*, Radiology. 269 (2013) 542–552. https://doi.org/10.1148/radiol.13122566.

[53] M. Moccia, F. Prados, M. Filippi, M.A. Rocca, P. Valsasina, W.J. Brownlee, C. Zecca, A. Gallo, A. Rovira, A. Gass, J. Palace, C. Lukas, H. Vrenken, S. Ourselin, C.A.M. Gandini Wheeler-Kingshott, O. Ciccarelli, F. Barkhof, *Longitudinal spinal cord atrophy in multiple sclerosis using the generalized boundary shift integral*, Ann Neurol. 86 (2019) 704–713. https://doi.org/10.1002/ana.25571.

[54] M. Moccia, S. Ruggieri, A. Ianniello, A. Toosy, C. Pozzilli, O. Ciccarelli, *Advances in spinal cord imaging in multiple sclerosis*, Ther Adv Neurol Disord. 12 (2019) 175628641984059. https://doi.org/10.1177/1756286419840593.

[55] Xinapse, *Cord Finder - Introduction.* , Http://Www.Xinapse.Com/Manual/. (2018). http://www.xinapse.com/Manual/ (accessed December 28, 2018).

[56] H. Kearney, M.C. Yiannakas, K. Abdel-Aziz, C.A.M. Wheeler-Kingshott, D.R. Altmann, O. Ciccarelli, D.H. Miller, *Improved MRI quantification of spinal cord atrophy in multiple sclerosis*, Journal of Magnetic Resonance Imaging. 39 (2014) 617–623. https://doi.org/10.1002/jmri.24194.

[57] B. De Leener, S. Lévy, S.M. Dupont, V.S. Fonov, N. Stikov, D. Louis Collins, V. Callot, J. Cohen-Adad, *SCT: Spinal Cord Toolbox, an open-source software for processing spinal cord MRI data*, Neuroimage. 145 (2017) 24–43. https://doi.org/10.1016/j.neuroimage.2016.10.009.

[58] SCT, *Studies using SCT*, (2023). https://spinalcordtoolbox.com/overview/studies.html (accessed June 29, 2023).

[59] B. De Leener, S. Kadoury, J. Cohen-Adad, *Robust, accurate and fast automatic segmentation of the spinal cord*, Neuroimage. 98 (2014) 528–536. https://doi.org/10.1016/j.neuroimage.2014.04.051.

[60] D.H. Ballard, *Generalizing the Hough transform to detect arbitrary shapes*, Pattern Recognit. 13 (1981) 111–122. https://doi.org/10.1016/0031-3203(81)90009-1.

[61] M.R. Kaus, V. Pekar, C. Lorenz, R. Truyen, S. Lobregt, J. Weese, *Automated 3-D PDM construction from segmented images using deformable models*, IEEE Trans Med Imaging. 22 (2003) 1005–1013. https://doi.org/10.1109/TMI.2003.815864.

[62] C. Gros, B. De Leener, A. Badji, J. Maranzano, D. Eden, S.M. Dupont, J. Talbott, R. Zhuoquiong, Y. Liu, T. Granberg, R. Ouellette, Y. Tachibana, M. Hori, K. Kamiya, L. Chougar, L. Stawiarz, J. Hillert, E. Bannier, A. Kerbrat, G. Edan, P. Labauge, V. Callot, J. Pelletier, B. Audoin, H. Rasoanandrianina, J.-C. Brisset, P. Valsasina, M.A. Rocca, M. Filippi, R. Bakshi, S. Tauhid, F. Prados, M. Yiannakas, H. Kearney, O. Ciccarelli, S. Smith, C.A. Treaba, C. Mainero, J. Lefeuvre, D.S. Reich, G. Nair, V. Auclair, D.G. McLaren, A.R. Martin, M.G. Fehlings, S. Vahdat, A. Khatibi, J. Doyon, T. Shepherd, E. Charlson, S. Narayanan, J. Cohen-Adad, *Automatic segmentation of the spinal cord and intramedullary multiple sclerosis lesions with convolutional neural networks*, Neuroimage. 184 (2019) 901–915. https://doi.org/10.1016/j.neuroimage.2018.09.081.

[63] C. Gros, B. De Leener, S.M. Dupont, A.R. Martin, M.G. Fehlings, R. Bakshi, S. Tummala, V. Auclair, D.G. McLaren, V. Callot, J. Cohen-Adad, M. Sdika, *Automatic spinal cord localization, robust to MRI contrasts using global curve optimization*, Med Image Anal. 44 (2018) 215–227. https://doi.org/10.1016/j.media.2017.12.001.

[64] L.G. Nyul, J.K. Udupa, *On standardizing the MR image intensity scale*, Magn Reson Med. 42 (1999) 1072–1081. https://doi.org/10.1002/(SICI)1522-2594(199912)42:6<1072::AID-MRM11>3.0.CO;2-M.

[65] Ö. Cicek, A. Abdulkadir, S.S. Lienkamp, T. Brox, R. Olaf, *3D U-Net: Learning Dense Volumetric Segmentation from Sparse Annotation*, Medical Image Computing and Computer-Assisted Intervention – MICCAI. (2016).

[66] F. Prados, M. Moccia, A. Johnson, M. Yiannakas, F. Grussu, M.J. Cardoso, O. Ciccarelli, S. Ourselin, F. Barkhof, C. Wheeler-Kingshott, *Generalised boundary shift integral for longitudinal assessment of spinal cord atrophy*, Neuroimage. 209 (2020) 116489. https://doi.org/10.1016/j.neuroimage.2019.116489.

[67] D.K. Jones, P.J. Basser, *Squashing peanuts and smashing pumpkins?: How noise distorts diffusion-weighted MR data*, Magn Reson Med. 52 (2004) 979–993. https://doi.org/10.1002/mrm.20283.

[68] A. Tristán-Vega, V. García-Pérez, S. Aja-Fernández, C.-F. Westin, *Efficient and robust nonlocal means denoising of MR data based on salient features matching*, Comput Methods Programs Biomed. 105 (2012) 131–144. https://doi.org/10.1016/j.cmpb.2011.07.014.

[69] N.J. Tustison, B.B. Avants, P.A. Cook, Yuanjie Zheng, A. Egan, P.A. Yushkevich, J.C. Gee, *N4ITK: Improved N3 Bias Correction*, IEEE Trans Med Imaging. 29 (2010) 1310–1320. https://doi.org/10.1109/TMI.2010.2046908.

[70] B. De Leener, G. Mangeat, S. Dupont, A.R. Martin, V. Callot, N. Stikov, M.G. Fehlings, J. Cohen-Adad, *Topologically preserving straightening of spinal cord MRI*, Journal of Magnetic Resonance Imaging. 46 (2017) 1209–1219. https://doi.org/10.1002/jmri.25622.

[71] M. Modat, D.M. Cash, P. Daga, G.P. Winston, J.S. Duncan, S. Ourselin, *Global image registration using a symmetric block-matching approach*, Journal of Medical Imaging. 1 (2014) 024003. https://doi.org/10.1117/1.JMI.1.2.024003.

[72] A. Buades, B. Coll, J.-M. Morel, A Non-Local Algorithm for Image Denoising, in: IEEE Computer Society Conference on Computer Vision and Pattern Recognition (CVPR'05), IEEE, 2005: pp. 60–65. https://doi.org/10.1109/CVPR.2005.38.

[73] C. Chien, M. Scheel, T. Schmitz-Hübsch, N. Borisow, K. Ruprecht, J. Bellmann-Strobl, F. Paul, A.U. Brandt, *Spinal cord lesions and atrophy in NMOSD with AQP4-IgG and MOG-IgG associated autoimmunity*, Multiple Sclerosis Journal. 25 (2019) 1926–1936. https://doi.org/10.1177/1352458518815596.

[74] Y. Liu, J. Wang, M. Daams, F. Weiler, H.K. Hahn, Y. Duan, J. Huang, Z. Ren, J. Ye, H. Dong, H. Vrenken, M.P. Wattjes, F.-D. Shi, K. Li, F. Barkhof, *Differential patterns of spinal cord and brain atrophy in NMO and MS*, Neurology. 84 (2015) 1465–1472. https://doi.org/10.1212/WNL.0000000000001441.

[75] R. Schneider, B. Bellenberg, I. Kleiter, R. Gold, O. Köster, F. Weiler, H. Hahn, C. Lukas, *Cervical cord and ventricle affection in neuromyelitis optica*, Acta Neurol Scand. 135 (2017) 324–331. https://doi.org/10.1111/ane.12601.

[76] S. Azodi, G. Nair, Y. Enose-Akahata, E. Charlip, A. Vellucci, I. Cortese, J. Dwyer, B.J. Billioux, C. Thomas, J. Ohayon, D.S. Reich, S. Jacobson, *Imaging spinal cord atrophy in progressive myelopathies: HTLV-I-associated neurological disease (HAM/TSP) and multiple sclerosis (MS)*, Ann Neurol. 82 (2017) 719–728. https://doi.org/10.1002/ana.25072.

[77] M.M. El Mendili, G. Querin, P. Bede, P.-F. Pradat, *Spinal Cord Imaging in Amyotrophic Lateral Sclerosis: Historical Concepts—Novel Techniques*, Front Neurol. 10 (2019) 1–11. https://doi.org/10.3389/fneur.2019.00350.

[78] M.-Ê. Paquin, M.M. El Mendili, C. Gros, S.M. Dupont, J. Cohen-Adad, P.-F. Pradat, *Spinal Cord Gray Matter Atrophy in Amyotrophic Lateral Sclerosis*, American Journal of Neuroradiology. 39 (2018) 184–192. https://doi.org/10.3174/ajnr.A5427.

[79] N.T. Olney, A. Bischof, H. Rosen, E. Caverzasi, W.A. Stern, C. Lomen-Hoerth, B.L. Miller, R.G. Henry, N. Papinutto, *Measurement of spinal cord atrophy using phase sensitive inversion recovery (PSIR) imaging in motor neuron disease*, PLoS One. 13 (2018) e0208255. https://doi.org/10.1371/journal.pone.0208255.

[80] C.K. Denecke, A. Aljović, F.M. Bareyre, *Combining molecular intervention with in vivo imaging to untangle mechanisms of axon pathology and outgrowth following spinal cord injury*, Exp Neurol. 318 (2019) 1–11. https://doi.org/10.1016/j.expneurol.2019.04.003.

[81] C.F. Chevis, C.B. da Silva, A. D'Abreu, I. Lopes-Cendes, F. Cendes, F.P.G. Bergo, M.C. França, *Spinal Cord Atrophy Correlates with Disability in Friedreich's Ataxia*, The Cerebellum. 12 (2013) 43–47. https://doi.org/10.1007/s12311-012-0390-6.

[82] B. Behmanesh, F. Gessler, J. Quick-Weller, A. Spyrantis, L. Imöhl, V. Seifert, G. Marquardt, *Regional Spinal Cord Atrophy Is Associated with Poor Outcome After Surgery on Intramedullary Spinal Cord Ependymoma: A New Aspect of Delayed Neurological Deterioration*, World Neurosurg. 100 (2017) 250–255. https://doi.org/10.1016/j.wneu.2017.01.026.

[83] R.M. Lorenzi, F. Palesi, G. Castellazzi, P. Vitali, N. Anzalone, S. Bernini, M. Cotta Ramusino, E. Sinforiani, G. Micieli, A. Costa, E. D'Angelo, C.A.M. Gandini Wheeler-Kingshott, *Unsuspected Involvement of Spinal Cord in Alzheimer Disease*, Front Cell Neurosci. 14 (2020) 1–10. https://doi.org/10.3389/fncel.2020.00006.

[84] W. Wilhelms, B. Bellenberg, O. Köster, F. Weiler, R. Hoffmann, R. Gold, C. Saft, C. Lukas, *Progressive spinal cord atrophy in manifest and premanifest Huntington's disease*, J Neurol Neurosurg Psychiatry. 88 (2017) 614–616. https://doi.org/10.1136/jnnp-2016-315000.

[85] H. Lundell, D. Barthelemy, A. Skimminge, T.B. Dyrby, F. Biering-Sørensen, J.B. Nielsen, *Independent spinal cord atrophy measures correlate to motor and sensory deficits in individuals with spinal cord injury*, Spinal Cord. 49 (2011) 70–75. https://doi.org/10.1038/sc.2010.87.

[86] J. Cohen-Adad, M.-M. El Mendili, S. Lehéricy, P.-F. Pradat, S. Blancho, S. Rossignol, H. Benali, *Demyelination and degeneration in the injured human spinal cord detected with diffusion and magnetization transfer MRI*, Neuroimage. 55 (2011) 1024–1033. https://doi.org/10.1016/j.neuroimage.2010.11.089.

[87] J. Cohen-Adad, M.-M. El Mendili, R. Morizot-Koutlidis, S. Lehéricy, V. Meininger, S. Blancho, S. Rossignol, H. Benali, P.-F. Pradat, *Involvement of spinal sensory pathway in ALS and specificity of cord atrophy to lower motor neuron degeneration*, Amyotroph Lateral Scler Frontotemporal Degener. 14 (2013) 30–38. https://doi.org/10.3109/17482968.2012.701308.

[88] F. Agosta, M. Absinta, M.P. Sormani, A. Ghezzi, A. Bertolotto, E. Montanari, G. Comi, M. Filippi, *In vivo assessment of cervical cord damage in MS patients: a longitudinal diffusion tensor MRI study*, Brain. 130 (2007) 2211–2219. https://doi.org/10.1093/brain/awm110.

[89] A.B. Cohen, M. Neema, A. Arora, E. Dell'Oglio, R.H.B. Benedict, S. Tauhid, D. Goldberg-Zimring, C. Chavarro-Nieto, A. Ceccarelli, J.P. Klein, J.M. Stankiewicz, M.K. Houtchens, G.J. Buckle, D.C. Alsop, C.R.G. Guttmann, R. Bakshi, *The Relationships among MRI-Defined Spinal Cord Involvement, Brain Involvement, and Disability in Multiple Sclerosis*, Journal of Neuroimaging. 22 (2012) 122–128. https://doi.org/10.1111/j.1552-6569.2011.00589.x.

[90] A.J. Thompson, S.E. Baranzini, J. Geurts, B. Hemmer, O. Ciccarelli, *Multiple sclerosis*, The Lancet. 391 (2018) 1622–1636. https://doi.org/10.1016/S0140-6736(18)30481-1.

[91] E. Waubant, R. Lucas, E. Mowry, J. Graves, T. Olsson, L. Alfredsson, A. Langer-Gould, *Environmental and genetic risk factors for MS: an integrated review*, Ann Clin Transl Neurol. 6 (2019) 1905–1922. https://doi.org/10.1002/acn3.50862.

[92] A. Compston, A. Coles, *Multiple sclerosis*, The Lancet. 372 (2008) 1502–1517. https://doi.org/10.1016/S0140-6736(08)61620-7.

[93] B.D. Trapp, K.-A. Nave, *Multiple Sclerosis: An Immune or Neurodegenerative Disorder?*, Annu Rev Neurosci. 31 (2008) 247–269. https://doi.org/10.1146/annurev.neuro.30.051606.094313.

[94] M.T. Wallin, W.J. Culpepper, E. Nichols, Z.A. Bhutta, T.T. Gebrehiwot, S.I. Hay, I.A. Khalil, K.J. Krohn, X. Liang, M. Naghavi, A.H. Mokdad, M.R. Nixon, R.C. Reiner, B. Sartorius, M. Smith, R. Topor-Madry, A. Werdecker, T. Vos, V.L. Feigin, C.J.L. Murray, *Global, regional, and national burden of multiple sclerosis 1990–2016: a systematic analysis for the Global Burden of Disease Study 2016*, Lancet Neurol. 18 (2019) 269–285. https://doi.org/10.1016/S1474-4422(18)30443-5.

[95] A. Scalfari, *MS progression is predominantly driven by age-related mechanisms – YES*, Multiple Sclerosis Journal. 25 (2019) 902–904. https://doi.org/10.1177/1352458518820633.

[96] J.W. Peterson, L. Bö, S. Mörk, A. Chang, B.D. Trapp, *Transected neurites, apoptotic neurons, and reduced inflammation in cortical multiple sclerosis lesions*, Ann Neurol. 50 (2001) 389–400. https://doi.org/10.1002/ana.1123.

[97] A. Kutzelnigg, C.F. Lucchinetti, C. Stadelmann, W. Brück, H. Rauschka, M. Bergmann, M. Schmidbauer, J.E. Parisi, H. Lassmann, *Cortical demyelination and diffuse white matter injury in multiple sclerosis*, Brain. 128 (2005) 2705–2712. https://doi.org/10.1093/brain/awh641.

[98] N. Petrova, D. Carassiti, D.R. Altmann, D. Baker, K. Schmierer, *Axonal loss in the multiple sclerosis spinal cord revisited*, Brain Pathology. 28 (2018) 334–348. https://doi.org/10.1111/bpa.12516.

[99] K. Schmierer, A. McDowell, N. Petrova, D. Carassiti, D.L. Thomas, M.E. Miquel, *Quantifying multiple sclerosis pathology in post mortem spinal cord using MRI*, Neuroimage. 182 (2018) 251–258. https://doi.org/10.1016/j.neuroimage.2018.01.052.

[100] H. Lassmann, *Spinal cord pathology in multiple sclerosis*, Lancet Neurol. 14 (2015) 348–349. https://doi.org/10.1016/S1474-4422(15)70037-2.

[101] S. Bramow, J.M. Frischer, H. Lassmann, N. Koch-Henriksen, C.F. Lucchinetti, P.S. Sørensen, H. Laursen, *Demyelination versus remyelination in progressive multiple sclerosis*, Brain. 133 (2010) 2983–2998. https://doi.org/10.1093/brain/awq250.

[102] J.M. Frischer, S.D. Weigand, Y. Guo, N. Kale, J.E. Parisi, I. Pirko, J. Mandrekar, S. Bramow, I. Metz, W. Brück, H. Lassmann, C.F. Lucchinetti, *Clinical and pathological insights into the dynamic nature of the white matter multiple sclerosis plaque*, Ann Neurol. 78 (2015) 710–721. https://doi.org/10.1002/ana.24497.

[103] H. Lassmann, *Multiple Sclerosis Pathology*, Cold Spring Harb Perspect Med. 8 (2018) a028936. https://doi.org/10.1101/cshperspect.a028936.

[104] F. Barkhof, P. Scheltens, S.T. Frequin, J.J. Nauta, M.W. Tas, J. Valk, O.R. Hommes, *Relapsing-remitting multiple sclerosis: sequential enhanced MR imaging vs clinical findings in determining disease activity.*, American Journal of Roentgenology. 159 (1992) 1041–1047. https://doi.org/10.2214/ajr.159.5.1414773.

[105] H. Lassmann, *Neuropathology in multiple sclerosis: new concepts*, Multiple Sclerosis Journal. 4 (1998) 93–98. https://doi.org/10.1177/135245859800400301.

[106] C. Lucchinetti, W. Bruck, J. Parisi, B. Scheithauer, M. Rodriguez, H. Lassmann, *Heterogeneity of multiple sclerosis lesions: Implications for the pathogenesis of demyelination*, Ann Neurol. 47 (2000) 707–717. https://doi.org/10.1002/1531-8249(200006)47:6<707::AID-ANA3>3.0.CO;2-Q.

[107] K.-A. Nave, B.D. Trapp, *Axon-Glial Signaling and the Glial Support of Axon Function*, Annu Rev Neurosci. 31 (2008) 535–561. https://doi.org/10.1146/annurev.neuro.30.051606.094309.

[108] B.D. Trapp, J. Peterson, R.M. Ransohoff, R. Rudick, S. Mörk, L. Bö, *Axonal Transection in the Lesions of Multiple Sclerosis*, New England Journal of Medicine. 338 (1998) 278–285. https://doi.org/10.1056/NEJM199801293380502.

[109] K. Schmierer, F. Scaravilli, D.R. Altmann, G.J. Barker, D.H. Miller, *Magnetization transfer ratio and myelin in postmortem multiple sclerosis brain*, Ann Neurol. 56 (2004) 407–415. https://doi.org/10.1002/ana.20202.

[110] G.C. DeLuca, *The contribution of demyelination to axonal loss in multiple sclerosis*, Brain. 129 (2006) 1507–1516. https://doi.org/10.1093/brain/awl074.

[111] J.P. Mottershead, K. Schmierer, M. Clemence, J.S. Thornton, F. Scaravilli, G.J. Barker, P.S. Tofts, J. Newcombe, M.L. Cuzner, R.J. Ordidge, W.I. McDonald, D.H. Miller, *High field MRI correlates of myelin content and axonal density in multiple sclerosis*, J Neurol. 250 (2003) 1293–1301. https://doi.org/10.1007/s00415-003-0192-3.

[112] G. Criste, B. Trapp, R. Dutta, Axonal loss in multiple sclerosis, in: Causes and mechanisms, 2014: pp. 101–113. https://doi.org/10.1016/B978-0-444-52001-2.00005-4.

[113] B.D. Trapp, M. Vignos, J. Dudman, A. Chang, E. Fisher, S.M. Staugaitis, H. Battapady, S. Mork, D. Ontaneda, S.E. Jones, R.J. Fox, J. Chen, K. Nakamura, R.A. Rudick, *Cortical neuronal densities and cerebral white matter demyelination in multiple sclerosis: a retrospective study*, Lancet Neurol. 17 (2018) 870–884. https://doi.org/10.1016/S1474-4422(18)30245-X.

[114] L. Haider, T. Zrzavy, S. Hametner, R. Höftberger, F. Bagnato, G. Grabner, S. Trattnig, S. Pfeifenbring, W. Brück, H. Lassmann, *The topograpy of demyelination and neurodegeneration in the multiple sclerosis brain*, Brain. 139 (2016) 807–815. https://doi.org/10.1093/brain/awv398.

[115] L. Haider, *Inflammation, Iron, Energy Failure, and Oxidative Stress in the Pathogenesis of Multiple Sclerosis*, Oxid Med Cell Longev. 2015 (2015) 1–10. https://doi.org/10.1155/2015/725370.

[116] L. Haider, M.T. Fischer, J.M. Frischer, J. Bauer, R. Hoftberger, G. Botond, H. Esterbauer, C.J. Binder, J.L. Witztum, H. Lassmann, *Oxidative damage in multiple sclerosis lesions*, Brain. 134 (2011) 1914–1924. https://doi.org/10.1093/brain/awr128.

[117] S. Faissner, J.R. Plemel, R. Gold, V.W. Yong, *Progressive multiple sclerosis: from pathophysiology to therapeutic strategies*, Nat Rev Drug Discov. 18 (2019) 905–922. https://doi.org/10.1038/s41573-019-0035-2.

[118] M. Moccia, O. Ciccarelli, *Molecular and Metabolic Imaging in Multiple Sclerosis*, Neuroimaging Clin N Am. 27 (2017) 343–356. https://doi.org/10.1016/j.nic.2016.12.005.

[119] H. Lassmann, *Pathogenic Mechanisms Associated With Different Clinical Courses of Multiple Sclerosis*, Front Immunol. 9 (2019) 1–14. https://doi.org/10.3389/fimmu.2018.03116.

[120] C.A. Dendrou, L. Fugger, M.A. Friese, *Immunopathology of multiple sclerosis*, Nat Rev Immunol. 15 (2015) 545–558. https://doi.org/10.1038/nri3871.

[121] L.H. Kasper, J. Shoemaker, *Multiple sclerosis immunology: The healthy immune system vs the MS immune system*, Neurology. 74 (2010) S2–S8. https://doi.org/10.1212/WNL.0b013e3181c97c8f.

[122] R. Gandhi, A. Laroni, H.L. Weiner, *Role of the innate immune system in the pathogenesis of multiple sclerosis*, J Neuroimmunol. 221 (2010) 7–14. https://doi.org/10.1016/j.jneuroim.2009.10.015.

[123] J.I. Spencer, J.S. Bell, G.C. DeLuca, *Vascular pathology in multiple sclerosis: reframing pathogenesis around the blood-brain barrier*, J Neurol Neurosurg Psychiatry. 89 (2018) 42–52. https://doi.org/10.1136/jnnp-2017-316011.

[124] J.S. Bell, J.I. Spencer, R.L. Yates, G.C. DeLuca, *The cortical blood–brain barrier in multiple sclerosis: a gateway to progression?*, J Neurol. 265 (2018) 966–967. https://doi.org/10.1007/s00415-017-8727-1.

[125] J. Machado-Santos, E. Saji, A.R. Tröscher, M. Paunovic, R. Liblau, G. Gabriely, C.G. Bien, J. Bauer, H. Lassmann, *The compartmentalized inflammatory response in the multiple sclerosis brain is composed of tissue-resident CD8+ T lymphocytes and B cells*, Brain. 141 (2018) 2066–2082. https://doi.org/10.1093/brain/awy151.

[126] O.W. Howell, C.A. Reeves, R. Nicholas, D. Carassiti, B. Radotra, S.M. Gentleman, B. Serafini, F. Aloisi, F. Roncaroli, R. Magliozzi, R. Reynolds, *Meningeal inflammation is widespread and linked to cortical pathology in multiple sclerosis*, Brain. 134 (2011) 2755–2771. https://doi.org/10.1093/brain/awr182.

[127] R. Magliozzi, O.W. Howell, C. Reeves, F. Roncaroli, R. Nicholas, B. Serafini, F. Aloisi, R. Reynolds, *A Gradient of neuronal loss and meningeal inflammation in multiple sclerosis*, Ann Neurol. 68 (2010) 477–493. https://doi.org/10.1002/ana.22230.

[128] R. Magliozzi, B. Serafini, B. Rosicarelli, G. Chiappetta, C. Veroni, R. Reynolds, F. Aloisi, *B-Cell Enrichment and Epstein-Barr Virus Infection in Inflammatory Cortical Lesions in Secondary Progressive Multiple Sclerosis*, J Neuropathol Exp Neurol. 72 (2013) 29–41. https://doi.org/10.1097/NEN.0b013e31827bfc62.

[129] J.M. Frischer, S. Bramow, A. Dal-Bianco, C.F. Lucchinetti, H. Rauschka, M. Schmidbauer, H. Laursen, P.S. Sorensen, H. Lassmann, *The relation between inflammation and neurodegeneration in multiple sclerosis brains*, Brain. 132 (2009) 1175–1189. https://doi.org/10.1093/brain/awp070.

[130] H. Lassmann, *Multiple Sclerosis Pathology and its Reflection by Imaging Technologies: Introduction*, Brain Pathology. 28 (2018) 721–722. https://doi.org/10.1111/bpa.12649.

[131] F. De Angelis, N.A. John, W.J. Brownlee, *Disease-modifying therapies for multiple sclerosis*, BMJ. (2018) k4674. https://doi.org/10.1136/bmj.k4674.

[132] M.P. Sormani, P. Bruzzi, *MRI lesions as a surrogate for relapses in multiple sclerosis: a meta-analysis of randomised trials*, Lancet Neurol. 12 (2013) 669–676. https://doi.org/10.1016/S1474-4422(13)70103-0.

[133] D.H. Miller, S.M. Leary, *Primary-progressive multiple sclerosis*, Lancet Neurol. 6 (2007) 903–912. https://doi.org/10.1016/S1474-4422(07)70243-0.

[134] P. Zaratin, G. Comi, T. Coetzee, K. Ramsey, K. Smith, A. Thompson, M. Panzara, *Progressive MS Alliance Industry Forum: Maximizing Collective Impact To Enable Drug*

Development, Trends Pharmacol Sci. 37 (2016) 808–810. https://doi.org/10.1016/j.tips.2016.07.005.

[135] M. Moccia, N. de Stefano, F. Barkhof, *Imaging outcome measures for progressive multiple sclerosis trials*, Multiple Sclerosis Journal. 23 (2017) 1614–1626. https://doi.org/10.1177/1352458517729456.

[136] L. Bö, J.J.G. Geurts, R. Ravid, F. Barkhof, *Magnetic resonance imaging as a tool to examine the neuropathology of multiple sclerosis*, Neuropathol Appl Neurobiol. 30 (2004) 106–117. https://doi.org/10.1111/j.1365-2990.2003.00521.x.

[137] M. Filippi, W. Brück, D. Chard, F. Fazekas, J.J.G. Geurts, C. Enzinger, S. Hametner, T. Kuhlmann, P. Preziosa, À. Rovira, K. Schmierer, C. Stadelmann, M.A. Rocca, *Association between pathological and MRI findings in multiple sclerosis*, Lancet Neurol. 18 (2019) 198–210. https://doi.org/10.1016/S1474-4422(18)30451-4.

[138] P.L. Hubbard, F.-L. Zhou, S.J. Eichhorn, G.J.M. Parker, *Biomimetic phantom for the validation of diffusion magnetic resonance imaging*, Magn Reson Med. 73 (2015) 299–305. https://doi.org/10.1002/mrm.25107.

[139] R. Cortese, O. Ciccarelli, *Clinical monitoring of multiple sclerosis should routinely include spinal cord imaging – Yes*, Multiple Sclerosis Journal. 24 (2018) 1536–1537. https://doi.org/10.1177/1352458518778010.

[140] K. Schmierer, M.E. Miquel, *Magnetic resonance imaging correlates of neuro-axonal pathology in the MS spinal cord*, Brain Pathology. 28 (2018) 765–772. https://doi.org/10.1111/bpa.12648.

[141] A.J. Thompson, B.L. Banwell, F. Barkhof, W.M. Carroll, T. Coetzee, G. Comi, J. Correale, F. Fazekas, M. Filippi, M.S. Freedman, K. Fujihara, S.L. Galetta, H.P. Hartung, L. Kappos, F.D. Lublin, R.A. Marrie, A.E. Miller, D.H. Miller, X. Montalban, E.M. Mowry, P.S. Sorensen, M. Tintoré, A.L. Traboulsee, M. Trojano, B.M.J. Uitdehaag, S. Vukusic, E. Waubant, B.G. Weinshenker, S.C. Reingold, J.A. Cohen, *Diagnosis of multiple sclerosis: 2017 revisions of the McDonald criteria*, Lancet Neurol. 17 (2018) 162–173. https://doi.org/10.1016/S1474-4422(17)30470-2.

[142] M. Tintore, S. Otero-Romero, J. Río, G. Arrambide, B. Pujal, C. Tur, I. Galán, M. Comabella, C. Nos, M.J. Arévalo, A. Vidal-Jordana, J. Castilló, B. Rodríguez-Acevedo, L. Midaglia, R. Mitjana, C. Auger, J. Sastre-Garriga, À. Rovira, X. Montalban, *Contribution of the symptomatic lesion in establishing MS diagnosis and prognosis*, Neurology. 87 (2016) 1368–1374. https://doi.org/10.1212/WNL.0000000000003144.

[143] M. Filippi, M.A. Rocca, O. Ciccarelli, N. De Stefano, N. Evangelou, L. Kappos, A. Rovira, J. Sastre-Garriga, M. Tintorè, J.L. Frederiksen, C. Gasperini, J. Palace, D.S. Reich, B. Banwell, X. Montalban, F. Barkhof, *MRI criteria for the diagnosis of multiple sclerosis: MAGNIMS consensus guidelines*, Lancet Neurol. 15 (2016) 292–303. https://doi.org/10.1016/S1474-4422(15)00393-2.

[144] W.J. Brownlee, J.K. Swanton, K.A. Miszkiel, D.H. Miller, O. Ciccarelli, *Should the symptomatic region be included in dissemination in space in MRI criteria for MS?*, Neurology. 87 (2016) 680–683. https://doi.org/10.1212/WNL.0000000000002975.

[145] A. Rovira, N. de Stefano, *MRI monitoring of spinal cord changes in patients with multiple sclerosis*, Curr Opin Neurol. 29 (2016) 445–452. https://doi.org/10.1097/WCO.0000000000000343.

[146] J.CJ. Bot, F. Barkhof, *Spinal-Cord MRI in Multiple Sclerosis: Conventional and Nonconventional MR Techniques*, Neuroimaging Clin N Am. 19 (2009) 81–99. https://doi.org/10.1016/j.nic.2008.09.005.

[147] F. Barkhof, *Spinal cord MRI should always be performed in clinically isolated syndrome patients: Yes*, Multiple Sclerosis Journal. 20 (2014) 1688–1689. https://doi.org/10.1177/1352458514546518.

[148] B.M. Keegan, T.J. Kaufmann, B.G. Weinshenker, O.H. Kantarci, W.F. Schmalstieg, M.M. Paz Soldan, E.P. Flanagan, *Progressive solitary sclerosis*, Neurology. 87 (2016) 1713–1719. https://doi.org/10.1212/WNL.0000000000003235.

[149] J.P. Schee, S. Viswanathan, *Pure spinal multiple sclerosis: A possible novel entity within the multiple sclerosis disease spectrum*, Multiple Sclerosis Journal. 25 (2019) 1189–1195. https://doi.org/10.1177/1352458518775912.

[150] A. Gass, M.A. Rocca, F. Agosta, O. Ciccarelli, D. Chard, P. Valsasina, J.C.W. Brooks, A. Bischof, P. Eisele, L. Kappos, F. Barkhof, M. Filippi, *MRI monitoring of pathological changes in the spinal cord in patients with multiple sclerosis*, Lancet Neurol. 14 (2015) 443–454. https://doi.org/10.1016/S1474-4422(14)70294-7.

[151] B.D. Trapp, J. Peterson, R.M. Ransohoff, R. Rudick, S. Mörk, L. Bö, *Axonal Transection in the Lesions of Multiple Sclerosis*, New England Journal of Medicine. 338 (1998) 278–285. https://doi.org/10.1056/NEJM199801293380502.

[152] P.A. Brex, *Measurement of spinal cord area in clinically isolated syndromes suggestive of multiple sclerosis*, J Neurol Neurosurg Psychiatry. 70 (2001) 544–547. https://doi.org/10.1136/jnnp.70.4.544.

[153] C.P. Gilmore, G.C. DeLuca, L. Bö, T. Owens, J. Lowe, M.M. Esiri, N. Evangelou, *Spinal Cord Neuronal Pathology in Multiple Sclerosis*, Brain Pathology. 19 (2009) 642–649. https://doi.org/10.1111/j.1750-3639.2008.00228.x.

[154] G.C. DeLuca, *Axonal loss in multiple sclerosis: a pathological survey of the corticospinal and sensory tracts*, Brain. 127 (2004) 1009–1018. https://doi.org/10.1093/brain/awh118.

[155] F. Agosta, M. Filippi, *MRI of Spinal Cord in Multiple Sclerosis*, Journal of Neuroimaging. 17 (2007) 46S-49S. https://doi.org/10.1111/j.1552-6569.2007.00137.x.

[156] N. Evangelou, *Pathological study of spinal cord atrophy in multiple sclerosis suggests limited role of local lesions*, Brain. 128 (2004) 29–34. https://doi.org/10.1093/brain/awh323.

[157] C.P. Gilmore, G.C. DeLuca, L. Bö, T. Owens, J. Lowe, M.M. Esiri, N. Evangelou, *Spinal Cord Atrophy in Multiple Sclerosis Caused by White Matter Volume Loss*, Arch Neurol. 62 (2005) 1859. https://doi.org/10.1001/archneur.62.12.1859.

[158] D.T. Chard, *The longitudinal relation between brain lesion load and atrophy in multiple sclerosis: a 14 year follow up study*, J Neurol Neurosurg Psychiatry. 74 (2003) 1551–1554. https://doi.org/10.1136/jnnp.74.11.1551.

[159] H. Kearney, D.H. Miller, O. Ciccarelli, *Spinal cord MRI in multiple sclerosis—diagnostic, prognostic and clinical value*, Nat Rev Neurol. 11 (2015) 327–338. https://doi.org/10.1038/nrneurol.2015.80.

[160] S. Ruggieri, M. Petracca, A. Miller, S. Krieger, R. Ghassemi, Y. Bencosme, C. Riley, J. Howard, F. Lublin, M. Inglese, *Association of Deep Gray Matter Damage With Cortical and Spinal Cord Degeneration in Primary Progressive Multiple Sclerosis*, JAMA Neurol. 72 (2015) 1466. https://doi.org/10.1001/jamaneurol.2015.1897.

[161] C. Casserly, E.E. Seyman, P. Alcaide-Leon, M. Guenette, C. Lyons, S. Sankar, A. Svendrovski, S. Baral, J. Oh, *Spinal Cord Atrophy in Multiple Sclerosis: A Systematic Review and Meta-Analysis*, Journal of Neuroimaging. 28 (2018) 556–586. https://doi.org/10.1111/jon.12553.

[162] B.C. Healy, A. Arora, D.L. Hayden, A. Ceccarelli, S.S. Tauhid, M. Neema, R. Bakshi, *Approaches to Normalization of Spinal Cord Volume: Application to Multiple Sclerosis*, Journal of Neuroimaging. 22 (2012) e12–e19. https://doi.org/10.1111/j.1552-6569.2011.00629.x.

[163] J. Oh, M. Seigo, S. Saidha, E. Sotirchos, K. Zackowski, M. Chen, J. Prince, M. Diener-West, P.A. Calabresi, D.S. Reich, *Spinal Cord Normalization in Multiple Sclerosis*, Journal of Neuroimaging. 24 (2014) 577–584. https://doi.org/10.1111/jon.12097.

[164] R. Schlaeger, N. Papinutto, A.H. Zhu, I. V. Lobach, C.J. Bevan, M. Bucci, A. Castellano, J.M. Gelfand, J.S. Graves, A.J. Green, K.M. Jordan, A. Keshavan, V. Panara, W.A. Stern, H.-C. von Büdingen, E. Waubant, D.S. Goodin, B.A.C. Cree, S.L. Hauser, R.G. Henry, *Association Between Thoracic Spinal Cord Gray Matter Atrophy and Disability in Multiple Sclerosis*, JAMA Neurol. 72 (2015) 897. https://doi.org/10.1001/jamaneurol.2015.0993.

[165] L.H. Hua, S.L. Donlon, M.J. Sobhanian, S.M. Portner, D.T. Okuda, *Thoracic spinal cord lesions are influenced by the degree of cervical spine involvement in multiple sclerosis*, Spinal Cord. 53 (2015) 520–525. https://doi.org/10.1038/sc.2014.238.

[166] M.A. Rocca, P. Valsasina, A. Meani, C. Gobbi, C. Zecca, À. Rovira, X. Montalban, H. Kearney, O. Ciccarelli, L. Matthews, J. Palace, A. Gallo, A. Bisecco, A. Gass, P. Eisele, C.

Lukas, B. Bellenberg, F. Barkhof, H. Vrenken, P. Preziosa, G. Comi, M. Filippi, *Clinically relevant cranio-caudal patterns of cervical cord atrophy evolution in MS*, Neurology. 93 (2019) e1852–e1866. https://doi.org/10.1212/WNL.0000000000008466.

[167] M. Daams, F. Weiler, M.D. Steenwijk, H.K. Hahn, J.J. Geurts, H. Vrenken, R.A. van Schijndel, L.J. Balk, P.K. Tewarie, J.-M. Tillema, J. Killestein, B.M. Uitdehaag, F. Barkhof, *Mean upper cervical cord area (MUCCA) measurement in long-standing multiple sclerosis: Relation to brain findings and clinical disability*, Multiple Sclerosis Journal. 20 (2014) 1860–1865. https://doi.org/10.1177/1352458514533399.

[168] V. Biberacher, C.C. Boucard, P. Schmidt, C. Engl, D. Buck, A. Berthele, M.-M. Hoshi, C. Zimmer, B. Hemmer, M. Mühlau, *Atrophy and structural variability of the upper cervical cord in early multiple sclerosis*, Multiple Sclerosis Journal. 21 (2015) 875–884. https://doi.org/10.1177/1352458514546514.

[169] M.A. Rocca, M.A. Horsfield, S. Sala, M. Copetti, P. Valsasina, S. Mesaros, V. Martinelli, D. Caputo, T. Stosic-Opincal, J. Drulovic, G. Comi, M. Filippi, *A multicenter assessment of cervical cord atrophy among MS clinical phenotypes*, Neurology. 76 (2011) 2096–2102. https://doi.org/10.1212/WNL.0b013e31821f46b8.

[170] I.T. Hagström, R. Schneider, B. Bellenberg, A. Salmen, F. Weiler, O. Köster, R. Gold, C. Lukas, *Relevance of early cervical cord volume loss in the disease evolution of clinically isolated syndrome and early multiple sclerosis: a 2-year follow-up study*, J Neurol. 264 (2017) 1402–1412. https://doi.org/10.1007/s00415-017-8537-5.

[171] W. Brownlee, D. Altmann, P. Alves Da Mota, J. Swanton, K. Miszkiel, C.G. Wheeler-Kingshott, O. Ciccarelli, D. Miller, *Association of asymptomatic spinal cord lesions and atrophy with disability 5 years after a clinically isolated syndrome*, Multiple Sclerosis Journal. 23 (2017) 665–674. https://doi.org/10.1177/1352458516663034.

[172] C. Tsagkas, S. Magon, L. Gaetano, S. Pezold, Y. Naegelin, M. Amann, C. Stippich, P. Cattin, J. Wuerfel, O. Bieri, T. Sprenger, L. Kappos, K. Parmar, *Preferential spinal cord volume loss in primary progressive multiple sclerosis*, Multiple Sclerosis Journal. 25 (2019) 947–957. https://doi.org/10.1177/1352458518775006.

[173] J. Furby, T. Hayton, D. Altmann, R. Brenner, J. Chataway, K.J. Smith, D.H. Miller, R. Kapoor, *A longitudinal study of MRI-detected atrophy in secondary progressive multiple sclerosis*, J Neurol. 257 (2010) 1508–1516. https://doi.org/10.1007/s00415-010-5563-y.

[174] W. Rashid, G.R. Davies, D.T. Chard, C.M. Griffin, D.R. Altmann, R. Gordon, R. Kapoor, A.J. Thompson, D.H. Miller, *Upper cervical cord area in early relapsing-remitting multiple sclerosis: Cross-sectional study of factors influencing cord size*, Journal of Magnetic Resonance Imaging. 23 (2006) 473–476. https://doi.org/10.1002/jmri.20545.

[175] W. Rashid, *Increasing cord atrophy in early relapsing-remitting multiple sclerosis: a 3 year study*, J Neurol Neurosurg Psychiatry. 77 (2006) 51–55. https://doi.org/10.1136/jnnp.2005.068338.

[176] N. Cawley, C. Tur, F. Prados, D. Plantone, H. Kearney, K. Abdel-Aziz, S. Ourselin, C.A.G. Wheeler-Kingshott, D.H. Miller, A.J. Thompson, O. Ciccarelli, *Spinal cord atrophy as a primary outcome measure in phase II trials of progressive multiple sclerosis*, Multiple Sclerosis Journal. 24 (2018) 932–941. https://doi.org/10.1177/1352458517709954.

[177] A. Eshaghi, F. Prados, W.J. Brownlee, D.R. Altmann, C. Tur, M.J. Cardoso, F. De Angelis, S.H. van de Pavert, N. Cawley, N. De Stefano, M.L. Stromillo, M. Battaglini, S. Ruggieri, C. Gasperini, M. Filippi, M.A. Rocca, A. Rovira, J. Sastre-Garriga, H. Vrenken, C.E. Leurs, J. Killestein, L. Pirpamer, C. Enzinger, S. Ourselin, C.A.M.G. Wheeler-Kingshott, D. Chard, A.J. Thompson, D.C. Alexander, F. Barkhof, O. Ciccarelli, *Deep gray matter volume loss drives disability worsening in multiple sclerosis*, Ann Neurol. 83 (2018) 210–222. https://doi.org/10.1002/ana.25145.

[178] H. Kearney, M. Rocca, P. Valsasina, L. Balk, J. Sastre-Garriga, J. Reinhardt, S. Ruggieri, A. Rovira, C. Stippich, L. Kappos, T. Sprenger, P. Tortorella, M. Rovaris, C. Gasperini, X. Montalban, J. Geurts, C. Polman, F. Barkhof, M. Filippi, D. Altmann, O. Ciccarelli, D. Miller, D. Chard, *Magnetic resonance imaging correlates of physical disability in relapse onset multiple sclerosis of long disease duration*, Multiple Sclerosis Journal. 20 (2014) 72–80. https://doi.org/10.1177/1352458513492245.

[179] F.X. Aymerich, C. Auger, J. Alonso, M. Alberich, J. Sastre-Garriga, M. Tintoré, X. Montalban, A. Rovira, *Cervical Cord Atrophy and Long-Term Disease Progression in Patients with Primary-Progressive Multiple Sclerosis*, American Journal of Neuroradiology. 39 (2018) 399–404. https://doi.org/10.3174/ajnr.A5495.

[180] W. Brownlee, D. Altmann, P. Alves Da Mota, J. Swanton, K. Miszkiel, C.G. Wheeler-Kingshott, O. Ciccarelli, D. Miller, *Association of asymptomatic spinal cord lesions and atrophy with disability 5 years after a clinically isolated syndrome*, Multiple Sclerosis Journal. 23 (2017) 665–674. https://doi.org/10.1177/1352458516663034.

[181] C. Tsagkas, S. Magon, L. Gaetano, S. Pezold, Y. Naegelin, M. Amann, C. Stippich, P. Cattin, J. Wuerfel, O. Bieri, T. Sprenger, L. Kappos, K. Parmar, *Spinal cord volume loss*, Neurology. 91 (2018) e349–e358. https://doi.org/10.1212/WNL.0000000000005853.

[182] H. Kearney, T. Schneider, M.C. Yiannakas, D.R. Altmann, C.A.M. Wheeler-Kingshott, O. Ciccarelli, D.H. Miller, *Spinal cord grey matter abnormalities are associated with secondary progression and physical disability in multiple sclerosis*, J Neurol Neurosurg Psychiatry. 86 (2015) 608–614. https://doi.org/10.1136/jnnp-2014-308241.

[183] U. Bonati, L.K. Fisniku, D.R. Altmann, M.C. Yiannakas, J. Furby, A.J. Thompson, D.H. Miller, D.T. Chard, *Cervical cord and brain grey matter atrophy independently associate with long-term MS disability*, J Neurol Neurosurg Psychiatry. 82 (2011) 471–472. https://doi.org/10.1136/jnnp.2010.205021.

[184] R. Kapoor, J. Furby, T. Hayton, K.J. Smith, D.R. Altmann, R. Brenner, J. Chataway, R.A. Hughes, D.H. Miller, *Lamotrigine for neuroprotection in secondary progressive multiple sclerosis: a randomised, double-blind, placebo-controlled, parallel-group trial*, Lancet Neurol. 9 (2010) 681–688. https://doi.org/10.1016/S1474-4422(10)70131-9.

[185] T. Singhal, S. Tauhid, S. Hurwitz, M. Neema, R. Bakshi, *The Effect of Glatiramer Acetate on Spinal Cord Volume in Relapsing-Remitting Multiple Sclerosis*, Journal of Neuroimaging. 27 (2017) 33–36. https://doi.org/10.1111/jon.12378.

[186] S.L. Dupuy, F. Khalid, B.C. Healy, S. Bakshi, M. Neema, S. Tauhid, R. Bakshi, *The effect of intramuscular interferon beta-1a on spinal cord volume in relapsing-remitting multiple*

sclerosis, BMC Med Imaging. 16 (2016) 56. https://doi.org/10.1186/s12880-016-0158-4.

[187] F. Durand-Dubief, B. Belaroussi, J.P. Armspach, M. Dufour, S. Roggerone, S. Vukusic, S. Hannoun, D. Sappey-Marinier, C. Confavreux, F. Cotton, *Reliability of Longitudinal Brain Volume Loss Measurements between 2 Sites in Patients with Multiple Sclerosis: Comparison of 7 Quantification Techniques*, American Journal of Neuroradiology. 33 (2012) 1918–1924. https://doi.org/10.3174/ajnr.A3107.

[188] N. Papinutto, R. Bakshi, A. Bischof, P.A. Calabresi, E. Caverzasi, R.T. Constable, E. Datta, G. Kirkish, G. Nair, J. Oh, D. Pelletier, D.L. Pham, D.S. Reich, W. Rooney, S. Roy, D. Schwartz, R.T. Shinohara, N.L. Sicotte, W.A. Stern, I. Tagge, S. Tauhid, S. Tummala, R.G. Henry, *Gradient nonlinearity effects on upper cervical spinal cord area measurement from 3D T1-weighted brain MRI acquisitions*, Magn Reson Med. 79 (2018) 1595–1601. https://doi.org/10.1002/mrm.26776.

[189] L. Luchetti, F. Prados, R. Cortese, G. Gentile, M. Battaglini, N. De Stefano, Evaluation of spinal cord atrophy using a SIENA-like approach, in: ECTRIMS, 2022.

[190] M. Reuter, N.J. Schmansky, H.D. Rosas, B. Fischl, *Within-subject template estimation for unbiased longitudinal image analysis*, Neuroimage. 61 (2012) 1402–1418. https://doi.org/10.1016/j.neuroimage.2012.02.084.

[191] K.K. Leung, G.R. Ridgway, S. Ourselin, N.C. Fox, *Consistent multi-time-point brain atrophy estimation from the boundary shift integral*, Neuroimage. 59 (2012) 3995–4005. https://doi.org/10.1016/j.neuroimage.2011.10.068.

[192] S.M. Smith, A. Rao, N. De Stefano, M. Jenkinson, J.M. Schott, P.M. Matthews, N.C. Fox, *Longitudinal and cross-sectional analysis of atrophy in Alzheimer's disease: Cross-validation of BSI, SIENA and SIENAX*, Neuroimage. 36 (2007) 1200–1206. https://doi.org/10.1016/j.neuroimage.2007.04.035.

[193] F. Prados, F. Barkhof, *Spinal cord atrophy rates*, Neurology. 91 (2018) 157–158. https://doi.org/10.1212/WNL.0000000000005873.

[194] B. Healy, P. Valsasina, M. Filippi, R. Bakshi, *Sample size requirements for treatment effects using gray matter, white matter and whole brain volume in relapsing-remitting multiple sclerosis*, J Neurol Neurosurg Psychiatry. 80 (2009) 1218–1224. https://doi.org/10.1136/jnnp.2008.154732.

[195] I.J. van den Elskamp, B. Boden, V. Dattola, D.L. Knol, M. Filippi, L. Kappos, F. Fazekas, K. Wagner, C. Pohl, R. Sandbrink, C.H. Polman, B.M.J. Uitdehaag, F. Barkhof, *Cerebral atrophy as outcome measure in short-term phase 2 clinical trials in multiple sclerosis*, Neuroradiology. 52 (2010) 875–881. https://doi.org/10.1007/s00234-009-0645-1.

[196] M. Battaglini, G. Gentile, L. Luchetti, A. Giorgio, H. Vrenken, F. Barkhof, K.S. Cover, R. Bakshi, R. Chu, M.P. Sormani, C. Enzinger, S. Ropele, O. Ciccarelli, C. Wheeler-Kingshott, M. Yiannakas, M. Filippi, M.A. Rocca, P. Preziosa, A. Gallo, A. Bisecco, J. Palace, Y. Kong, D. Horakova, M. Vaneckova, C. Gasperini, S. Ruggieri, N. De Stefano, *Lifespan normative data on rates of brain volume changes*, Neurobiol Aging. 81 (2019) 30–37. https://doi.org/10.1016/j.neurobiolaging.2019.05.010.

[197] G. Giovannoni, D. Tomic, J.R. Bright, E. Havrdová, *"No evident disease activity": The use of combined assessments in the management of patients with multiple sclerosis*, Multiple Sclerosis Journal. 23 (2017) 1179–1187. https://doi.org/10.1177/1352458517703193.

[198] T. Uher, M. Vaneckova, L. Sobisek, M. Tyblova, Z. Seidl, J. Krasensky, D. Ramasamy, R. Zivadinov, E. Havrdova, T. Kalincik, D. Horakova, *Combining clinical and magnetic resonance imaging markers enhances prediction of 12-year disability in multiple sclerosis*, Multiple Sclerosis Journal. 23 (2017) 51–61. https://doi.org/10.1177/1352458516642314.